



저작자표시-비영리-변경금지 2.0 대한민국

이용자는 아래의 조건을 따르는 경우에 한하여 자유롭게

- 이 저작물을 복제, 배포, 전송, 전시, 공연 및 방송할 수 있습니다.

다음과 같은 조건을 따라야 합니다:



저작자표시. 귀하는 원저작자를 표시하여야 합니다.



비영리. 귀하는 이 저작물을 영리 목적으로 이용할 수 없습니다.



변경금지. 귀하는 이 저작물을 개작, 변형 또는 가공할 수 없습니다.

- 귀하는, 이 저작물의 재이용이나 배포의 경우, 이 저작물에 적용된 이용허락조건을 명확하게 나타내어야 합니다.
- 저작권자로부터 별도의 허가를 받으면 이러한 조건들은 적용되지 않습니다.

저작권법에 따른 이용자의 권리는 위의 내용에 의하여 영향을 받지 않습니다.

이것은 [이용허락규약\(Legal Code\)](#)을 이해하기 쉽게 요약한 것입니다.

[Disclaimer](#)

공학박사학위논문

듀얼암-유연성 베이스 시스템의 진동 저감 및  
힘 제어

Vibration Suppression and Wrench Control Framework of  
Dual-Arm Robotic System on Flexible Base

2024년 8월

서울대학교 대학원

기계항공공학부

이정섭

# 듀얼암-유연성 베이스 시스템의 진동 저감 및 힘 제어

Vibration Suppression and Wrench Control Framework of  
Dual-Arm Robotic System on Flexible Base

지도교수 이 동 준

이 논문을 공학박사 학위논문으로 제출함

2024년 4월

서울대학교 대학원

기계항공공학부

이 정 섭

이정섭의 공학박사 학위논문을 인준함

2024년 6월

위원장 : 조규진 (인)

부위원장 : 이동준 (인)

위원 : 박재홍 (인)

위원 : 신호철 (인)

위원 : 이진오 (인)

# *Abstract*

## *Vibration Suppression and Wrench Control Framework of Dual-Arm Robotic System on Flexible Base*

Jeongseob Lee

Graduate School of Mechanical and Aerospace Engineering

Seoul National University

In this thesis, we propose a novel control framework for high-precision/high-force interaction tasks of a dual-arm robotic system on a flexible base. The dual-arm robotic system on a long-reach base platform, which is designed for industrial inspection and maintenance operations in a height environment, exhibits substantial flexibility due to intrinsic compliance and the mechanical tolerance of the long-reach supporting platform. To address the challenge of this flexibility of the long-reach base system, we present two control strategies to handle the flexibility and enable high-precision and high-force operation: 1) passivity-based vibration suppression control, 2) optimal wrench control utilizing supporting surface.

First, we address the problem of the vibration of the flexible base induced by the dual-arm system motion and external disturbance. To suppress this vibration during precise motion tracking, we decompose the dynamics into two orthogonal subsystem dynamics with inertia decoupling. We adopt passive decomposition for this dynamics decomposition which preserves the passivity

of decomposed subsystem dynamics, and we design passivity-based vibration suppression control and motion tracking control for each decomposed dynamics separately. With this control framework, we can achieve precise in-height operation.

The second problem is to achieve high-force interaction tasks, in which most of the repair/maintenance tasks are included. To resolve the substantial deformation of the base during the high-force execution, we utilize the supporting surface by pushing or holding this surface by one arm while the other arm performs the high-force execution, as we humans do in daily life. For that, we first design the control as a combination of: 1) nominal control action; 2) active stiffness control; and 3) feedback wrench control. We then sequentially perform optimizations of the nominal configuration (and its related wrenches) and the active stiffness control gain. We also design the PI (proportional-integral) type wrench control to improve the robustness and precision of the control. The key theoretical enabler for our framework is a novel stiffness analysis of the dual-arm system with flexibility, which, when combined with supporting contact constraints, provides some peculiar relations, that can effectively be used to significantly simplify the optimization problem-solving and to facilitate the feedback wrench control design.

The efficacy of above control frameworks is validated by the experimental results, which show the possibility of the industrial application for high-precision/high-force in-height operation of the dual-arm robotic system on a long-reach base platform.

**Keywords:** Dual-Arm System, Flexible Base, Vibration Suppression Control, Dynamics Decomposition, Force Control, Supporting Contact

**Student Number:** 2016-20707

# Contents

<b>List of Figures</b>	<b>vi</b>
<b>List of Tables</b>	<b>xi</b>
<b>1 Introduction</b>	<b>1</b>
1.1 Motivation and Contribution . . . . .	1
1.2 Related Works . . . . .	5
1.2.1 Related Works of Vibration Suppression Control . . . . .	5
1.2.2 Related Works of Wrench Control . . . . .	7
1.3 Outline . . . . .	9
<b>2 Passivity-based Vibration Suppression Control</b>	<b>10</b>
2.1 Introduction . . . . .	10
2.2 Problem Formulation . . . . .	15
2.2.1 System Modeling . . . . .	15
2.2.2 Flexibility Modeling of the Telescopic Mast . . . . .	16
2.3 Design of Vibration Suppression Control . . . . .	18
2.3.1 Control Objectives . . . . .	18
2.3.2 Passive Decomposition . . . . .	19
2.3.3 Control Design . . . . .	21
2.3.4 State Estimation of the Telescopic Mast . . . . .	25
2.4 Simulation . . . . .	29
2.5 Experiment . . . . .	30
2.5.1 Experimental Setup . . . . .	30
2.5.2 Experimental Results . . . . .	33
2.6 Conclusion . . . . .	36
<b>3 Optimal Wrench Control utilizing Supporting Surface</b>	<b>37</b>
3.1 Introduction . . . . .	37
3.2 Problem Formulation . . . . .	43
3.2.1 System Modeling . . . . .	43
3.2.2 Control Objectives . . . . .	45
3.2.3 Proposed Framework . . . . .	49
3.3 Stiffness Analysis and Polytope Mappings . . . . .	50

3.3.1	Perturbation Analysis and Stiffness Matrices . . . . .	51
3.3.2	Polytope Mappings under $\xi_c(q) \in \mathcal{X}_c$ . . . . .	53
3.4	Design of Feedback Wrench Control . . . . .	57
3.5	Nominal Configuration and Active Stiffness Optimization . . . . .	59
3.5.1	Nominal Configuration Optimization . . . . .	60
3.5.2	Active Stiffness Optimization . . . . .	61
3.5.3	Optimization Structure . . . . .	64
3.5.4	Inverse Kinematics for Initial Variable . . . . .	65
3.6	Simulation . . . . .	67
3.6.1	Validation of Supporting Contact . . . . .	68
3.6.2	Simulation in Various Scenarios . . . . .	72
3.7	Experiment . . . . .	74
3.7.1	Experimental Setup . . . . .	74
3.7.2	Experimental Results . . . . .	78
3.7.2.1	Case 1 - Bilateral Holding . . . . .	78
3.7.2.2	Case 2 - Frictional Contact . . . . .	86
3.8	Conclusion . . . . .	93
<b>4</b>	<b>Conclusion</b> . . . . .	<b>95</b>
4.1	Summary . . . . .	95
4.2	Future Works . . . . .	98

# List of Figures

1.1	Examples of industrial operation and robotization for height environment operation. (a) Fuel replacement in nuclear power plants. (b) Dual-arm telerobotic system for fuel replacement in nuclear power plant [1, 2]. (c) JR-West humanoid robot for railway infrastructure maintenance [3]. (d) Live-wire powerline maintenance. (e) Dual-arm robotic system for live-wire powerline maintenance [4] . . . . .	2
2.1	Schematic description of the CANDU reactor. The manual driving mechanism is equipped at the fuel-loading machine, which consists of the clutch axis and driver shaft axis. . . . .	11
2.2	Dual-arm telerobotic system for height-operation in the nuclear power plant. The system consists of a dual-arm industrial manipulator, a long-reach mast with a telescopic structure, and a stage system with 2-DoF additional actuation (1-DoF rotational, 1-DoF translational actuation). . . . .	12
2.3	The flexibility of the telescopic mast can be modeled by adopting an elastic kinematic chain (EKC) modeling. Each adjacent segments (links) are connected through a 2-DoF universal joint, and the flexibility of the mast can be modeled by a torsional spring and damper at each joint. . . . .	16
2.4	The most 4 dominant vibration modes of the telescopic mast. . . . .	17
2.5	Estimation result for the 2-DoF mast-end horizontal position. . . . .	28
2.6	Snapshots of the right arm end-effector circular trajectory tracking simulation with the adoption of the proposed control framework. . . . .	28
2.7	Snapshots of the right arm end-effector circular trajectory tracking simulation with the impedance control in (2.27) . . . . .	28
2.8	Plots for the simulation of the right arm end-effector circular trajectory tracking. (a) Right arm end-effector error with the proposed control framework. (b) $x_s$ error with the proposed control framework. (c) Right arm end-effector error with the impedance control in (2.27). (d) $x_s$ error with the impedance control in (2.27). . . . .	29

2.9	(a) Mock-up environment of the CANDU reactor for fuel bundle realizing task. The manual driving mechanism is equipped at about a 10m height environment, and the driving tools are equipped at the end-effector of each manipulator. (b) The teleoperation setup for the control of the dual-arm telerobotic system. The user utilizes 6-DoF haptic devices for manipulator control and gets some visual feedback of the mock-up environment from system-mounted cameras. . . . .	31
2.10	Snapshots of the first scenario to check the vibration suppression performance under external disturbance. Excitation is performed in two different directions to check the control performance. . . . .	32
2.11	Snapshots of the second scenario to check the vibration suppression performance during the user command tracking. The system is required to follow the user command in two orthogonal directions to check the control performance. . . . .	33
2.12	Error plots of the 2-DoF horizontal position of the mast-stage system $x_s$ for the external disturbance excitation scenario. Plots in (a), (c) show the error when the vibration suppression control is adopted, and plots in (b), (d) show the error without the adoption of the vibration suppression control. . . . .	34
2.13	Error plots of the 2-DoF horizontal position of the mast-stage system $x_s$ for the user command tracking scenario. Plots in (a), (c) show the error when the vibration suppression control is adopted, and plots in (b), (d) show the error without the adoption of the vibration suppression control. . . . .	34
2.14	Snapshots of the 1mm-gap peg-in-hole task with the telerobotic system in mock-up environment of the nuclear power plant. . .	35
2.15	Snapshots of the 1mm-tolerance peg-in-hole task with the telerobotic system in mock-up environment of the nuclear power plant.	35
3.1	The interaction task of the dual-arm robotic system on the flexible base utilizing supporting contact. The system performs interaction tasks with one arm while maintaining supporting contact with the other arm. . . . .	39
3.2	The set of target task wrench data can be reformulated to the form of a desired wrench polytope $\mathcal{W}_e^d$ with its center $f_e^*$ and apexes $\delta f_e^i$ . . . . .	45

3.3	(a) 3D example of contact wrench set $\mathcal{W}_c$ for the bilateral holding constraint (e.g., hard grasping contact). (b) Contact wrench set $\mathcal{W}_c$ for the unilateral point constraint which is a friction cone with contact normal $n_c$ . (c) $\mathcal{W}_e^r(q^*)$ formulation from $\mathcal{W}_{\tau_a}$ . . . . .	47
3.4	The architecture of the proposed control framework. . . . .	50
3.5	Example of the polytope mappings under the supporting contact constraint: (a) $\mathcal{W}_e^r$ formulation. (b) $\mathcal{W}_e^c$ formulation. (c) $\mathcal{W}_e := \mathcal{W}_e^r \cap \mathcal{W}_e^c$ formulation. . . . .	56
3.6	Snapshot of the comparison between vibration suppression control and the proposed control framework utilizing supporting contact. (a) Force compensation with passivity-based vibration suppression control. (b) Force compensation with the proposed control framework utilizing supporting contact. . . . .	66
3.7	Results for the force compensation simulation in Fig. 3.6. (a)(b) End-effector position error and normalized joint torque results with passivity-based vibration suppression control. (c)(d) End-effector position error and normalized joint torque results with the proposed control framework utilizing supporting contact. . . . .	67
3.8	End-effector wrench polytope comparison with the existence of the supporting contact in two different views. . . . .	68
3.9	(a) Snapshot for the force tracking simulation with frictional contact. (b) Wrench polytope generation result. . . . .	69
3.10	Simulation results for the force tracking simulation in Fig. 3.9. (a) Task force tracking result. (b) Contact force. (c) Normalized joint torque. . . . .	69
3.11	(a) Snapshot for the force tracking simulation with bilateral holding. (b) Wrench polytope generation result. . . . .	70
3.12	Simulation results for the force tracking simulation in Fig. 3.11. (a) Task force tracking result. (b) Contact force. (c) Normalized joint torque. . . . .	70
3.13	(a) Snapshot for the force tracking simulation with pipe grasping in the perpendicular direction. (b) Wrench polytope generation result. . . . .	71
3.14	Simulation results for the force tracking simulation in Fig. 3.13. (a) Task force tracking result. (b) Contact force. (c) Normalized joint torque. . . . .	71
3.15	(a) Snapshot for the force tracking simulation with pipe grasping in the same direction. (b) Wrench polytope generation result. . . . .	71

3.16	Simulation results for the force tracking simulation in Fig. 3.15. (a) Task force tracking result. (b) Contact force. (c) Normalized joint torque. . . . .	71
3.17	(a) System setup of the dual-arm manipulator system on the flexible base. (b) Detail of the flexible base with IMU sensor attachment. . . . .	73
3.18	Environmental setup and the tool setup for the target task execution with the supporting contact. . . . .	73
3.19	Comparison between the optimized solution and the unoptimized variables in the case of the bilateral holding. (a) Visualization of the optimized configuration. (b) Wrench polytope generation result from the optimized solution. (c) Visualization of the unoptimized configuration. (d) Wrench polytope generation result from the unoptimized variables. . . . .	77
3.20	(a) Snapshots for the force tracking experiment with bilateral holding. (b) Wrench polytope generation result. . . . .	79
3.21	Experimental results for the force tracking with bilateral holding. (a) Task force tracking result. (b) Contact force. (c) Normalized left arm joint torque. (d) Normalized right arm joint torque. . . . .	80
3.22	(a) Snapshots of the drilling task with bilateral holding. (b) Wrench polytope generation result. . . . .	81
3.23	Experimental results for the drilling task with bilateral holding. (a) Task force tracking result. (b) Contact force. (c) Normalized left arm joint torque. (d) Normalized right arm joint torque. . . . .	82
3.24	Comparison between the optimized solution and the unoptimized variables in the case of the frictional contact. (a) Visualization of the optimized configuration. (b) Generated wrench polytopes from the optimized solution. (c) Visualization of the unoptimized configuration. (d) Generated wrench polytopes from the unoptimized variables. . . . .	85
3.25	Contact force comparison between the optimized solution and the unoptimized variables in the case of the frictional contact. The friction cone constraint ( $f_c^t \leq \mu f_c^n$ ) is violated at around 16s, 42s, 51s, and 79s such that slip occurs for the unoptimized case. . . . .	88
3.26	(a) Snapshots for the force tracking experiment with frictional contact. (b) Wrench polytope generation result. . . . .	89

3.27	Experimental results for the force tracking with frictional contact. (a) Task force tracking result. (b) Contact force. (c) Normalized left arm joint torque. (d) Normalized right arm joint torque. . . . .	90
3.28	(a) Snapshots of the drilling task with frictional contact. (b) Wrench polytope generation result. . . . .	91
3.29	Experimental results for the drilling task with frictional contact. (a) Task force tracking result. (b) Contact force. (c) Normalized left arm joint torque. (d) Normalized right arm joint torque. . .	92

# List of Tables

2.1	Singular values of $C_{q_f}$ from the mast excitation data. . . . .	17
3.1	Inertial parameter of the flexible base in Fig. 3.17 . . . . .	72
3.2	Optimization results for the case of bilateral holding . . . . .	76
3.3	Optimization results for the case of the frictional contact . . . . .	84

# Chapter 1

## Introduction

### 1.1 Motivation and Contribution

Industrial facilities often require regular inspection and emergency maintenance to ensure effective performance and safety. These maintenance tasks involve operations in the height environment, such as nuclear fuel magazine replacement, live-wire powerline maintenance, and other infrastructure maintenance tasks in various industrial fields. Despite the availability of skilled workers, these tasks are inherently dangerous, often resulting in fatalities and injuries. Thus, the robotization of such tasks is becoming increasingly desirable to replace the human resource for safety and efficiency. There have been active attempts at this robotization by many companies and research groups, by equipping the dual-arm manipulator system on the long-reach platform (e.g., telescopic mast) to access the height environment [1–4] (see Fig. 1.1). However, their robotization is challenging, as extending the platform to reach the high altitude itself often exhibits substantial flexibility. This flexibility arises from the compliance of the components (e.g., the flexibility of each link of the telescoping platform) as well as the assembly tolerance among the components (e.g., the gap at each link of the telescoping platform), which are accumulated

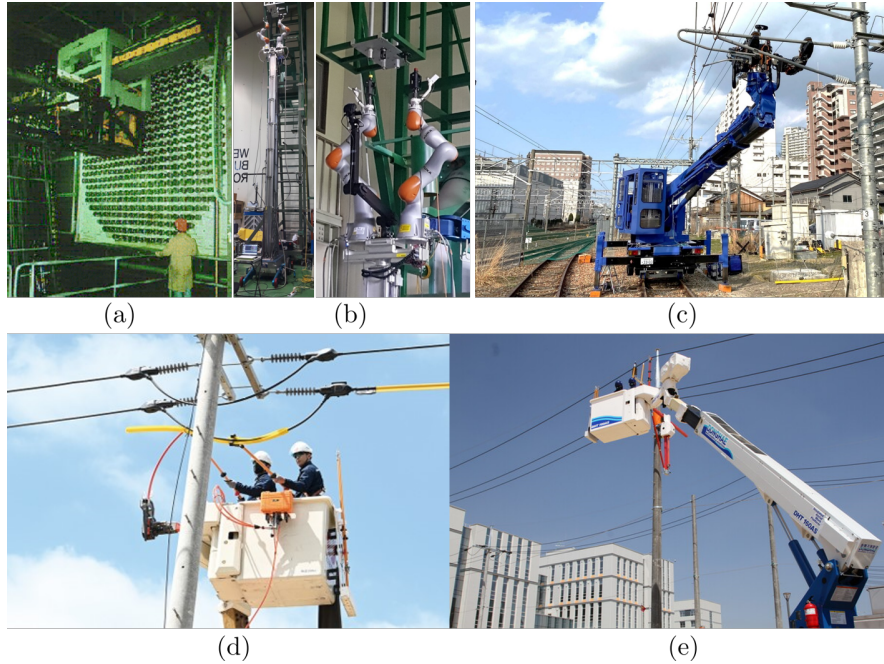


FIGURE 1.1: Examples of industrial operation and robotization for height environment operation. (a) Fuel replacement in nuclear power plants. (b) Dual-arm telerobotic system for fuel replacement in nuclear power plant [1, 2]. (c) JR-West humanoid robot for railway infrastructure maintenance [3]. (d) Live-wire powerline maintenance. (e) Dual-arm robotic system for live-wire powerline maintenance [4]

through the length of an extending platform, thereby, leading into substantial deviation and the vibration at the end of the platform. Since the target maintenance task requires high-force and high-precision operation (e.g., releasing the magazine, precision cutting and pushing-insertion of wire into connectors, pushing or pulling of infrastructure equipment, and industrial tool manipulation such as drilling and hammering), the flexibility issue becomes an even more significant concern. Thus, the control framework to resolve the flexibility issue should be developed to perform high-force/high-precision tasks in a height environment.

In this thesis, we consider the problem of how to achieve high-force/high-precision in-height robot operation on an extending platform with substantial end-flexibility. For this, we define two control problem scenarios: 1) motion control for high-precision tasks, and 2) force control for high-force tasks. The effect of flexibility on task performance appears in different ways in each control problem. For the first problem of motion control, the task performance is degraded by the vibration of the long-reach base, which arises from the motion of the manipulator and external disturbance. On the other hand, during high-force operation, flexibility can be a hurdle due to the deformation induced by the interaction wrench. Moreover, the system is under-actuated with only the dual-arm manipulator fully-actuated, while the flexible base lacks any control actuation such that the flexibility should be covered by under-actuated control input. For this, we propose a novel control framework to handle the flexibility issue during the high-precision/high-force in-height operation for the dual-arm robotic system on the flexible base. Our control consists of the following two main frameworks:

- Passivity-based vibration suppression control for precise operation: we propose a passivity-based control framework to attain precise end-effector motion while suppressing the vibration of the flexible base. To achieve two control objectives (precise end-effector motion tracking, vibration suppression), we adopt passive decomposition [5] to decompose the system dynamics into two orthogonal spaces: the end-effector of the flexible base and its orthogonal space. To resolve the under-actuation, we extract

a reduced model of the base end-motion and suppress the dominant end-motion of the base, while achieving precise motion of the manipulator system.

- Optimal wrench control utilizing supporting surface for high-force operation: we propose an optimal wrench control to attain high-force interaction tasks. To resolve the deformation issue during the high interaction wrench execution, we utilize the supporting surface. Inspired by the exploitation of supporting contact/surface by humans in daily life, we aim to attain high-force operation by one (right/working/interaction) arm while holding, or pushing on, the surface by the other (left/supporting/-contact) arm. Based on the prior information of the target task (task wrench set, supporting surface, etc), We first design the control as a combination of: 1) nominal control; 2) active stiffness control; and 3) feedback wrench control. We then sequentially perform optimizations of the nominal configuration (and its related wrenches) and the active stiffness control gain. We adopt quasi-static stiffness analysis considering supporting contact which enables the design of feedback wrench control and eases the calculation load of the optimization framework.

The effects of these two control frameworks are validated by the experimental results. For the first control problem of vibration suppression, we utilize a dual-arm telerobotic system on a telescopic mast in a mock-up environment of the nuclear power plant. For the second problem, we utilize the small-scale dual-arm system on a flexible base with the supporting surface provided. Our control frameworks show effective solutions for the flexibility issue, and enable high-precision/high-force operation in height-environment.

## 1.2 Related Works

### 1.2.1 Related Works of Vibration Suppression Control

There has been a long history of research into the control problem of single or multiple robot manipulators on a flexible base. These studies mainly focus on vibration suppression for various types of manipulator systems on a flexible base, for instance, flexible-macro/rigid-micro manipulator systems [6–11], flexible link manipulator systems [12–15], a single robotic arm mounted on a flexible fixed base [16–25], a robotic manipulator on a flexible beam with additional actuation [1, 2], and dual-arm humanoid on flexible mobile base [26, 27]. Early results propose a mixed control framework assuming a different time-scale motion between the flexible base and the manipulator such as augmented damping control [6–11, 16, 17] and singular perturbation [18], which may degrade the tracking performance due to the vibration damping control term in same control channel. Results in [21–23, 26, 27] utilize the redundancy to control the system motion and vibration suppression, but the system motion is restricted to the null space motion which doesn't affect the base vibration. Results in [13–15, 28] adopt a planning-based approach for vibration minimization, but are still limited to the mixed control approach and show computation issues.

While the above results adopt the mixed control approach for the whole system dynamics with dynamic coupling, there have been other control approaches to decompose the system dynamics (decouple the inertia coupling

of the whole system) and control each sub-system dynamics separately. Results in [24, 25] utilize the coupling force between two decomposed dynamics as a control for vibration suppression of the linear translational flexible base. Results in [1, 2] present a control framework that simultaneously performs manipulator tracking and vibration suppression of the 2D manipulator-stage system on the flexible beam utilizing a passivity-based dynamics decomposition [5]. The platform in [1, 2] is a small-scale testbed system of a telerobotic system for a nuclear power plant, and this thesis will extend this result to the dual-arm manipulator system on a flexible mast, which will be introduced in Chapter 2.

For the execution of our vibration suppression control framework, we need a state estimation framework to estimate the state of the flexible mast. This estimation should be calculated in a real-time manner using onboard sensing. Based on the EKC (elastic kinematic chain [29]) modeling of the flexible mast, there have been many studies to estimate the motion of EKC systems. Various approaches for this estimation are presented including vision-based estimation [30–32], utilization of electromagnetic sensor [33], and shape reconstruction techniques using Fiber Bragg Grating (FBG) sensors [34, 35]. However, these approaches suffer from computation issues or price issues of expensive sensors such that it is not applicable to the real-time estimation of the nonlinear high-DoF flexible mast. For that, we utilize a model-free estimation framework in [36] which utilizes only IMU sensors for real-time estimation.

### 1.2.2 Related Works of Wrench Control

While there have been many results about the control problem of manipulator systems on a flexible base, these results mainly show motion control performance with vibration suppression, and these results lack focus on force control strategies which are essential for the high-force interaction task. In this context, results in [37, 38] propose an impedance control strategy for the force control of a single manipulator system on a linear flexible base, yet rely on indirect force control within a simplified model, and there is still a lack of in-depth results to address the control problem of manipulator systems on flexible base for the high-force interaction task.

The control problem for high-force interaction tasks has been rather more actively investigated within humanoid robotics. While most of results in humanoid robotics focus on the problem of balancing [39–43] and Quadratic Programming (QP)-based contact wrench distribution [44–48] against measured (or estimated) interaction wrench, some studies have specifically targeted the application of high-force interaction tasks. Investigations into the heavy-object pushing task [49–54] exemplify this focus, with methodologies ranging from motion planning [49–51] to Model Predictive Control (MPC)-based approaches with pose optimization [52]. Additionally, results in [53, 54] leveraged additional supporting contacts to augment wrench capacity during the interaction. However, despite these advances in handling high-force interaction tasks, their approaches mainly rely on reduced dynamics (e.g., centroidal dynamics [55, 56]), which is typically adopted for the control of humanoid robots due to their high-DOFs, yet, fundamentally inapplicable for analyzing the effect

of the flexibility. These approaches only consider the approximated center of mass behavior and contact wrench constraints [57–60] during the control design, without a rigorous analysis of full system behavior with flexibility, system stability, joint angle, and torque limits [61, 62]. Also, there is a lack of explicit feedback wrench control approach for the desired task wrench execution. In contrast, our framework proposed in this paper is based on the full dynamics analysis of the system to manifest the complete effect of flexibility on the system behavior.

To evaluate the force feasibility of the system to perform high-force target tasks, the adoption of the equivalent performance measure is required. For that, we adopt the concept of the wrench polytope. The concept of wrench polytope has long been utilized to check the force capability with various names such as wrench polytope [63–66] for industrial manipulator, wrench-feasible workspace (WFW) [67, 68] for tendon tension in parallel cable robot, and the force manipulability ellipsoid [69, 70] which is a approximation of the wrench polytope. There also have been various approaches to adopting the wrench polytope to the locomotion problem of humanoid robots. The set of feasible contact forces is evaluated through the projection of friction cones (contact wrench cone (CWC) [57–60]) to simplified CoM dynamics, or joint torque limit of the system is also involved (actuation wrench polytope (AWP) [61, 62]) to find more sophisticated locomotion plan. The wrench polytope is adopted to the balancing control during the interaction task [54]. while these approaches of utilizing the concept of wrench polytope evaluate the balancing stability by projecting polytopes to the CoM dynamics, our research explicitly evaluates the task force feasibility by considering these wrench polytopes in full

dynamics and find relationship between these wrench capability performance measures.

As far as we know, our result in this thesis is the very first result for the high-force/high-precision interaction task control of the dual-arm system on the flexible base.

### **1.3 Outline**

The outline of this thesis is as follows. In chapter 1, we provide the motivation and the contribution of the thesis with a brief review of related research. In chapter 2, we propose a passivity-based vibration suppression control framework for high-precision operation utilizing dynamics decomposition and show some results for the application in a mock-up environment of the nuclear power plant. The optimal wrench control framework utilizing supporting surface for high-force operation is described in chapter 3, with stiffness analysis and optimization framework. The experimental validation for the wrench control framework is also presented in chapter 3. The conclusion and possible directions of future research will be provided in chapter 4.

# Chapter 2

## Passivity-based Vibration Suppression Control

### 2.1 Introduction

In this chapter, we consider the motion control problem for high-precision operation in height-environment. For this control problem, in this section, we consider the dual-arm telerobotic system on the telescopic mast for the maintenance task in a nuclear power plant. In Canada Deuterium Uranium (CANDU) reactor, a type of pressurized heavy-water reactor has a unique mechanism designed for the fuel-feeding operation; two fuel-loading machines feed the fuel bundle to the reactor during the plant operation. As the plant ages, the fuel bundle may be stuck in the fuel-feeding pressure tube in front of the calandria during the feeding process, which requires emergency operation to release the bundle. For this, a manual driving mechanism consisting of a clutch axis and a driver shaft axis is equipped at the fuel-loading machine (see Fig. 2.1). For the fuel bundle release, it is required to operate the clutch axis and the driver shaft axis simultaneously. Despite the participation of skilled human workers, the fuel-releasing task still has a high degree of difficulty and

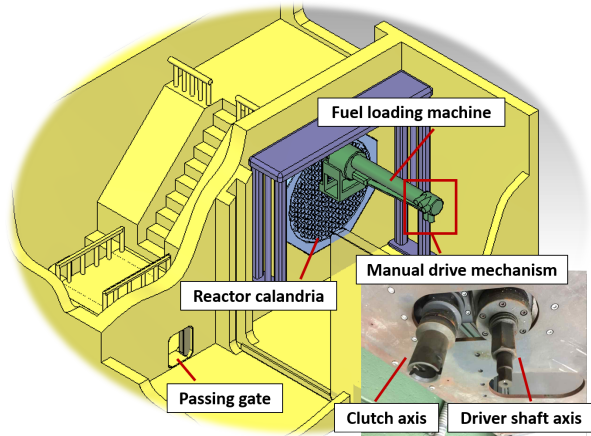


FIGURE 2.1: Schematic description of the CANDU reactor. The manual driving mechanism is equipped at the fuel-loading machine, which consists of the clutch axis and driver shaft axis.

risk for even skilled human workers due to the following properties. First, the internal environment of the reactor is a highly radioactive environment, which is hazardous to human technicians. Second, the manual drive mechanism is equipped at a height environment (about 10m), and the skilled human worker should utilize the specific device attached to the very long rod. If the emergency manual release is failed, the reactor should be shut down. It takes much time to wait until the radiation dose inside the plant decreases for the task. It is required to operate the manual drive mechanism with sufficient torque capacity, and the tight tolerance (mm-scale tolerance) between the tool and the clutch/driver shaft axis further increases the difficulty of the task.

For that, a novel dual-arm telerobotic system is developed based on results in [71, 72] as shown in Fig. 2.2. The proposed telerobotic system attaches a dual-arm industrial manipulator to the mobile platform with a telescopic mast for height operation in the nuclear power plant. The system can reach

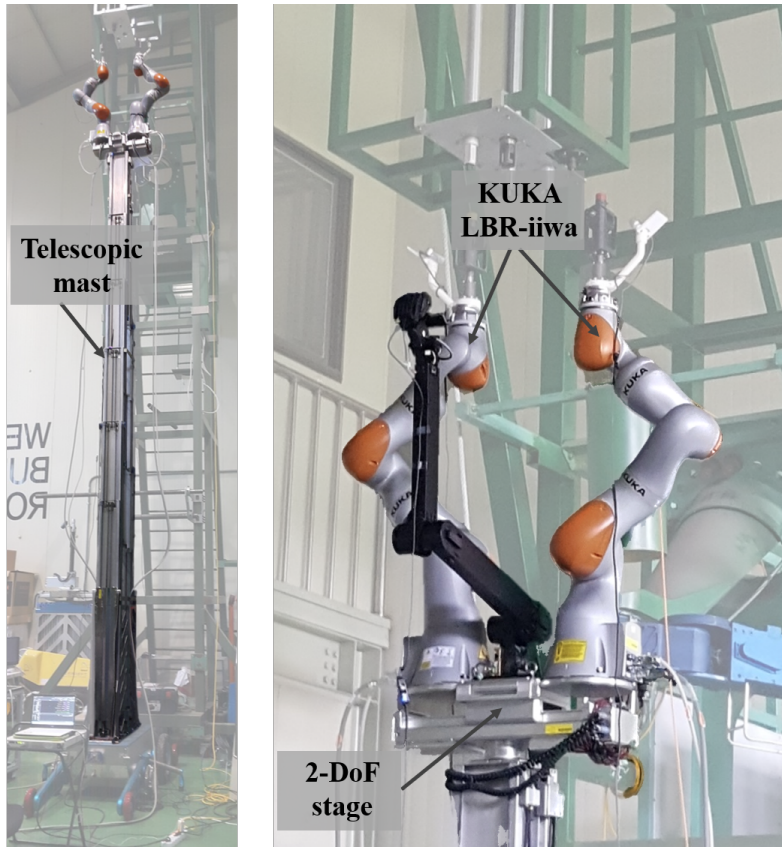


FIGURE 2.2: Dual-arm telerobotic system for height-operation in the nuclear power plant. The system consists of a dual-arm industrial manipulator, a long-reach mast with a telescopic structure, and a stage system with 2-DoF additional actuation (1-DoF rotational, 1-DoF translational actuation).

the height-environment target workspace by expanding the telescopic mast. During the target task (fuel bundle releasing task) operation, the telescopic mast is elevated up to about 10m height, and the flexibility resulting from the gaps between each mast segment cannot be ignored. The flexibility of the telescopic mast causes vibration during the operation. This vibration comes from the motion of the actuated part (manipulator and the stage system), due to the dynamic coupling between the mast and the actuated part of the system. Also, external disturbance can affect the vibration of the mast.

To resolve the vibration of the telescopic mast, this chapter is devoted to designing a novel vibration suppression control framework for precise target task operation. The control goal is to attain the desired motion tracking and suppression of the mast vibration. To achieve these two control objectives simultaneously, we adopt the passive decomposition [5]. This passive decomposition enables the decoupling of the system dynamics into two subsystems; the dynamics of the mast motion and its orthogonal complement (including manipulator motion). Based on the decoupled dynamics, we can separately design two control inputs for motion tracking and vibration suppression. For this control design, we should consider the under-actuation of the system, where the telescopic mast is under-actuated and the control should be allocated to only fully-actuated manipulator control inputs. Also, the scale of mast inertia and the vibration is different from that of manipulator inertia and motion. For that, we utilize an additional actuated system. A stage system with 2-DoF actuation (1-DoF rotational, 1-DoF translational actuation) is equipped between the mast and the dual-arm manipulator as shown in Fig. 2.2. This stage system is used for vibration suppression control, and due to under-actuation, the

stage stabilizes only the 2-DoF horizontal position of the mast end-effector. This control strategy is reasonable because the vibration of the mast can be reduced to specific dominant vibration modes, and the remaining vibration modes can be stabilized by the compliance of the mast. While the vibration suppression is performed by the stage system, the dual-arm system is controlled to attain precise target task operation. This control approach based on passive decomposition has been previously explored in previous studies in [1, 2], which propose a control framework for a single manipulator-stage system on the aluminum beam emulating our telerobotic system on a small scale. Results in [1, 2] similarly decompose the dynamics to suppress the beam vibration with the linear stage system while the remaining motion (manipulator motion) is controlled separately, but the control is adopted to the planar system with a linear beam model in the planar and low DoF (7-DoF) system. We extend this approach to a high-DoF (28 DoF) nonlinear system with a dual-arm manipulator for practical application to the maintenance tasks in the nuclear power plant.

The rest of this chapter is organized as follows. Sec. 2.2 define the problem formulation with the system modeling. Sec. 2.3 presents the control design based on the passive decomposition and an estimation framework for the mast state estimation. The experimental validation is performed and validation results are described in Sec. 2.5, and the conclusion is followed by in Sec. 2.6.

## 2.2 Problem Formulation

### 2.2.1 System Modeling

The dynamics of the dual-arm manipulator system on the telescopic mast in Fig. 2.2 can be expressed by

$$M(q)\ddot{q} + C(q, \dot{q})\dot{q} + G(q) + \mathcal{S}_f\tau_f = \mathcal{S}_a\tau_a + J_e^T(q)f_e \quad (2.1)$$

where  $q = [q_f; q_a] \in \mathbb{R}^n$  is the system configuration with  $q_f \in \mathbb{R}^{n_f}$  and  $q_a = [q_s; q_l; q_r] \in \mathbb{R}^{n_a}$  respectively being the configurations of the flexible base and that of the actuated joints. Actuated joints consist of the dual-arm manipulator configuration  $[q_l; q_r] \in \mathbb{R}^{2n_r}$  and the configuration of the stage system  $q_s \in \mathbb{R}^{n_s}$ ;  $M(q)$ ,  $C(q, \dot{q}) \in \mathbb{R}^{n \times n}$ , and  $G(q) \in \mathbb{R}^n$  are the inertia, Coriolis, and gravity matrices of the system;  $\tau_f$  is the compliance of the (un-actuated) flexible base as given by

$$\tau_f = B_f(q_f)\dot{q}_f + K_f(q_f)[q_f - q_f^0]$$

where  $B_f(q_f) \in \mathbb{R}^{n_f \times n_f}$  and  $K_f(q_f) \in \mathbb{R}^{n_f \times n_f}$  are the damping and stiffness matrices with  $q_f^0 \in \mathbb{R}^{n_f}$  being an equilibrium configuration; and  $\tau_a \in \mathbb{R}^{n_a}$  is the control actuation for the (fully-actuated) dual-arm manipulator and the stage system, which is to be designed below. The matrices  $\mathcal{S}_f \in \mathbb{R}^{n \times n_f}$  and  $\mathcal{S}_a \in \mathbb{R}^{n \times n_a}$  are the selection matrices as defined by

$$\mathcal{S}_f = \begin{bmatrix} I_{n_f} \\ 0_{n_a \times n_f} \end{bmatrix} \in \mathbb{R}^{n \times n_f}, \quad \mathcal{S}_a = \begin{bmatrix} 0_{n_f \times n_a} \\ I_{n_a} \end{bmatrix} \in \mathbb{R}^{n \times n_a} \quad (2.2)$$

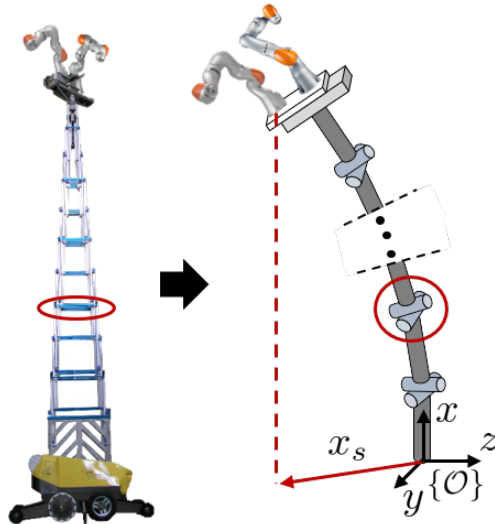


FIGURE 2.3: The flexibility of the telescopic mast can be modeled by adopting an elastic kinematic chain (EKC) modeling. Each adjacent segments (links) are connected through a 2-DoF universal joint, and the flexibility of the mast can be modeled by a torsional spring and damper at each joint.

### 2.2.2 Flexibility Modeling of the Telescopic Mast

The telescopic mast exhibits the flexibility induced by the assembly tolerance among each adjacent segment of the telescopic structure. Following this, we adopt an elastic kinematic chain (EKC) system modeling [29] where each link is connected by a 2-DoF universal joint as described in Fig. 2.3. The flexibility of the mast can be modeled as a torsional spring and damper equipped at each joint. The telescopic mast in Fig. 2.2 consists of 7 rigid segments, and we can adopt 12-DoF EKC modeling considering that the first segment is fixed at the mobile base. We set the equilibrium configuration  $q_f^0 = 0$ , and stiffness and damping matrices  $B_f(q_f)$  and  $K_f(q_f)$  are estimated by parameter identification assuming constant values. This assumption is reasonable because of the slight flexible motion near the  $q_f^0 = 0$ .

$\sigma_1$	$\sigma_2$	$\sigma_3$	$\sigma_4$
$6.906 \times 10^{-5}$	$6.975 \times 10^{-6}$	$2.639 \times 10^{-6}$	$9.353 \times 10^{-7}$
$\sigma_5$	$\sigma_6$	$\sigma_7$	$\sigma_8$
$4.368 \times 10^{-7}$	$2.386 \times 10^{-7}$	$1.575 \times 10^{-7}$	$7.614 \times 10^{-8}$
$\sigma_9$	$\sigma_{10}$	$\sigma_{11}$	$\sigma_{12}$
$5.742 \times 10^{-8}$	$3.977 \times 10^{-8}$	$3.112 \times 10^{-8}$	$1.399 \times 10^{-8}$

TABLE 2.1: Singular values of  $C_{qf}$  from the mast excitation data.

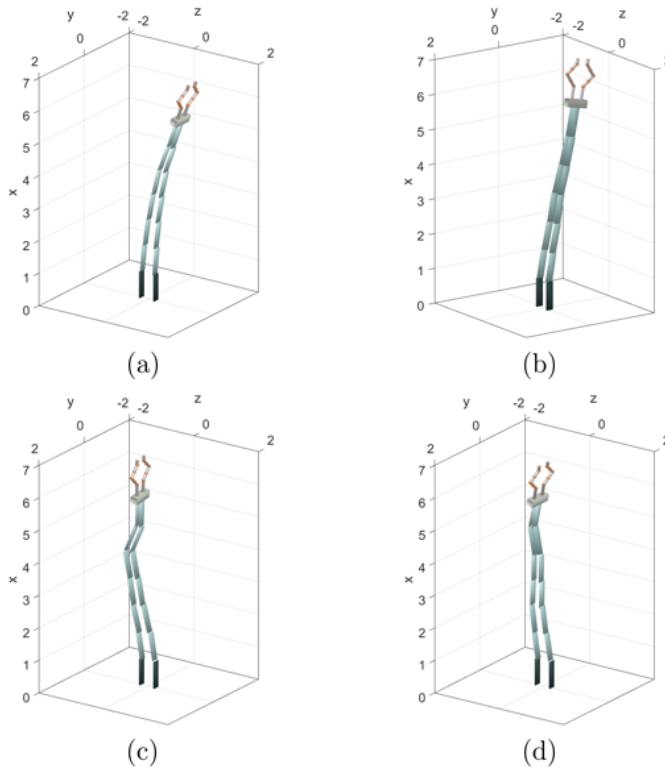


FIGURE 2.4: The most 4 dominant vibration modes of the telescopic mast.

While this high-DoF EKC modeling adoption is reasonable for the telescopic mast motion, the actual vibration of the mast can be approximated with the combination of specific dominant vibration modes. To find these dominant vibration modes, we adopt proper orthogonal decomposition (POD) [73]. This

POD process can be performed by obtaining motion data emulating target task operation. By obtaining sufficient data on the mast motion, we can calculate the covariance of the mast state with its singular value decomposition result expressed by

$$C_{q_f} = \frac{1}{N} \sum_{k=1}^N \tilde{q}_{f,k} \tilde{q}_{f,k}^T = U \Sigma U^T \quad (2.3)$$

where  $\tilde{q}_{f,k}$  is an error state of the mast from the equilibrium state at k-th time step,  $U \in \mathfrak{R}^{n_f \times n_f}$  is proper orthogonal modes (POMs) and  $\Sigma \in \mathfrak{R}^{n_f \times n_f}$  is a diagonal matrix composed of singular values in descending order ( $\sigma_1 \geq \sigma_2 \geq \dots \geq \sigma_{n_f}$ ). The result of this singular value decomposition is described in Table. 2.1. Following this result, we can decompose the mast state into dominant and non-dominant modes, and the most 4 dominant vibration modes can be extracted as shown in Fig. 2.4.

## 2.3 Design of Vibration Suppression Control

### 2.3.1 Control Objectives

Our control objectives for the high-precision operation can be summarized as follows:

- Vibration suppression of the telescopic mast induced by the manipulator (and stage system) motion and the external disturbance.

- Desired trajectory control for precise motion of the system to perform tight-tolerance desired operation. The target operation in this section is to perform the fuel bundle realizing task, and we aim to attain a one-arm desired trajectory tracking to connect the task tool (one-arm end-effector) to the driving mechanism.

To achieve these two distinct objectives simultaneously, we propose a control strategy based on passive decomposition. The estimation framework for the mast state estimation will be briefly presented in the following.

### 2.3.2 Passive Decomposition

Let's recall the dynamics of the dual-arm telerobotic system in (2.1). Analyzing the structure of the dynamics, we can reformulate (2.1) by

$$\begin{aligned}
\begin{bmatrix} M_f & M_{fa} \\ M_{af} & M_a \end{bmatrix} \begin{bmatrix} \ddot{q}_f \\ \ddot{q}_a \end{bmatrix} + \begin{bmatrix} C_f & C_{fa} \\ C_{af} & C_a \end{bmatrix} \begin{bmatrix} \dot{q}_f \\ \dot{q}_a \end{bmatrix} + \begin{bmatrix} G_f \\ G_a \end{bmatrix} \\
+ \begin{bmatrix} B_f \dot{q}_f + K_f q_f \\ 0 \end{bmatrix} = \begin{bmatrix} 0 \\ \tau_a \end{bmatrix} + \begin{bmatrix} J_{e,f}^T f_e \\ J_{e,a}^T f_e \end{bmatrix} \quad (2.4)
\end{aligned}$$

The hurdle for our control design is a dynamics coupling (inertia & Coriolis coupling) terms between the dynamics of the mast and actuated system, such that the motion of the manipulator system and the stage system affects the mast vibration with coupling force  $M_{fa}\ddot{q}_a + C_{fa}\dot{q}_a$ .

To eliminate this dynamics coupling term, we need a dynamics decomposition strategy to decouple the dynamics and control them separately. For that, we adopt a passive decomposition [5]. The main idea of the passive decomposition is to decompose the dynamics such that the inertia coupling terms between decomposed dynamics are eliminated, and preserve the passivity of each decomposed dynamics. Let us first consider the general n-DoF multibody system with dynamics

$$M(q)\ddot{q} + C(q, \dot{q})\dot{q} + G(q) = \tau + J(q)^T f \quad (2.5)$$

the specific target space to be controlled defined by

$$h(q) : \mathbb{R}^n \rightarrow \mathbb{R}^m \quad (2.6)$$

Then, we can consider the two aspects of the motion: 1) formation aspect, which considers the  $h(q)$  motion in the manifold, and 2) maneuver aspect which is a motion on the level set  $h(q) = c$ . Following this, we decompose the tangent space (motion space) and the cotangent space (force space) decomposed by

$$T_q\mathcal{M} = \Delta_{\top} \oplus \Delta_{\perp}, \quad T_q^*\mathcal{M} = \Omega_{\top} \oplus \Omega_{\perp} \quad (2.7)$$

and the equivalent space decomposition can be expressed by

$$\dot{q} = \begin{bmatrix} \Delta_{\top} & \Delta_{\perp} \end{bmatrix} \begin{bmatrix} \nu_L \\ \nu_E \end{bmatrix}, \quad \tau = \begin{bmatrix} \Omega_{\top}^T & \Omega_{\perp}^T \end{bmatrix} \begin{bmatrix} \tau_L \\ \tau_E \end{bmatrix} \quad (2.8)$$

where  $\Omega_{\perp} = \frac{\partial h}{\partial q}$ ,  $\Delta_{\top} = \text{Null}(\Omega_{\perp})$ ,  $\Delta_{\perp} = M^{-1}\Omega_{\perp}^T(\Omega_{\perp}M^{-1}\Omega_{\perp}^T)^{-1}$ ,  $\Omega_{\top} =$

$(\Delta_{\top}^T M \Delta_{\top})^{-1} \Delta_{\top}^T M$  and  $\nu_E = \frac{dh}{dt}$ . Then applying (2.8), (2.5) can be decomposed by

$$\begin{bmatrix} M_L & 0 \\ 0 & M_E \end{bmatrix} \begin{bmatrix} \dot{\nu}_L \\ \dot{\nu}_E \end{bmatrix} + \begin{bmatrix} C_L & C_{LE} \\ C_{EL} & C_E \end{bmatrix} \begin{bmatrix} \nu_L \\ \nu_E \end{bmatrix} + \begin{bmatrix} G_L \\ G_E \end{bmatrix} = \begin{bmatrix} \tau_L \\ \tau_E \end{bmatrix} + \begin{bmatrix} f_L \\ f_E \end{bmatrix} \quad (2.9)$$

The upper dynamics represent the locked system dynamics which describes the maneuver aspect, and the lower dynamics represent the shape system dynamics which describes the formation aspects. Each dynamics satisfies the passivity (i.e.  $\dot{M}_E - 2C_E$  and  $\dot{M}_L - 2C_L$  are skew-symmetric matrices) such that the standard control framework can be freely designed for each dynamics separately. For more details about the passive decomposition, see [5].

### 2.3.3 Control Design

Applying the passive decomposition for our control objectives, we can separately design the vibration suppression control and motion tracking control. For this control design, we have to consider the under-actuation of the system such that the mast motion cannot be controlled directly due to no actuation. Also, due to the different scale of motion and inertia between the mast and the dual-arm manipulator system, the dual-arm manipulator system is not suitable for vibration suppression such that only the 2-DoF stage system is allocated for the vibration suppression.

To suppress the mast vibration with the stage system avoiding the under-actuation issue, we define the 2-DoF horizontal position of the mast-stage

subsystem as described in Fig. 2.3 which can be expressed by

$$h(q) = h(q_f, q_s) = h(q_{base}) = x_s(q_{base}) = [x_s^y, x_s^z] \in \mathbb{R}^{n_e} \quad (2.10)$$

where we define  $q_{base} = [q_f; q_s] \in \mathbb{R}^{n_f+n_s}$  as an augmented configuration of the mast and the stage system,  $x_s \in \mathbb{R}^{n_e}$  ( $n_e = 2$ ) We only consider the 2-DoF motion to enable fully-actuated control with the stage input, and this reduction is reasonable considering the actual vibration modes of the mast system consist of 4 dominant modes as shown in Sec. 2.2.2, and the singular value ratio  $\frac{\sum_{i=1}^2 \sigma_i}{\sum_{i=1}^{n_f} \sigma_i} = 0.943$  for the first 2 dominant modes such that the most of the mast vibration can be stabilized through the stage input.

From that, we can adapt the passive decomposition in (2.8) with

$$\Omega_{\perp} = \frac{\partial x_s(q_{base})}{\partial q} = \begin{bmatrix} \frac{\partial x_s(q_{base})}{\partial q_{base}} & 0_{n_e \times 2n_r} \end{bmatrix} = \begin{bmatrix} J_s^{fs} & 0_{n_e \times 2n_r} \end{bmatrix} \in \mathbb{R}^{n_e \times n} \quad (2.11)$$

$$\Delta_{\top} = \text{Null}(\Omega_{\perp}) = \begin{bmatrix} \text{Null}(J_s^{fs}) & 0 \\ 0 & I_{2n_r} \end{bmatrix} \in \mathbb{R}^{n \times (n-n_e)} \quad (2.12)$$

with  $\nu_E = \frac{dh}{dt} = \dot{x}_s$ . The locked system velocity  $\nu_L = [\nu_f; \dot{q}; \dot{q}_r] \in \mathbb{R}^{n-n_e}$  which consists of the internal mast motion  $\nu_f$  and the motion of the dual-arm system.

Then, the decomposed dynamics can be expressed by

$$\begin{bmatrix} M_L & 0 \\ 0 & M_E \end{bmatrix} \begin{bmatrix} \dot{\nu}_L \\ \dot{\nu}_E \end{bmatrix} + \begin{bmatrix} C_L & C_{LE} \\ C_{EL} & C_E \end{bmatrix} \begin{bmatrix} \nu_L \\ \nu_E \end{bmatrix} + \begin{bmatrix} G_L \\ G_E \end{bmatrix} + \begin{bmatrix} \Delta_L \\ \Delta_E \end{bmatrix} = \begin{bmatrix} \tau_L \\ \tau_E \end{bmatrix} + \begin{bmatrix} f_L \\ f_E \end{bmatrix} \quad (2.13)$$

where  $\Delta_L = \Delta_{\top}^T \mathcal{S}_f(B_f \dot{q} + K_f q_f)$  and  $\Delta_E = \Delta_{\perp}^T \mathcal{S}_f(B_f \dot{q} + K_f q_f)$  represent the mast compliance projection to the locked system dynamics and the shape system dynamics, and  $f_L = \Delta_{\top}^T J_e^T f_e$  and  $f_E = \Delta_{\perp}^T J_e^T f_e$  represent the external wrench projection to the locked system dynamics and the shape system dynamics. The decomposed control can be expressed by

$$\tau_E = \Delta_{\perp}^T \mathcal{S}_a \tau_a = \mathcal{D}_E^s \tau_s + \mathcal{D}_E^l \tau_l + \mathcal{D}_E^r \tau_r \quad (2.14)$$

$$\tau_L = \Delta_{\top}^T \mathcal{S}_a \tau_a = \mathcal{D}_L^s \tau_s + \mathcal{S}_l \tau_l + \mathcal{S}_r \tau_r \quad (2.15)$$

where  $\mathcal{S}_l = [0_{n_f \times n_l}; I_{n_r}; 0_{n_r}]$  and  $\mathcal{S}_r = [0_{n_f \times n_l}; 0_{n_r}; I_{n_r}]$ . For the vibration suppression control design, recall the shape system dynamics by

$$\begin{aligned} M_E \ddot{x}_s + C_E \dot{x}_s + C_{EL} \nu_L + G_L + \Delta_{\perp}^T \mathcal{S}_f(B_f \dot{q} + K_f q_f) \\ = \mathcal{D}_E^s \tau_s + \mathcal{D}_E^l \tau_l + \mathcal{D}_E^r \tau_r + f_E \end{aligned} \quad (2.16)$$

We adopt a passivity-based control approach to robustly suppress the vibration with system uncertainties. Following this, the stage control is expressed by

$$\begin{aligned} \tau_s = \mathcal{D}_E^{s\dagger} [C_{EL} \nu_L + G_L + \Delta_{\perp}^T \mathcal{S}_f(B_f \dot{q} + K_f q_f) - \mathcal{D}_E^l \tau_l - \mathcal{D}_E^r \tau_r] \\ - \mathcal{D}_E^{s\dagger} [-B_E \dot{x}_s - K_E (x_s - x_s^d)] \end{aligned} \quad (2.17)$$

where  $\mathcal{D}_E^{s\dagger} = D_{\tau} \mathcal{D}_E^{sT} (\mathcal{D}_E^s D_{\tau} \mathcal{D}_E^{sT})^{-1} \in \mathbb{R}^{n_s \times n_s}$  is the weighted pseudo-inverse of  $\mathcal{D}_E^s$  with the weight matrix  $D_{\tau} = \text{diag}[\tau_1^{lim}, \tau_2^{lim}] \in \mathbb{R}^{n_s \times n_s}$  based on the

base control limit  $\tau_i^{lim} := \frac{\bar{\tau}_i - \underline{\tau}_i}{2}$ . Matrices  $B_E, K_E \in \mathbb{R}^{n_s \times n_s}$  are damping and stiffness control gain for the stabilization to desired stage horizontal position  $x_s^d$ . Then the closed-loop dynamics of (2.16) under (2.17) is given by

$$M_E \ddot{x}_s + C_E \dot{x}_s + B_E \dot{x}_s + K_E (x_s - x_s^d) = f_E \quad (2.18)$$

The remaining internal motion of the stage-mast subsystem is stabilized with intrinsic stiffness and damper of the telescopic mast while the shape dynamics is stabilized with the stage input ( $\tau_s \in \mathbb{R}^2$ ). With the stage-mast subsystem stabilization ( $\dot{x}_s, \nu_f \rightarrow 0$ ), we can approximate the mast-stage system as a fixed base and then we only need to consider the motion of the manipulator. Consider the remaining manipulator dynamics converged by

$$M_{l,r}(q)\ddot{q}_{l,r} + C_{l,r}(q, \dot{q})\dot{q}_{l,r} + G_{l,r}(q) = \tau_{l,r} \quad (2.19)$$

and the control can be designed by

$$\tau_{l,r} = M_{l,r}(q)\ddot{q}_{l,r}^d + C_{l,r}(q, \dot{q})\dot{q}_{l,r}^d - B_{l,r}(\dot{q}_{l,r} - \dot{q}_{l,r}^d) - K_{l,r}(q_{l,r} - q_{l,r}^d) + G_{l,r}(q) \quad (2.20)$$

where  $q_{l,r}^d, \dot{q}_{l,r}^d, \ddot{q}_{l,r}^d \in \mathbb{R}^{n_r}$  represent the desired configuration, and  $B_{l,r}, K_{l,r} \in \mathbb{R}^{n_r \times n_r}$  are damping and stiffness control gain for the desired trajectory tracking. With this passivity-based control, we can achieve  $q_{l,r} \rightarrow q_{l,r}^d$  with the following closed-loop dynamics

$$\begin{aligned} M_{l,r}(q)(\ddot{q}_{l,r} - \ddot{q}_{l,r}^d) + C_{l,r}(q, \dot{q})(\dot{q}_{l,r} - \dot{q}_{l,r}^d) \\ + B_{l,r}(\dot{q}_{l,r} - \dot{q}_{l,r}^d) + K_{l,r}(q_{l,r} - q_{l,r}^d) = 0 \end{aligned} \quad (2.21)$$

### 2.3.4 State Estimation of the Telescopic Mast

Our proposed control approach analyzes the whole system dynamics and utilizes system states for the passivity-based feedback control, and this requires the estimation of states of the dual-arm telerobotic system. While the states of the dual-arm system and the stage system can be easily estimated using embedded joint sensors and encoders, there should be a certain framework to estimate the mast states, which does not have any actuation and encoder. To estimate the mast states (i.e. top-end position, joint angle), there exist two key issues. First, it is impossible to utilize the MOCAP (motion capture) system in a high-radiation nuclear power plant, so an onboard sensing strategy is indispensable. Second, the telescopic mast is modeled as a high-DoF nonlinear EKC model, and due to its complexity, it is challenging to manage the model-based estimation process in real time.

For that, we adopt a novel state estimation framework with only onboard sensing (IMU sensor attached to each segment of the mast) [36]. To account for the high DoF and nonlinear properties of the telescopic mast, we adopt a model-free estimation approach with model reduction. By extracting reduced vibration modes of the mast, we estimate the mast end-effector position with a minimum number of onboard sensors. More details are presented in [36].

The first process is to reduce the model of the mast motion to extract the dominant vibration modes. This process is described in Sec. 2.2.2. Based on this model reduction process, the state can be decoupled into dominant and

non-dominant modes.

$$\begin{aligned}\tilde{q}_f(t) &= U\xi(t) = [U_1 \ U_2] \begin{bmatrix} \xi_1(t) \\ \xi_2(t) \end{bmatrix} \\ &= U_1\xi_1(t) + U_2\xi_2(t)\end{aligned}\tag{2.22}$$

where  $U_1 \in \mathfrak{R}^{n_f \times r}$  and  $\xi_1(t) \in \mathfrak{R}^r$  are dominant modes and dominant states, and non-dominant modes and non-dominant states are denoted by  $U_2 \in \mathfrak{R}^{n_f \times (n_f - r)}$  and  $\xi_2(t) \in \mathfrak{R}^{n_f - r}$ . We can consider the dominant states  $U_1\xi_1(t)$  as the reduced state of the system, and the non-dominant states  $U_2\xi_2(t)$  can be regarded as a noise. As described in Sec. 2.2.2, there exist 4 most dominant vibration modes for the mast system ( $r = 4$ ), and  $\frac{\sum_{i=1}^r \sigma_i}{\sum_{i=1}^{n_f} \sigma_i} = 0.987$  such that this reduced 4 modes represent most of the mast vibration.

We can now choose the number of onboard sensors (IMU sensor for our application) based on the result of the mast model reduction. For that, we consider the measurement model of the IMU sensor by

$$y_{q_f}(t) = H\tilde{q}_f(t) + w(t) \in \mathfrak{R}^m, \quad w(t) \sim \mathcal{N}(0, C_w)\tag{2.23}$$

where  $H \in \mathfrak{R}^{m \times n_f}$  represent a mapping matrix for the IMU sensor placement to the mast and  $w(t) \in \mathfrak{R}^m$  represent the measurement noise with zero-mean Gaussian and covariance  $C_w \in \mathfrak{R}^{m \times m}$ . Thanks to the model reduction, we only have to attach the minimum number of IMU sensor satisfying  $m \geq r$ . With the decision of the IMU sensor number for the estimation, we have to optimize the sensor placement to maximize the estimation performance. This

sensor placement optimization is expressed by

$$\begin{aligned} H^* &= \underset{H}{\operatorname{argmin}} \operatorname{tr}(C_{e_\psi}) \\ &\text{subj. to } H \in \Omega \end{aligned} \quad (2.24)$$

where  $\psi \in \mathbb{R}^2$  represent the estimation output (2-DoF horizontal mast-end position for  $x_s$  in Sec. 2.3.3),  $\Omega$  is a set of possible sensor placement mapping matrices  $H$ , and  $C_{e_\psi} \in \mathfrak{R}^{q \times q}$  represent the covariance matrix of the output estimation error.

Based on these results, we aim to estimate the mast-end position  $\psi(t)$ . For that, we reconstruct the measurement model of  $\psi(t)$  based on POD result in (2.22), measurement model (2.23), and linearized relationship between  $\psi(t)$  and  $q_f$ . This can be expressed by

$$y_\psi(t) = \hat{S}U_1\hat{\xi}_1(t) = \hat{S}U_1\tilde{U}_1^\dagger y_{q_f} \quad (2.25)$$

Also, we can find the stochastic model of the output measurement, which is  $y_\psi \sim \mathcal{N}(\tilde{\psi}, C_{e_{y_\psi}})$  from [36]. Consequently, with the knowledge of prior distribution and measurement of the output, we may apply maximum a posteriori (MAP) estimation to obtain optimal output estimation as

$$\begin{aligned} \hat{\tilde{\psi}} &= \underset{\tilde{\psi}}{\operatorname{argmax}} p(\tilde{\psi}|y_\psi) = \underset{\tilde{\psi}}{\operatorname{argmax}} p(y_\psi|\tilde{\psi})p(\tilde{\psi}) \\ &= (C_{e_{y_\psi}}^{-1} + C_{\tilde{\psi}}^{-1})^{-1}C_{e_{y_\psi}}^{-1}y_\psi \end{aligned} \quad (2.26)$$

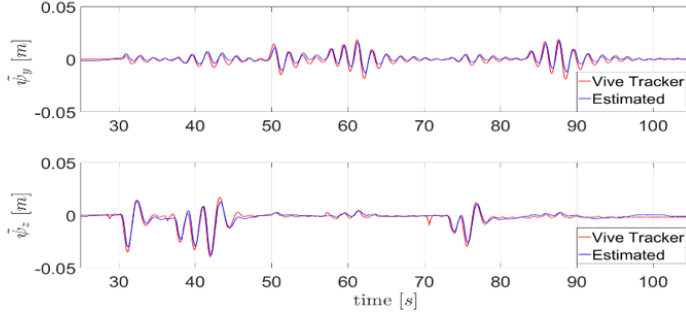


FIGURE 2.5: Estimation result for the 2-DoF mast-end horizontal position.



FIGURE 2.6: Snapshots of the right arm end-effector circular trajectory tracking simulation with the adoption of the proposed control framework.



FIGURE 2.7: Snapshots of the right arm end-effector circular trajectory tracking simulation with the impedance control in (2.27)

We apply this model-free estimation framework to estimate the 2-DoF mast-end horizontal position. We utilize HTC Vive Tracker for the ground truth measurement, and the estimation result with 2 IMU sensors is shown in Fig. 2.5. The proposed estimation framework ensures accurate mast state estimation (RMS 2.82mm error for the telescopic mast top-end position) using only 2 IMU sensors.

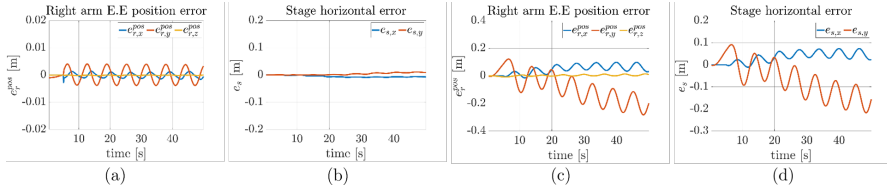


FIGURE 2.8: Plots for the simulation of the right arm end-effector circular trajectory tracking. (a) Right arm end-effector error with the proposed control framework. (b)  $x_s$  error with the proposed control framework. (c) Right arm end-effector error with the impedance control in (2.27). (d)  $x_s$  error with the impedance control in (2.27).

## 2.4 Simulation

We first propose the simulation result to validate the efficacy of the proposed vibration suppression control framework. For the simulation, the right arm end-effector of the dual-arm telerobotic system in Fig. 2.2 is required to follow the desired circular trajectory. For the comparison, we adopt impedance control for the actuated space expressed by

$$\tau_a = G_a(q) - B_a(\dot{q}_a - \dot{q}_a^d) - K_a(q_a - q_a^d) \quad (2.27)$$

where the desired trajectory of the dual-arm manipulator is designed to follow the desired trajectory assuming fixed base and the desired trajectory of the state system is a zero configuration. Results of the simulation are shown in Fig. 2.6, Fig. 2.7 and Fig. 2.8. As shown in Fig. 2.6 and Fig. 2.8-(a),(b), the right arm end-effector of the system follows the desired trajectory while suppressing the vibration of  $x_s$  while the impedance control in (2.27) cannot follow the desired trajectory with the increasing vibration of  $x_s$  as shown in Fig. 2.7

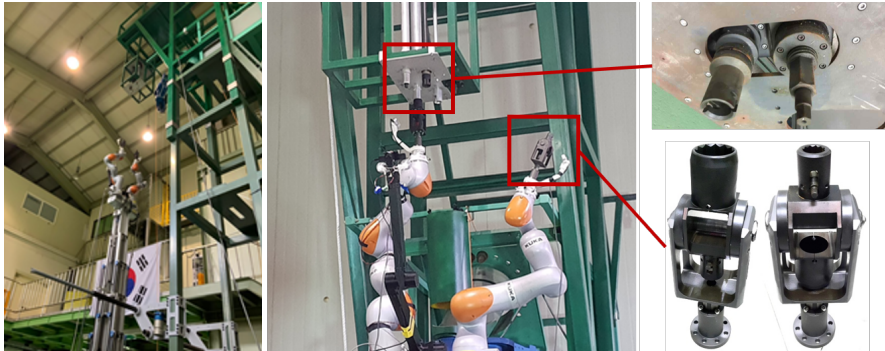
and Fig. 2.8-(c),(d). Considering the decomposed dynamics in (2.13), our proposed control framework eliminates coupling terms between decomposed dynamics such that two control objectives can be achieved simultaneously. On the other hand, (2.27) doesn't consider the property of (2.13) and coupling terms degrade the tracking and the vibration suppression performance.

## 2.5 Experiment

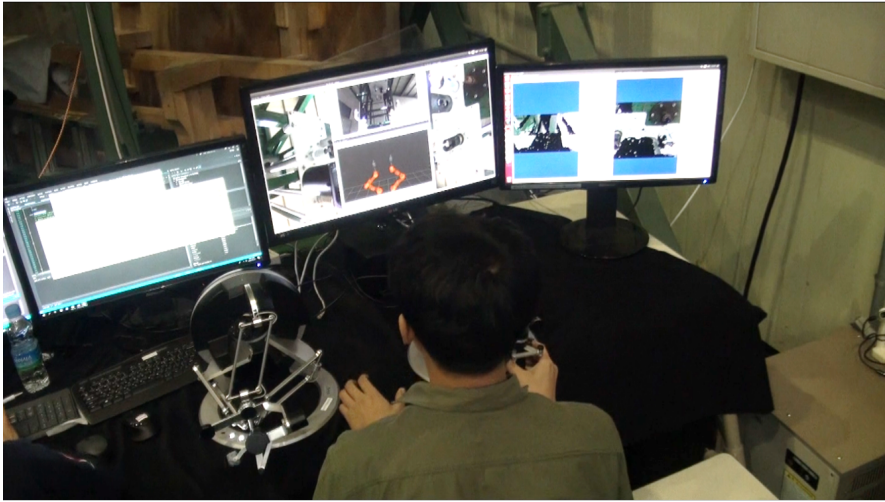
### 2.5.1 Experimental Setup

For the experimental validation of the vibration suppression control framework, we utilize the dual-arm telerobotic system in Fig. 2.2. The system consists of two 7-DoF KUKA-LBR-iiwa R820 manipulators controlled with 500Hz, a 2-DOF stage system with 300Hz control rate, and a 12-DoF telescopic mast with a fixed mobile base. The system is required to perform desired operations at the mock-up environment of the CANDU reactor which is described in Fig. 2.9-(a). The mock-up environment consists of a manual driving mechanism for the fuel bundle realizing task, and the mechanism is equipped at about a 10m height environment for the height operation. For the operation, the equivalent driving tools are equipped at the end-effector of each manipulator. The dual-arm manipulator system is required to follow the user command with the teleoperation setup in Fig. 2.9-(b). The user utilizes two haptic devices (Force Dimension Omega.7) for the control of each manipulator.

Our experimental validation consists of three scenarios. The first scenario is to check the vibration suppression performance under external disturbance.



(a)



(b)

FIGURE 2.9: (a) Mock-up environment of the CANDU reactor for fuel bundle realizing task. The manual driving mechanism is equipped at about a 10m height environment, and the driving tools are equipped at the end-effector of each manipulator. (b) The teleoperation setup for the control of the dual-arm telerobotic system. The user utilizes 6-DoF haptic devices for manipulator control and gets some visual feedback of the mock-up environment from system-mounted cameras.

The external force excitation is performed by pushing the system in two orthogonal directions as shown in Fig. 2.10 and  $x_s$  is measured during the excitation to compare the result between the system motion with control adoption and the system motion without the control. The second scenario is to check

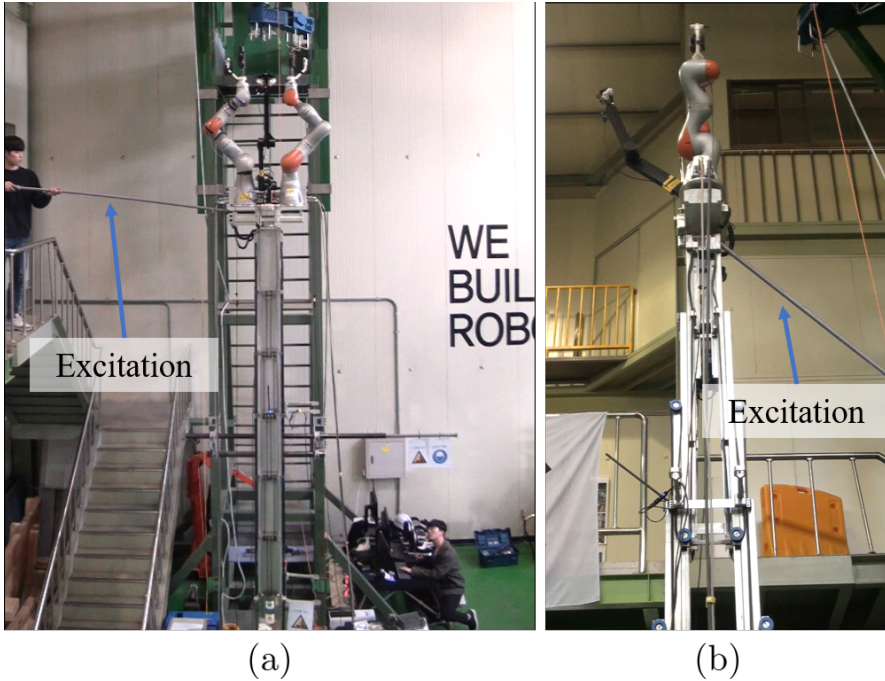


FIGURE 2.10: Snapshots of the first scenario to check the vibration suppression performance under external disturbance. Excitation is performed in two different directions to check the control performance.

the control performance during the manipulator motion. The dual-arm system is controlled to follow the user command in two orthogonal directions as shown in Fig. 2.11 and  $x_s$  is measured during the excitation to compare the result between the system motion with control adoption and the system motion without the control similar with the first scenario. The third scenario is to perform a practical application of the system in the mock-up environment, and the system is required to perform two precise operations: fuel bundle realizing task and tight-tolerance peg-in-hole task. For the fuel bundle realizing task, the right arm is first required to be tightened to the driving mechanism with the adoption of the vibration suppression control. After the right arm is tightened, the system can be considered a fixed base manipulator system

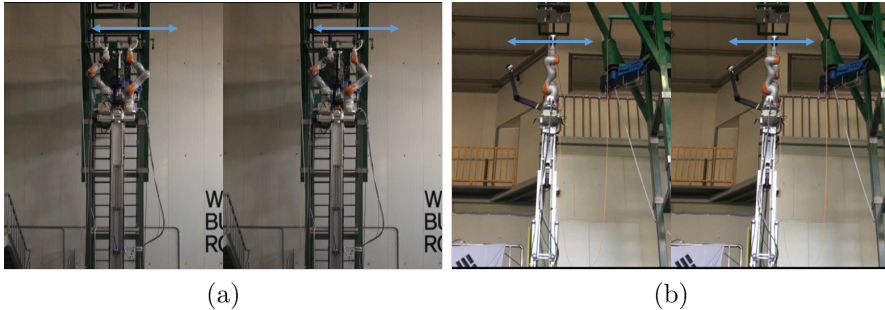


FIGURE 2.11: Snapshots of the second scenario to check the vibration suppression performance during the user command tracking. The system is required to follow the user command in two orthogonal directions to check the control performance.

and the remaining left arm follows the user command to tighten the other driving mechanism. As this fuel bundle realizing task is a tightening task to a vertically equipped mechanism, we perform an additional tight-tolerance peg-in-hole task to validate more general high-precision operation. The system performs a 1mm-tolerance peg-in-hole task with a hole setup equipped in a height environment with arbitrary pose.

## 2.5.2 Experimental Results

The result for the first scenario of vibration suppression under external disturbance is shown in Fig. 2.12. Plots in Fig. 2.12 represent the error of  $x_s$  during the external disturbance excitation, and we can see that the proposed control framework suppresses the vibration with a maximum 6mm level error (maximum 6.018mm in y-direction excitation, 6.619mm in z-direction excitation) of  $x_s$  under the external disturbance (RMS: 1.824mm in y-direction

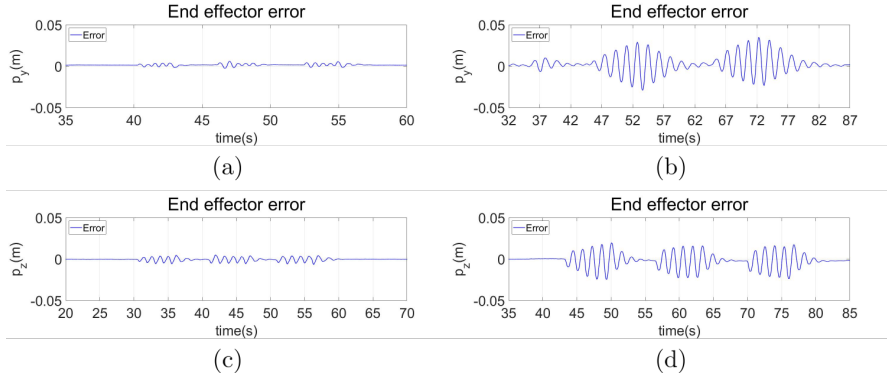


FIGURE 2.12: Error plots of the 2-DoF horizontal position of the mast-stage system  $x_s$  for the external disturbance excitation scenario. Plots in (a), (c) show the error when the vibration suppression control is adopted, and plots in (b), (d) show the error without the adoption of the vibration suppression control.

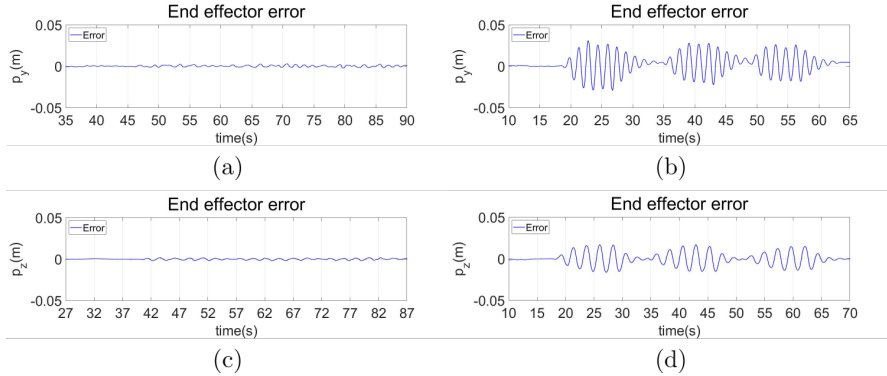


FIGURE 2.13: Error plots of the 2-DoF horizontal position of the mast-stage system  $x_s$  for the user command tracking scenario. Plots in (a), (c) show the error when the vibration suppression control is adopted, and plots in (b), (d) show the error without the adoption of the vibration suppression control.

motion, 1.923mm in z-direction motion), and without the vibration suppression control, the vibration is stabilized only by the damping of the mast (RMS: 12.231mm in y-direction motion, 8.859mm in z-direction motion).

The error plot of  $x_s$  for the second scenario of user command tracking is shown in Fig. 2.13. With the adoption of the vibration suppression control,

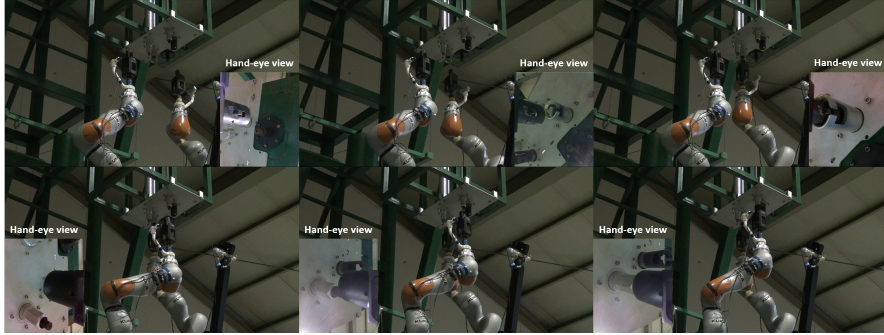


FIGURE 2.14: Snapshots of the 1mm-gap peg-in-hole task with the telerobotic system in mock-up environment of the nuclear power plant.



FIGURE 2.15: Snapshots of the 1mm-tolerance peg-in-hole task with the telerobotic system in mock-up environment of the nuclear power plant.

we ensure 1mm-scale tracking error (RMS: 1.012mm in y-direction motion, 0.799mm in z-direction motion) performance, reducing about 10 times smaller than the case controller not used (RMS: 11.828mm in y-direction motion, 7.397mm in z-direction motion).

Results for the third scenario are shown in Fig. 2.14 and Fig. 2.15. We can see that the system can perform high-precision tasks in the height environment with the proposed control framework.

## 2.6 Conclusion

In this chapter, we propose a passivity-based control framework for the dual-arm telerobotic system on the flexible mast. To resolve the vibration of the mast and the under-actuation of the system during high-precision operation in a height environment, we propose a control framework based on a dynamics decomposition approach to simultaneously achieve two different control objectives. With the adoption of passive decomposition, we can decompose the system into two independent subsystems preserving the system passivity, and design two control inputs separately. Experimental validations in a mock-up environment of the nuclear power plant show the effect of the proposed control framework.

# Chapter 3

## Optimal Wrench Control utilizing Supporting Surface

### 3.1 Introduction

In this chapter, we consider the wrench control problem for high-force operation in the height environment. While Chapter 2 covers the control problem for high-precise motion, the actual application of this dual-arm system on the long-reach supporting platform requires maintenance and repair tasks, which involve interaction force with the task environment (e.g., releasing the magazine, precision cutting, and pushing-insertion of wire into connectors, pushing or pulling of infrastructure equipment, and industrial tool manipulation such as drilling and hammering). For that, the system should execute sufficient interaction wrench to the target environment but the deformation issue arises due to the flexibility of the supporting platform. As the supporting platform reaches a higher altitude by unfolding telescopic structure, this deformation issue becomes more concern for the high-force interaction.

To resolve this deformation problem, we consider the problem of how to achieve high-force/high-precision in-height robot operation on an extending platform with substantial end-flexibility in this chapter. For this, we specifically consider the set-up of a dual-arm robot system on the flexible base as described in Fig. 3.1 with a supporting-providing surface. Compared with the setup in Chapter 2, we can see that the supporting surface is given to the dual-arm system. We utilize this supporting surface inspired by the human nature of exploiting the environment during high-force interaction tasks. By leaning or pushing the nearby environment with an arm or torso, the human can execute the higher interaction wrench while maintaining balancing stability. Similar to this exploitation of the supporting contact/surface by humans in daily life, we aim to attain high-force/high-precision operation by one (right/working/interaction) arm while holding, or pushing on, the surface by the other (left/supporting/contact) arm. We also specify the target task as to generate any wrench in a desired task wrench set at the right arm against the task environment, while holding the surface or maintaining the bilateral/holding or unilateral/frictional contact on the supporting surface by the left arm. The desired task wrench set is defined by the form of wrench polytope denoted by  $\mathcal{W}_e^d$  (see the definition in Sec. 3.2.2). Recruiting the left arm to utilize the supporting contact is crucial, since, without that, it would be difficult to precisely regulate the high-interaction wrench by the right arm, as the (often lightly-damped) flexible base may produce oscillation or even its deformation may be too large to hold against the high-interaction wrench at the right arm. Moreover, the system we consider is under-actuated: only the two robot arms are fully-actuated, while the flexible base lacks any control actuation such that

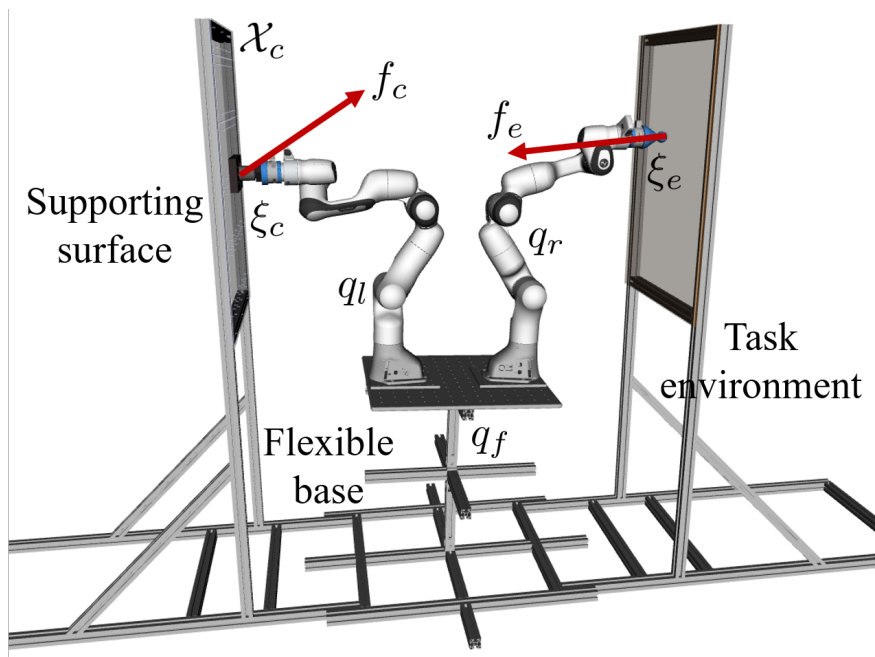


FIGURE 3.1: The interaction task of the dual-arm robotic system on the flexible base utilizing supporting contact. The system performs interaction tasks with one arm while maintaining supporting contact with the other arm.

without the supporting contact, we cannot directly control the system. The supporting contact wrench can be considered as an additional control input and this wrench can be utilized to prevent the deformation and task wrench execution.

To solve this control problem for high-force in-height operation utilizing the supporting contact, we first design our control (control actuation of the dual-arm system) to be composed of the nominal control  $\tau_a^*$  (to produce centroid of  $\mathcal{W}_e^d$ ), the active stiffness control  $\tau_a^k$  with the stiffness gain  $K_a$ , and the real-time feedback wrench control  $\tau_a'$  to improve precision and robustness of the interaction wrench control at the right hand. More precisely, we first optimize the normal configuration  $q^*$  of the total system (i.e., two robot arms and the flexible base), the nominal control actuation  $\tau_a^*$  of the two arms and the nominal supporting contact wrench  $f_c^*$  at the left arm to produce the representative/nominal task wrench  $f_e^*$  (i.e., the centroid of  $\mathcal{W}_e^d$ ) at the right arm, while minimizing the nominal control  $\tau_a^*$  and also ensuring the stability of the interaction operation by alleviating the possibly-destabilizing effect of geometric stiffness [74], all under the supporting surface holding/frictional-contact constraints and the limits of the joint angles and control actuation constraints. This optimization is then followed by the second optimization to choose the active stiffness gain  $K_a$  for  $\tau_a^k$ , under the constraints that the overall stiffness of the system (i.e., combination of flexible base stiffness  $K_f$ , active stiffness gain  $K_a$ , and geometric stiffness  $\bar{K}_{geo}$ ) to be positive-definite (for system stability) and the desired wrench polytope  $\mathcal{W}_e^d$  to be compatible with the constraints of the joint torque limits and the supporting contact maintenance

(e.g., friction-cone constraint). Finally, the feedback wrench control  $\tau'_a$  is designed based on the stiffness relation at the right arm end-effector with the effect of  $\tau'_a$  fully analyzed.

The key theoretical result to allow us to attain these is the novel stiffness analysis of the dual-arm robot on the flexible base. More precisely, through some variational analysis under the supporting contact maintenance constraint<sup>1</sup>, we could extract a peculiar stiffness relation linear among  $\delta f_c, \delta f_e, \delta \tau_a$  (i.e., deviations of  $f_c, f_e, \tau_a$  around the nominal configuration and wrenches  $q^*, f_e^*, f_c^*, \tau_a^*$ ). This relation is particularly crucial for our second optimization process, as it allows us to explicitly compute the effect of the supporting-contact wrench constraints (i.e.,  $\mathcal{W}_e^c$ ) and the control actuation limits (i.e.,  $\mathcal{W}_e^r$ ) at the right arm wrench space so that we can efficiently check if the desired wrench polytope  $\mathcal{W}_e^d$  at the right arm is feasible with those constraints/limits. Using this linear relation, we can also eliminate a substantive number of search variables, thereby, significantly improving the computational efficiency and convergence of the optimization solving. This relation also enables us to extract the stiffness equation at the right arm wrench space, thereby, greatly facilitating our design of the feedback wrench control  $\tau'_a$ .

The main contribution of this chapter can be summarized as follows:

- A novel control framework design consists of nominal control, compliance control, and feedback wrench control to perform high-force operation utilizing supporting contact.

---

<sup>1</sup>This holding/contact-maintenance constraint is ensured by explicitly incorporating its relevant constraints into our optimization formulation with some safety-margin at the supporting-contact polytopes to address the effect of  $\tau'_a$

- A novel sequential optimization framework to optimize the nominal control (together with nominal configuration and nominal contact wrench) and active stiffness control gain.
- Novel quasi-static stiffness analysis under supporting contact to find the linear relation among control actuation, task wrench, and contact wrench to improve the computational efficiency of the optimization and enable feedback wrench control design.
- Experimental validation to show the efficacy of the proposed control framework for high-force operation.

The rest of the chapter is organized as follows: Sec. 3.2 shows problem formulation for our control framework. Quasi-static stiffness analysis and a linear relation among  $(\delta f_c, \delta f_e, \delta \tau_a)$  in Sec. 3.3. Based on this linear relation, Sec. 3.4 provides stiffness behavior at the interaction task space and the feedback wrench control. Sec. 3.5 provides details of a nominal configuration and active stiffness optimization. Sec. 3.6 shows the simulational results with the necessity validation of the supporting contact. Sec. 3.7 presents experimental results to validate our control framework, and the conclusion of this paper is shown in Sec. 3.8.

## 3.2 Problem Formulation

### 3.2.1 System Modeling

Let us first consider the dual-arm manipulator system mounted on the flexible base performing interaction tasks while utilizing supporting contact as shown in Fig. 3.1. Then, the system dynamics can be expressed by

$$\begin{aligned} M(q)\ddot{q} + C(q, \dot{q})\dot{q} + G(q) + \mathcal{S}_f\tau_f \\ = \mathcal{S}_a\tau_a - J_c^T(q)f_c + J_e^T(q)f_e \end{aligned} \quad (3.1)$$

where  $q = [q_f; q_a] \in \mathbb{R}^n$  is the system configuration with  $q_f \in \mathbb{R}^{n_f}$  and  $q_a = [q_l; q_r] \in \mathbb{R}^{n_a}$  respectively being the configurations of the flexible base and that of the actuated joints of the dual-arm manipulator;  $M(q)$ ,  $C(q, \dot{q}) \in \mathbb{R}^{n \times n}$ , and  $G(q) \in \mathbb{R}^n$  are the inertia, Coriolis, and gravity matrices of the system;  $\tau_f$  is the compliance of the (un-actuated) flexible base as given by

$$\tau_f = B_f(q_f)\dot{q}_f + K_f(q_f)[q_f - q_f^0]$$

where  $B_f(q_f) \in \mathbb{R}^{n_f \times n_f}$  and  $K_f(q_f) \in \mathbb{R}^{n_f \times n_f}$  are the damping and stiffness matrices with  $q_f^0 \in \mathbb{R}^{n_f}$  being an equilibrium configuration; and  $\tau_a \in \mathbb{R}^{n_a}$  is the control actuation for the (fully-actuated) dual-arm manipulator, which is to be designed below. Without loss of generality, in this chapter, as shown in Fig. 3.1, we assume that the right arm is performing the high-force/precision interaction tasks against a target task environment (or object), while the left arm is holding, or maintaining the contact on, the supporting surface  $\mathcal{X}_c$ . Their

respective poses and task/contact wrenches are then given by  $\xi_e(q) \in \mathbb{R}^{n_e}$ ,  $\xi_c(q) \in \mathbb{R}^{n_c}$  and  $f_e \in \mathbb{R}^{n_e}$  and  $f_c \in \mathbb{R}^{n_c}$ , with  $\dot{\xi}_e(q) = J_e(q)\dot{q}$  and  $\dot{\xi}_c(q) = J_c(q)\dot{q}$ , where  $J_e(q) \in \mathbb{R}^{n_e \times n_e}$  and  $J_c(q) \in \mathbb{R}^{n_c \times n_e}$  are the end-effector and supporting-contact Jacobian matrices of the right and left arms. The matrices  $\mathcal{S}_f \in \mathbb{R}^{n \times n_f}$  and  $\mathcal{S}_a \in \mathbb{R}^{n \times n_a}$  are the selection matrices as defined by

$$\mathcal{S}_f = \begin{bmatrix} I_{n_f} \\ 0_{n_a \times n_f} \end{bmatrix} \in \mathbb{R}^{n \times n_f}, \quad \mathcal{S}_a = \begin{bmatrix} 0_{n_f \times n_a} \\ I_{n_a} \end{bmatrix} \in \mathbb{R}^{n \times n_a} \quad (3.2)$$

In this section, for simplicity, we assume constant compliance parameters  $B_f$  and  $K_f$  with the zero equilibrium configuration  $q_f^0 = 0$  and this can be easily extended for variable compliance and non-zero equilibrium of the flexible base. We also assume that, as typically true for high-force/high-precision tasks, the system motion is slow enough so that the system dynamics (3.1) can be suitably captured by the following quasi-static equation:

$$G(q) + \mathcal{S}_f K_f q_f = \mathcal{S}_a \tau_a - J_c^T(q) f_c + J_e^T(q) f_e \quad (3.3)$$

Here, note that this equation (3.3) is under-actuated (i.e., fully-actuated dual-arm with un-actuated flexible base with  $n = n_a + n_f$ ). Further, the actuation  $\tau_a \in \mathbb{R}^{n_a}$  is not in the same space with the interaction force  $f_e \in \mathbb{R}^{n_e}$  or the contact force  $f_c$ , thus, how to affect the interaction and contact forces via the control  $\tau_a$  is not straightforward.

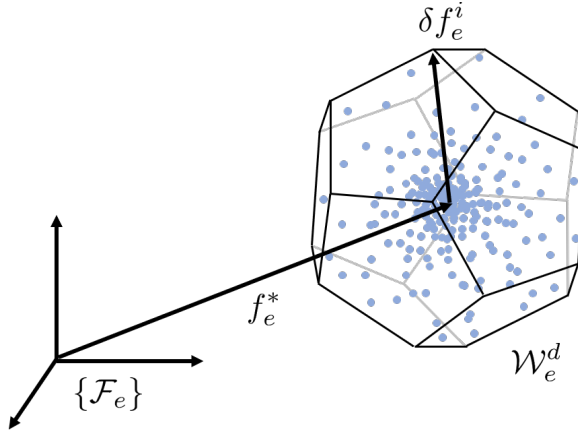


FIGURE 3.2: The set of target task wrench data can be reformulated to the form of a desired wrench polytope  $\mathcal{W}_e^d$  with its center  $f_e^*$  and apexes  $\delta f_e^i$

### 3.2.2 Control Objectives

In this paper, we aim to achieve the following control objectives at the same time:

- The right arm end-effector can exert *any* desired wrench against the environment in the task wrench polytope as defined by

$$\mathcal{W}_e^d = \{f_e \in \mathbb{R}^{n_e} \mid f_e = f_e^* + \sum_{i=1}^{n_p} \alpha_i \delta f_e^i, \alpha_i \geq 0, \sum_{i=1}^{n_p} \alpha_i \leq 1\} \quad (3.4)$$

while maintaining the desired pose  $\xi_e(q) = \xi_e^d$  (see Fig. 3.2), where  $f_e^*$  is the nominal task wrench around the nominal configuration  $q^* \in \mathbb{R}^n$  (to be defined below), which is also the centroid of  $\mathcal{W}_e^d$  with the apexes  $\delta f_e^i$ ;

- During this operation, the left arm end-effector should hold, or maintain contact with, the supporting surface  $\mathcal{X}_c$  with  $\xi_c(q) \in \mathcal{X}_c \forall t \geq 0$ , while

contact wrench  $f_c$  constrained to be in the set of

$$\mathcal{W}_c := \{f_c \in \mathbb{R}^{n_c} \mid \|f_c\|_\infty \leq \alpha\} \quad (3.5)$$

for the case of bilateral holding (e.g., rigidly grip a bar, fixed to the surface via bolting) with bounded contact force; or in the set of

$$\mathcal{W}_c := \{f_c \in \mathbb{R}^{n_c} \mid f_c^t \leq \mu f_c^n, f_c^n \geq 0\} \quad (3.6)$$

for the case of unilateral/friction-cone contact, where  $f_c^n = (f_c \cdot n_c)n_c$  and  $f_c^t = f_c - f_c^n$  are normal and tangential contact forces for the contact surface normal  $n_c$ , and  $\mu$  is the friction coefficient; and

- We aim to achieve the objectives above, while also ensuring the stability of (3.3) against perturbation around the normal configuration  $q^*$  (to be defined below), respecting the joint angle and torque limits s.t.,

$$\underline{q} < q^* < \bar{q} \quad (3.7)$$

$$\underline{\tau}_a \leq \tau_a^* \leq \bar{\tau}_a \quad (3.8)$$

and utilizing the passive stiffness  $K_f$  of the flexible base as much as possible.

For these above control objectives, we assume that the target task information is given by the desired task pose  $\xi_e^d \in \mathbb{R}^{n_e}$ , supporting surface  $\mathcal{X}_c$ . The desired task wrench is given by (3.4), which is formulated from the set of task wrench data defined by  $\mathcal{F}_e := \{f_e^1, f_e^2, \dots, f_e^i, \dots, f_e^N\}$  with  $f_e^i \in \mathbb{R}^{n_e}$ . The nominal task wrench  $f_e^*$  is determined by the weighted average of  $f_e^i$ , and  $\delta f_e^i$

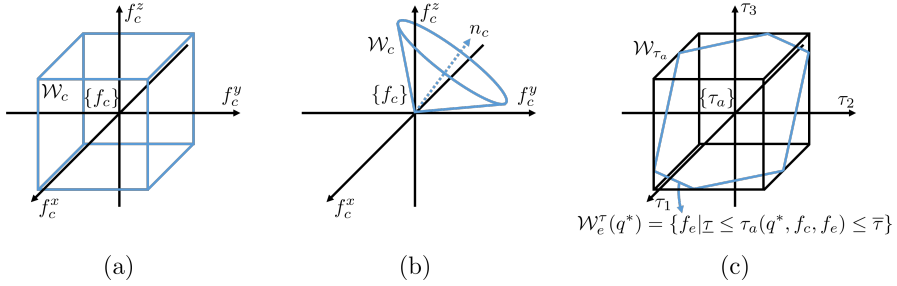


FIGURE 3.3: (a) 3D example of contact wrench set  $\mathcal{W}_c$  for the bilateral holding constraint (e.g., hard grasping contact). (b) Contact wrench set  $\mathcal{W}_c$  for the unilateral point constraint which is a friction cone with contact normal  $n_c$ . (c)  $\mathcal{W}_e^\tau(q^*)$  formulation from  $\mathcal{W}_{\tau_a}$ .

represents extremum variances wrench from  $f_e^*$ . During the task operation, the system has to maintain the supporting contact with  $\mathcal{X}_c$ , and for that, the system should regulate the feasible contact wrench during the task. The set of feasible contact wrenches is presented in (3.5)-(3.6) which are also called contact wrench cone (CWC) [57–60]. The 3D example of these contact wrench polytopes is shown in Fig. 3.3-(a),(b). Also, the joint torque should be regulated in torque limit during the execution of  $f_e^d \in \mathcal{W}_e^d$ . This can be checked by adopting the concept of actuation wrench polytope (AWP) [61, 62]. By finding the intersection between a hypercube  $\mathcal{W}_{\tau_a} := \{\tau_a \in \mathbb{R}^{n_a} | \underline{\tau}_a \leq \tau_a \leq \bar{\tau}_a\}$  and  $J_e^T(q)$ , we can find feasible task wrench set considering joint torque limit defined by  $\mathcal{W}_e^\tau$ , which will be presented in Sec. 3.3.2. The 3D example of  $\mathcal{W}_e^\tau$  is shown in Fig. 3.3-(c).

To achieve these control objectives, we design the control actuation  $\tau_a$  s.t.,

$$\tau_a = \tau_a^* + \tau_a^k + \tau_a^l \quad (3.9)$$

with each term explained as follows:

- The first term  $\tau_a^*$  is the nominal control to generate the nominal task wrench  $f_e^* \in \mathcal{W}_e^d$  and the nominal contact wrench  $f_c^* \in \mathcal{W}_c$  at the nominal equilibrium configuration  $q^*$  with

$$G(q^*) + \mathcal{S}_f K_f q_f^* = \mathcal{S}_a \tau_a^* - J_c^T(q^*) f_c^* + J_e^T(q^*) f_e^* \quad (3.10)$$

where  $q^* = [q_a^*; q_f^*] \in \mathfrak{R}^n$  will be computed via the optimization process in Sec. 3.5 to satisfy the control objectives as stated above;

- The second term is given by

$$\tau_a^k := -B_a \dot{q}_a - K_a (q_a - q_a^*) \quad (3.11)$$

which is the active compliance control to stabilize the system (3.3) and enhance the robustness around the equilibrium  $q^*$ , where  $B_a, K_a \in \mathbb{R}^{n_a \times n_a}$  are the damping and stiffness gains. Only the stiffness gain  $K_a$  we will consider here, and will be chosen via the optimization procedure in Sec. 3.5.2 while ensuring the system stability and the task and supporting-contact wrench requirements (i.e.,  $f_e \in \mathcal{W}_e^d$  and  $f_c \in \mathcal{W}_c$ ), for which the peculiar linear relation among  $\delta f_c, \delta f_e, \delta \tau_a$  (i.e., deviations of  $f_c, f_e, \tau_a$  around  $q^*, f_e^*, f_e^*, \tau_a^*$ ) to be obtained in Sec. 3.3.2 under the supporting-contact maintenance turns out to greatly facilitate the optimization formulation and solving of Sec. 3.5.2; and

- The last term  $\tau_a'$  is to contain the PI (proportional-integral) type control with the feedback of the task wrench  $f_e$  to precisely track the desired wrench  $f_e^d \in \mathcal{W}_e^d$  while enhancing the control robustness in general via the feedback action.

### 3.2.3 Proposed Framework

Based on control objectives in Sec. 3.2.2 and the equivalent control structure in (3.9), our control framework consists of the following novel algorithms:

- Nominal configuration and active compliance optimization: offline optimization procedure to find optimal nominal configuration  $q^*$  (together with  $\tau_a^*$  and  $f_c^*$ ) and active control compliance gain  $K_a^*$ . As the control actuation  $\tau_a$  in (3.9) split the control into  $\tau_a^*$  for nominal configuration with  $f_e^*$  and  $\tau_a^k + \tau_a'$  for perturbed motion with  $\delta f_e$ , we present two sub-problems of optimization framework. First, the nominal configuration  $q^*$  is optimized together with  $\tau_a^*$  and  $f_c^*$  to execute  $f_e^*$  with minimum load. The contact pose  $\xi_c \in \mathbb{R}^{n_c}$  is determined by the optimized solution of  $q^*$ . After the calculation of the nominal configuration and its equivalent wrenches, we now optimize the active stiffness gain for the perturbed behavior of the system. We check whether  $\mathcal{W}_e^d$  is compatible with joint torque limit and contact wrench constraints. The proposed optimization framework will be shown in Sec. 3.5.
- Quasi-static stiffness analysis: Considering the perturbed motion near the nominal configuration, we can obtain the quasi-static stiffness behavior of the system. We can obtain a peculiar linear relation among  $\delta f_e$ ,  $\delta f_c$ , and  $\delta \tau_a$  based on this stiffness behavior combined with the supporting contact constraint. This linear relation enables the enhancement of calculation efficiency for the active stiffness optimization, and further we can obtain the stiffness behavior in the right-arm end-effector which

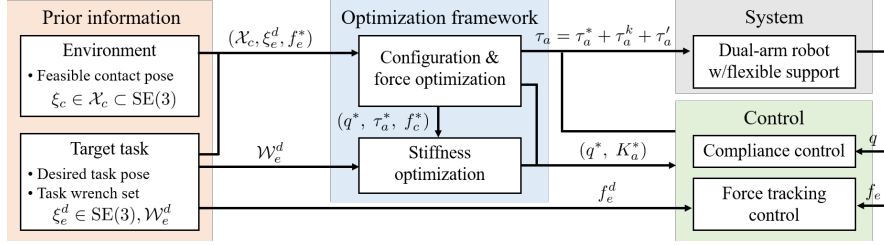


FIGURE 3.4: The architecture of the proposed control framework.

enables the design of real-time feedback wrench control  $\tau_a^l$  which will be shown in Sec. 3.4.

The overall architecture of the proposed control framework is described in Fig. 3.4.

### 3.3 Stiffness Analysis and Polytope Mappings

In this section, by perturbing (3.3), we analyze the stiffness of the system (3.3) around the nominal equilibrium  $(q^*, f_e^*, f_c^*)$  of (3.10). The perturbation analysis provides a linear relation among the deviations  $\delta q, \delta f_e, \delta f_c$  and  $\delta \tau_a := \tau_a^k + \tau_a^l$ , respectively from  $q^*, f_e^*, f_c^*$  and  $\tau_a^*$ . This linear relation, combined with the contact-maintaining/surface-holding constraint  $\xi_c(q) \in \mathcal{X}_c$ , then allows us to map the contact wrench polytope  $\mathcal{W}_c$  in (3.5)-(3.6) and the torque limit polytope (3.8) into the space of the interaction wrench  $f_e$ , thereby, allowing us to check their effects on the attainment of exerting the desired wrench by the right-arm (i.e.,  $f_e^d \in \mathcal{W}_e^d$ ) in a straightforward manner (see the optimization of

$K_a$  in Sec. 3.5.2). This relation further reveals the stiffness relation at the right-arm end-effector (i.e., between  $\delta\xi_e$  and  $\delta f_e$ ), which turns out to be instrumental for our design of the feedback control  $\tau'_a$  (see Sec. 3.4).

### 3.3.1 Perturbation Analysis and Stiffness Matrices

By perturbing (3.10) around the nominal equilibrium  $(q^*, f_e^*, f_c^*)$  with the control equation (3.9) and (3.11), we have

$$\begin{aligned} G(q^* + \delta q) + J_c(q^* + \delta q)^T(f_c^* + \delta f_c) + \mathcal{S}_u K_f(q_f^* + \delta q_f) \\ = \mathcal{S}_a(\tau_a^* - K_a \delta q_a + \tau'_a) + J_e(q^* + \delta q)^T(f_e^* + \delta f_e) \end{aligned} \quad (3.12)$$

where  $\delta q, \delta f_e, \delta f_c$  are the deviations around the nominal state. Taking the first-order Taylor expansion and neglecting  $\delta q \delta f_e$  and  $\delta q \delta f_c$  terms, we can get

$$\begin{aligned} \left( G(q^*) + \frac{\partial G}{\partial q} \Big|_{q^*} \delta q \right) + \left( J_c^T(q^*) f_c^* + \frac{\partial J_c^T[f_c^* + \delta f_c]}{\partial q} \Big|_{q^*} \delta q \right) \\ + \mathcal{S}_f K_f(q_f^* + \delta q_f) = \mathcal{S}_a(\tau_a^* - K_a \delta q_a + \tau'_a) \\ + \left( J_e^T(q^*) f_e^* + \frac{\partial J_e^T[f_e^* + \delta f_e]}{\partial q} \Big|_{q^*} \delta q \right) \end{aligned} \quad (3.13)$$

From this, we can obtain a linear stiffness equation of the system around the equilibrium (3.10) s.t.,

$$\bar{K} \delta q + J_c^T(q^*) \delta f_c = J_e^T(q^*) \delta f_e + \mathcal{S}_a \tau'_a \quad (3.14)$$

with  $\bar{K} \in \mathbb{R}^{n \times n}$  being the effective stiffness of the system (3.3) as given by

$$\bar{K} := \bar{K}_f + \bar{K}_a + \bar{K}_{geo} \quad (3.15)$$

where  $\bar{K}_f = \mathcal{S}_f K_f \mathcal{S}_f^T$  is the passive stiffness (from the flexible base),  $\bar{K}_a = \mathcal{S}_a K_a \mathcal{S}_a^T$  is the active stiffness (from  $K_a$  of (3.11)), and

$$\bar{K}_{geo} := \left[ \frac{\partial G(q)}{\partial q} \Big|_{q^*} + \frac{\partial J_c^T(q) f_c^*}{\partial q} \Big|_{q^*} - \frac{\partial J_e^T(q) f_e^*}{\partial q} \Big|_{q^*} \right] \quad (3.16)$$

is the geometric stiffness [74]. This geometric stiffness comes from the change in the system geometry (configuration), and the effect of this stiffness depends on the system configuration and the equilibrium wrench. The geometric stiffness  $\bar{K}_{geo}(q^*)$  is not necessarily positive-definite and, thus, can induce system instability. To resolve this issue, we may control  $q^*$  and  $f_c^*$  to enforce positive-definite  $\bar{K}_{geo}(q^*)$ , as  $\bar{K}_{geo}(q^*)$  is a function of them. However,  $\bar{K}_{geo}^g(q^*) := \frac{\partial G}{\partial q} \Big|_{q^*}$  and  $\bar{K}_{geo}^e(q^*) := -\frac{\partial J_e^T f_e^*}{\partial q} \Big|_{q^*}$  which are geometric stiffness related to the gravity and the task wrench, solely depend on the change of  $q^*$  while the geometric stiffness  $\bar{K}_{geo}^c(q^*) := \frac{\partial J_c^T f_c^*}{\partial q} \Big|_{q^*}$  can be controlled by  $q^*$  and  $f_c^*$ . Due to the limited range of  $q^*$ , the range of  $\bar{K}_{geo}^g(q^*)$  and  $\bar{K}_{geo}^e(q^*)$  that change by  $q^*$  is small such that we found that this strategy of  $q^*$  and  $f_c^*$  control is too limiting. For this, in the optimization process of Sec. 3.5.1, we aim to minimize the effect of this possibly-destabilizing  $\bar{K}_{geo}$  by optimizing  $q^*$  and  $f_c^*$ , so that it can be dominated by the positive-definite (i.e., always stabilizing)  $\bar{K}_f$  and  $\bar{K}_a$ , which would be granted in practice with a reasonably-designed flexible base (i.e., not so soft with large enough  $K_f$ ) and a reasonably-strong dual robotic arms (i.e., large enough  $K_a$  possible for (3.11)), as also evidenced in Sec. 3.7.

Note also that, although not included in the analysis here, the damping gain  $B_a$  of (3.11) always helps the system stability.

### 3.3.2 Polytope Mappings under $\xi_c(q) \in \mathcal{X}_c$

Now, given  $(f_e^*, f_c^*, \tau_a^*)$  from (3.10), if we can analyze the behavior of the deviations  $(\delta f_e, \delta f_c, \delta \tau_a)$ , we would be able to see if the interaction task is attained (i.e.,  $f_e^d = f_e^* + \delta f_e$ ) and the supporting-contact constraint (i.e.,  $f_c = f_c^* + \delta f_c \in \mathcal{W}_c$  with (3.5)-(3.6)) or the joint torque limit constraint (i.e.,  $\tau_a = \tau_a^* + \delta \tau_a = \tau_a^* + \tau_a^k + \tau_a^l$  with (3.8)) is violated. Also, since what we ultimately want is to achieve the interaction task at the right arm, it would be useful and convenient to map the supporting-contact constraint  $\mathcal{W}_c$  and the joint torque limit constraint (3.8) into the task wrench space of  $f_e$ , and see how those constraints will curb the possible wrench-generation polytope at the right arm.

For this, here, we utilize the constraint that  $\xi_c(q) = \mathcal{X}_c$ , which is granted *at default* if the left arm is rigidly holding the supporting surface with (3.5) or will (and needs to) be enforced by the optimization processes in Sec. 3.5 if the left-arm is to maintain the frictional contact on the surface with (3.6). Then, the penetration into the supporting-surface  $\mathcal{X}_c$  should be zero, or we should have:

$$\begin{aligned} \delta \xi_c &= J_c(q^*) \delta q \\ &= J_c(q^*) \bar{K}^{-1} [-J_c^T(q^*) \delta f_c + J_e^T(q^*) \delta f_e + \mathcal{S}_a \tau_a^l] \equiv 0 \end{aligned} \quad (3.17)$$

where we use (3.14). From this, we can obtain

$$\delta f_c = J_c^{\bar{K}+T}(q^*)[J_e^T(q^*)\delta f_e + \mathcal{S}_a\tau_a'] \quad (3.18)$$

where  $J_c^{\bar{K}+}(q^*) = \bar{K}^{-1}J_c^T(q^*)[J_c(q^*)\bar{K}^{-1}J_c^T(q^*)]^{-1} \in \mathbb{R}^{n \times n_c}$  is the weighted pseudo inverse of  $J_c(q^*)$  w.r.t. the effective stiffness  $\bar{K}$ . Injecting (3.18) into (3.14), we then have

$$\bar{K}\delta q = N_c(q^*)[J_e^T(q^*)\delta f_e + \mathcal{S}_a\tau_a'] \quad (3.19)$$

where the term  $J_e^T(q^*)\delta f_e$  is projected to the space, which cannot be supported by  $J_c^T(q^*)$  with the associated null-space operator  $N_c(q^*) \in \mathbb{R}^{n \times n}$  w.r.t. the effective stiffness  $\bar{K}$  given by

$$N_c(q^*) = I - J_c^T(q^*)J_c^{\bar{K}+T}(q^*)$$

Using (3.19) in (3.9), we can express the control (3.9) as a function of  $\delta f_e$  s.t.,

$$\begin{aligned} \tau_a &= \tau_a^* - K_a\delta q_a + \tau_a' = \tau_a^* - K_a\mathcal{S}_a^T\delta q + \tau_a' \\ &= \tau_a^* - K_a\mathcal{S}_a^T\bar{K}^{-1}N_c(q^*)[J_e^T(q^*)\delta f_e + \mathcal{S}_a\tau_a'] + \tau_a' \end{aligned} \quad (3.20)$$

This relation (3.20) then allows us to map the joint torque limit constraint (3.8) into the following  $\tau$ -polytope in the task wrench space of the right arm:

$$\mathcal{W}_e^\tau := \{f_e \in \mathbb{R}^{n_e} | \mathcal{I}_a \leq A_\tau + B_\tau\delta f_e + C_\tau\tau_a' \leq \bar{\tau}_a\} \quad (3.21)$$

where  $f_e = f_e^* + \delta f_e$  with  $f_e^*$  given,  $A_\tau := \tau_a^*$ ,  $B_\tau := -K_a \mathcal{S}_a^T \bar{K}^{-1} N_c(q^*) J_e^T(q^*)$ , and  $C_\tau := I - K_a \mathcal{S}_a^T \bar{K}^{-1} N_c(q^*) \mathcal{S}_a$ . This mapping from (3.8) to the polytope  $\mathcal{W}_e^\tau$  is possible due to the linear relation between  $\tau_a$  and  $\delta f_e$  in (3.20). Note also the presence of  $\tau_a'$ , which is a feedback control, thus, cannot be known *a priori*. This term  $\tau_a'$ , yet, can be approximated by the linear function of  $\delta f_e$  with the additional bounded uncertainty term in practice. Let us denote this uncertainty bound term through the operator  $C_\tau$  by  $\mathcal{B}_{\epsilon_1}$ . We choose this  $\mathcal{B}_{\epsilon_1}$  to be constant (e.g., independent from  $K_a$ ). This can be possible if we compute its conservative estimate with the various bounds taken into account. A necessary condition for the control objective of exerting any  $f_e \in \mathcal{W}_e^d$  by the right arm is then given by

$$\mathcal{W}_e^d \oplus \mathcal{B}_{\epsilon_1} \subset \mathcal{W}_e^\tau \quad (3.22)$$

where  $\oplus$  is the Minkowski sum operator. See Sec. 3.4 for more details on the boundedness of  $\tau_a'$ .

On the other hand, similarly to (3.21), using (3.18), we can express the supporting-contact wrench in the task wrench space of the right arm s.t.,

$$f_c = f_c^* + J_c^{\bar{K}+T} [J_e^T(q^*) \delta f_e + \mathcal{S}_a \tau_a'] \quad (3.23)$$

where the contact wrench  $f_c$  should be in the set of  $\mathcal{W}_c$  as given in (3.5) or (3.6). This condition can be expressed by

$$\mathcal{W}_e^c := \{f_e \in \mathbb{R}^{n_e} \mid A_c + B_c \delta f_e + C_c \tau_a' \in \mathcal{W}_c\} \quad (3.24)$$

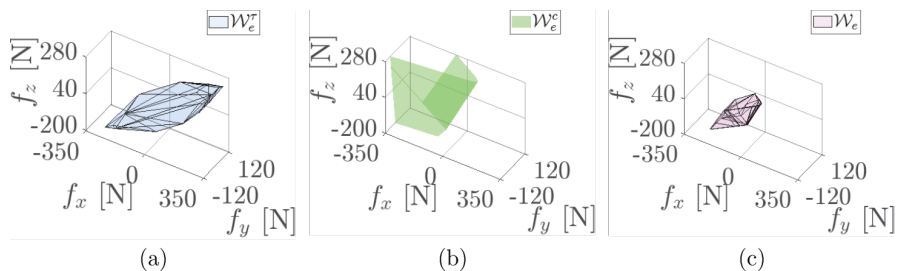


FIGURE 3.5: Example of the polytope mappings under the supporting contact constraint: (a)  $\mathcal{W}_e^\tau$  formulation. (b)  $\mathcal{W}_e^c$  formulation. (c)  $\mathcal{W}_e := \mathcal{W}_e^\tau \cap \mathcal{W}_e^c$  formulation.

where  $f_e = f_e^* + \delta f_e$ ,  $A_c := f_c^*$ ,  $B_c := J_c^{\bar{K}+T} J_e^T(q^*)$ , and  $C_c := J_c^{\bar{K}+T} \mathcal{S}_a$ . This then leads into a polytope in the task wrench space of  $f_e$  for the case of (3.5) or a cone for the case of (3.6). A necessary condition for the right arm to exert any wrench  $f_e$  in the set of  $\mathcal{W}_e^d$  can then be written by

$$\mathcal{W}_e^d \oplus \mathcal{B}_{\epsilon_2} \subset \mathcal{W}_e^c \quad (3.25)$$

where  $\epsilon_2$  denotes a bound additional uncertainty term of  $\tau_a'$  through  $C_c$ . Similarly for (3.22) above, here, we also assume this ball  $\mathcal{B}_{\epsilon_2}$  to be of a (conservatively-computed) constant radius. See also Sec. 3.4 for more details on the bounds of  $\tau_a'$ .

These two inclusion conditions in (3.22) and (3.25) should both be satisfied for the task feasibility, and we can define resultant wrench set  $\bar{\mathcal{W}}_e$  by

$$\mathcal{W}_e = \mathcal{W}_e^\tau \cap \mathcal{W}_e^c \quad (3.26)$$

The example of  $\mathcal{W}_e^\tau$ ,  $\mathcal{W}_e^c$  and  $\mathcal{W}_e$  is described in Fig. 3.5.

Here, note that the two inclusion conditions, (3.22) and (3.25), can be

checked simply by inserting each  $\delta f_e^i$  of (3.4) into (3.22) or (3.25) to see if any of them violates the condition of (3.22) or (3.25). This straightforward checking of the two conditions (3.22) and (3.25) is possible thanks to the stiffness analysis presented in this Sec. 3.3 and substantially facilitates the optimization solving to find  $K_a$  under these two inclusion conditions in Sec. 3.5.2. Our stiffness analysis presented here also allows us to obtain the stiffness behavior at the right arm end-effector and to design the real-time control  $\tau_a'$  in (3.9) based on that. This is explained in the following Sec. 3.4.

### 3.4 Design of Feedback Wrench Control

Using (3.19), we can derive the stiffness relation at the right-arm end-effector as follows:

$$\begin{aligned}\delta\xi_e &= J_e(q^*)\delta q \\ &= K_e^{-1}[\delta f_e + K_e(q^*)J_e(q^*)\bar{K}^{-1}N_c(q^*)\mathcal{S}_a\tau_a']\end{aligned}\quad (3.27)$$

where

$$K_e(q^*) := [J_e(q^*)\bar{K}^{-1}N_c(q^*)J_e^T(q^*)]^{-1} \in \mathbb{R}^{n_e \times n_e} \quad (3.28)$$

is the interaction task space stiffness matrix at the right arm. This stiffness matrix  $K_e(q^*)$  is not necessarily symmetric and positive-definite from that  $\bar{K}(q^*)$  in (3.15) is in general neither due to the presence of  $\bar{K}_{geo}(q^*)$ . It is not so problematic even if  $\bar{K}_e$  is not symmetric, yet, it is definitely so if  $\bar{K}_e$  is not positive-definite, as the system can then exhibit instability. This issue is

resolved in the optimization process in Sec. 3.5.2 , where we explicitly enforce the positive-definite constraint for  $\bar{K}_e$ .

For the stiffness relation (3.27), we can design the PI (proportional-derivative) type control  $\tau'_a$  with  $\delta f_e$ -feedback as follows. Let us first rewrite (3.27) by

$$K_e \delta \xi_e = \delta f_e + \mathcal{S}_e \tau'_a \quad (3.29)$$

where  $\mathcal{S}_e(q^*) := K_e(q^*)J_e(q^*)\bar{K}^{-1}N_c(q^*)\mathcal{S}_a \in \mathbb{R}^{n_e \times n_a}$ . The wrench control objective is given by

$$f_e = f_e^* + \delta f_e \rightarrow f_e^d = f_e^* + \delta f_e^d \in \mathcal{W}_e^d$$

that is, what we need to attain can be written as  $\delta f_e \rightarrow \delta f_e^d$ . To attain this, we design  $\tau'_a$  s.t.,

$$\tau'_a = \mathcal{S}_e^\dagger [K_e \delta \xi_e - \delta f_e^d + K_I \int_0^t (\delta f_e - \delta f_e^d) ds] \quad (3.30)$$

where  $K_I \in \mathbb{R}^{n_e \times n_e}$  is the integral control gain and  $\mathcal{S}_e^\dagger = D_\tau \mathcal{S}_e^T (\mathcal{S}_e D_\tau \mathcal{S}_e^T)^{-1} \in \mathbb{R}^{n_a \times n_e}$  is the weighted pseudo inverse of  $\mathcal{S}_e$  with the weight matrix  $D_\tau = \text{diag}[\tau_1^{lim}, \tau_2^{lim}, \dots, \tau_{n_a}^{lim}] \in \mathbb{R}^{n_a \times n_a}$  based on the joint torque limit  $\tau_i^{lim} := \frac{\bar{\tau}_i - \underline{\tau}_i}{2}$ .

The closed-loop dynamics of (3.29) under (3.30) is then given by

$$\delta f_e - \delta f_e^d + K_I \int_0^t (\delta f_e - \delta f_e^d) ds = 0 \quad (3.31)$$

implying that  $f_e = f_e^d \in \mathcal{W}_e^d$ . This linear exponentially-stable dynamics (3.31) also implies that the  $\tau'_a$  can be approximated by

$$\tau'_a = -\mathcal{S}_e^\dagger \delta f_e + \epsilon' \quad (3.32)$$

which consists of the linear function of  $\delta f_e$  and the additional uncertainty term  $\epsilon'$ . This  $\epsilon'$  is bounded, even in the presence of uncertainty, unmodeled disturbance, etc. This bound is (conservatively) estimated and used to compute  $\epsilon_1, \epsilon_2$  in the inclusion constraints (3.22) and (3.25) to ensure their satisfaction even in the presence of  $\tau'_a$  therein.

### 3.5 Nominal Configuration and Active Stiffness Optimization

In this Sec. 3.5, we present optimization processes to decide the nominal configuration  $q^*$  and the active stiffness gain  $K_a$  of (3.11) under all the constraints as stated in Sec. 3.2.2 while utilizing the passive stiffness  $K_f$  of the flexible base as much as we can. For this, we assume that the nominal right arm pose  $\xi_e$ , the supporting contact surface  $\mathcal{X}_c$ , and the desired wrench polytope  $\mathcal{W}_e^d$  (i.e.,  $f_e^*$  and  $\delta f_e^i$  as well) are all given (see Sec. 3.2.2). Optimizing  $q^*$  and  $K_a$  at the same time leads to fairly a complicated NLP (nonlinear programming) problem, thus, here, we decompose it into two sub-problems and sequentially solve, first for  $(q^*, f_c^*, \tau_a^*)$  and then for  $K_a$ .

### 3.5.1 Nominal Configuration Optimization

The first sub-problem is to find the optimal nominal configuration  $q^*$  with its feasible  $(f_c^*, \tau_a^*)$  given the nominal task wrench  $f_e^*$  at the right hand. We formulate the following optimization problem for this:

$$\min_{q^*, f_c^*, \tau_a^*} f_1(q^*, f_c^*, \tau_a^*) \quad (3.33a)$$

$$\text{s.t. } \xi_c(q^*) \in \mathcal{X}_c, \xi_e(q^*) = \xi_e^d \quad (3.33b)$$

$$G(q^*) + J_c^T(q^*)f_c^* + \mathcal{S}_f K_f q_f^* = \mathcal{S}_a \tau_a^* + J_e^T(q^*)f_e^* \quad (3.33c)$$

$$f_c^* \in \mathcal{W}_c(q^*) \quad (3.33d)$$

$$\underline{q} < q^* < \bar{q} \quad (3.33e)$$

$$\underline{\tau}_a \leq \tau_a^* \leq \bar{\tau}_a \quad (3.33f)$$

where:

- The cost function in (3.33a) is designed as

$$\begin{aligned} f_1(q^*, f_c^*, \tau_a^*) \\ = w_1 \|\tau_a^*\|^2 + w_2 \|f_c^*\|^2 + w_3 \sum_{i=1}^n \sigma_i^2(\bar{K}_{geo}^g(q^*) + \bar{K}_{geo}^e(q^*)) \end{aligned}$$

where the first term is to minimize the control effort  $\tau_a^*$ , and the second term to minimize the supporting contact wrench  $f_c^*$  while also reducing the possibly-destabilizing  $\bar{K}_{geo}$  in (3.16) along with the third term minimizing  $\bar{K}_{geo}^g := \frac{\partial G(q)}{\partial q}|_{q^*}$  and  $\bar{K}_{geo}^e := \frac{\partial J_e^T(q)f_e^*}{\partial q}|_{q^*}$ . Here,  $w_1, w_2, w_3 > 0$  are some positive weights and  $\sigma_i$  is the  $i$ -th eigenvalue of a matrix.

- The constraints (3.33b) are to ensure that the right arm maintains the desired nominal pose  $\xi_e^d$  and the left arm keeps holding, or making contact with, the supporting surface  $\mathcal{X}_c$ .
- The constraint (3.33c) is to uphold the quasi-static equation (3.10) to generate  $f_e^*$  at the nominal equilibrium configuration  $q^*$ .
- The constraint (3.33d) is to enforce the supporting contact wrench constraint (3.5) or (3.6).
- The constraints (3.33e) and (3.33f) are just rewriting of the joint angle and torque limit constraints (3.7) and (3.8).

### 3.5.2 Active Stiffness Optimization

Given  $(q^*, f_c^*, \tau_a^*)$  obtained from the first optimization sub-problem (3.33), here, we solve for  $K_a$  in (3.11) to ensure the system stability and the two inclusion constraints, (3.22) and (3.25), while utilizing  $K_f$  as much as possible. For this, we define the following optimization problem:

$$\min_{K_a} f_2(K_a) \tag{3.34a}$$

$$\bar{K}(K_a) > 0 \tag{3.34b}$$

$$\mathcal{W}_e^d \oplus \mathcal{B}_{\epsilon_1} \subset \mathcal{W}_e^r(K_a) \tag{3.34c}$$

$$\mathcal{W}_e^d \oplus \mathcal{B}_{\epsilon_2} \subset \mathcal{W}_e^c(K_a) \tag{3.34d}$$

$$\underline{K}_a \leq K_a \leq \bar{K}_a \tag{3.34e}$$

where:

- The cost function in (3.34a) is designed s.t.,

$$f_2(K_a) = \sum_{i=1}^{n_e} \sigma_i^2(K_e(K_a))$$

to minimize the task space stiffness  $K_e$  in (3.28) at the right arm end-effector to enhance its interaction compliance and robustness to disturbance, uncertainty, etc.

- The constraint (3.34b) is to enforce the positive-definiteness of  $\bar{K}$  even in the presence of possibly-destabilizing  $\bar{K}_{geo}$  in (3.15) and, consequently, the system stability.
- The constraints (3.34c) and (3.34d) are to enforce the two inclusion conditions (3.22) and (3.25), thereby, ensuring the feasibility of the solution to exert any  $f_e \in \mathcal{W}_e^d$  by the right arm under the joint torque limit constraint (3.8) and the supporting surface holding/contact constraint (i.e., (3.5) or (3.6)).
- The constraint (3.34e) is to ensure the well-behavedness of the solution  $K_a$  by enforcing it to be located between some lower bound  $\underline{K}_a$  and upper bound  $\bar{K}_a$ . We set each axis value of these  $\underline{K}_a$  and  $\bar{K}_a$  to be proportional to the joint torque limit.

It is worthwhile to mention that the stiffness analysis and the derived equations of Sec. 3.3 are particularly instrumental for the second optimization sub-problem (3.34). More precisely, if it were not for those analyses and derivations, we need to directly consider (3.14) with all  $(K_a, \delta q, \delta f_c) \in \mathbb{R}^{n_a \times n_a} \times \mathbb{R}^n \times \mathbb{R}^{n_c}$  being the optimization variables. In contrast, by using the various reduction

equations of Sec. 3.3, we only have  $K_a \in \mathbb{R}^{n_a \times n_a}$  as the search variables for the sub-problem (3.34). Further, using the affine presence of  $\delta f_e$  in  $\mathcal{W}_e^c$  (3.24) and in  $\mathcal{W}_e^\tau$  (3.21), the two inclusion constraints, (3.34c) and (3.34d), become rather straightforward to deal with. Let us consider the  $\mathcal{W}_e^\tau$ -inclusion constraint (3.34c) which can be enforced simply by

$$\mathcal{I}_a \leq [A_\tau + B'_\tau(K_a)\delta f_e^i] \oplus \mathcal{B}_{e_1} \leq \bar{\tau}_a, \quad \forall i \in \{1, 2, \dots, n_p\}$$

This can be formulated from (3.21) with the approximation of the feedback wrench control in (3.30). For that, let us recall the  $\mathcal{W}_e^\tau$  formulation with (3.20). With the precise control of (3.30), we can approximate  $\tau'_a$  by (3.32), and we can reformulate (3.20) by

$$\begin{aligned} \tau_a &= \tau_a^* - K_a \delta q_a + \tau'_a = \tau_a^* - K_a \mathcal{S}_a^T \delta q + \tau'_a \\ &= \tau_a^* - K_a \mathcal{S}_a^T \bar{K}^{-1} N_c(q^*) [J_e^T(q^*) \delta f_e + \mathcal{S}_a \tau'_a] + \tau'_a \\ &= \tau_a^* - K_a \mathcal{S}_a^T \bar{K}^{-1} N_c(q^*) [J_e^T(q^*) \delta f_e - \mathcal{S}_a \mathcal{S}_e^\dagger \delta f_e] - \mathcal{S}_e^\dagger \delta f_e \\ &\quad - K_a \mathcal{S}_a^T \bar{K}^{-1} N_c(q^*) \mathcal{S}_a \epsilon' + \epsilon' \end{aligned} \quad (3.35)$$

This reformulated relation in (3.35) can be utilized to reformulate  $\mathcal{W}_e^\tau$  without uncertainty term  $\epsilon'$  by

$$\mathcal{W}_e^\tau := \{f_e \in \mathbb{R}^{n_e} | \mathcal{I}_a \leq A_\tau + B'_\tau \delta f_e \leq \bar{\tau}_a\} \quad (3.36)$$

The uncertainty term  $\epsilon'$  can be bounded by (i.e., independent from  $K_a$ ) conservatively estimated over the interval of  $K_a$  in (3.34e). This uncertainty can be mapped through a matrix  $C_\epsilon = (I - K_a \mathcal{S}_a^T \bar{K}^{-1} N_c(q^*) \mathcal{S}_a)$ , and this mapped

uncertainty can be considered as a ball  $\mathcal{B}_{\epsilon_1}$  with constant radius  $\epsilon_1$ . This derivation leads to the expression of (3.34c).

Similarly, the  $\mathcal{W}_e^c$ -inclusion constraint (3.34d) can be enforced by reformulating (3.23) with (3.32)

$$\begin{aligned} f_c &= f_c^* + J_c^{\bar{K}+T} [J_e^T(q^*) \delta f_e + \mathcal{S}_a \tau_a'] \\ &= f_c^* + J_c^{\bar{K}+T} [J_e^T(q^*) \delta f_e - \mathcal{S}_a \mathcal{S}_e^\dagger \delta f_e] + J_c^{\bar{K}+T} \mathcal{S}_a \epsilon' \end{aligned} \quad (3.37)$$

and this can lead to

$$[A_c + B_c'(K_a) \delta f_e^i] \oplus \mathcal{B}_{\epsilon_2} \in \mathcal{W}_c, \quad \forall i \in \{1, 2, \dots, n_p\}$$

where, again,  $\mathcal{B}_{\epsilon_2}$  is a ball of radius independent from  $K_a$ . It is also equally worthy to recall that the stiffness analysis of Sec. 3.3 is crucial for the development of the feedback control  $\tau_a'$  at the interaction task wrench space of the right arm in Sec. 3.4. This stiffness analysis of Sec. 3.3, to our knowledge, is explicitly revealed in this paper for the first time for the dual-arm robotic system on a flexible base, and we believe it would also be applicable to other types of robots as well (e.g., Justin-DLR on flexible base [26]).

### 3.5.3 Optimization Structure

Sec. 3.5.1 and Sec. 3.5.2 describe the detail of each sub-problem; nominal configuration optimization and active stiffness optimization. The first sub-problem only considers the equilibrium in the nominal task wrench execution and doesn't need to consider the compliance control. The second sub-problem

---

**Algorithm 1** Sequential optimization

---

**INPUT:** (Task set  $(\xi_e^d, \mathcal{W}_e^d)$ , contact environment  $\mathcal{X}_c$ )

**OUTPUT:**  $\mathcal{X}^* = (q^*, \tau_a^*, f_c^*, K_a^*)$

**INITIAL:**  $\mathcal{X}^i \leftarrow q^{init}, \tau_a^{init}, f_c^{init}, K_a^{init}$

**Optimization start**

$(q^*, \tau_a^*, f_c^*) \leftarrow \text{CONFIG. OPT.}(\mathcal{X}^i, \xi_e^d, \mathcal{W}_e^d, \mathcal{X}_c)$  (Eq. (3.33))

$K_a^* \leftarrow \text{STIFF. OPT.}(q^*, \tau_a^*, f_c^*, \mathcal{W}_e^d)$  (Eq. (3.34))

**Optimization end**

**return**  $\mathcal{X}^* = (q^*, K_a^*, \tau_a^*, f_c^*)$

---

analyzes the compliance behavior near the equilibrium configuration. With this property, we can adopt the sequential optimization structure as described in Fig. 3.4. The detailed description of the pose and active stiffness optimization is described in the Algorithm 1.

### 3.5.4 Inverse Kinematics for Initial Variable

Our proposed optimization is a set of highly nonlinear optimization sub-problems, and the proposed framework can show a local-optimal solution, which is highly dependent on the initial condition. Among other optimization variables ( $K_a$ ,  $\tau_a^*$  and  $f_c^*$ ), setting initial condition of system configuration  $q_0^* = [q_{f0}^*; q_{a0}^*] \in \mathbb{R}^n$  is especially essential for the optimization due to the highly nonlinear nature of the problem w.r.t.  $q^*$ . Considering the task pose, supporting contact space, and motion range of the flexible base near the steady state, we solve the feasible initial configuration system by adopting the inverse kinematics problem. The inverse kinematics problem for the initial variable is

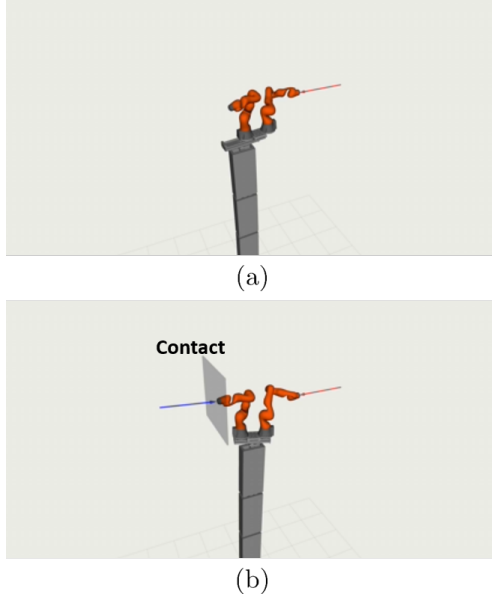


FIGURE 3.6: Snapshot of the comparison between vibration suppression control and the proposed control framework utilizing supporting contact. (a) Force compensation with passivity-based vibration suppression control. (b) Force compensation with the proposed control framework utilizing supporting contact.

expressed by

$$\begin{aligned}
 \min_{q_0^*} \quad & w_c e_c(q_0^*)^T e_c(q_0^*) + w_e e_e(q_0^*)^T e_e(q_0^*) + q_{f0}^{*T} K_f q_{f0}^* \\
 \text{s.t.} \quad & \underline{q} < q_0^* < \bar{q}
 \end{aligned} \tag{3.38}$$

where  $e_c(q) = \xi_c(q_0^*) - \xi_c^d$ ,  $e_e(q_0^*) = \xi_e(q_0^*) - \xi_e^d$  are the error from desired contact pose (choose any of supporting contact pose  $\xi_c^d \in \mathcal{X}_c$ ), and from desired task pose. The cost term  $q_{f0}^{*T} K_f q_{f0}^*$  is added to regulate the initial deflection of the flexible base. We adopt PMI-based inverse kinematics [75] which is a forward dynamics simulation-based optimization solver approach.

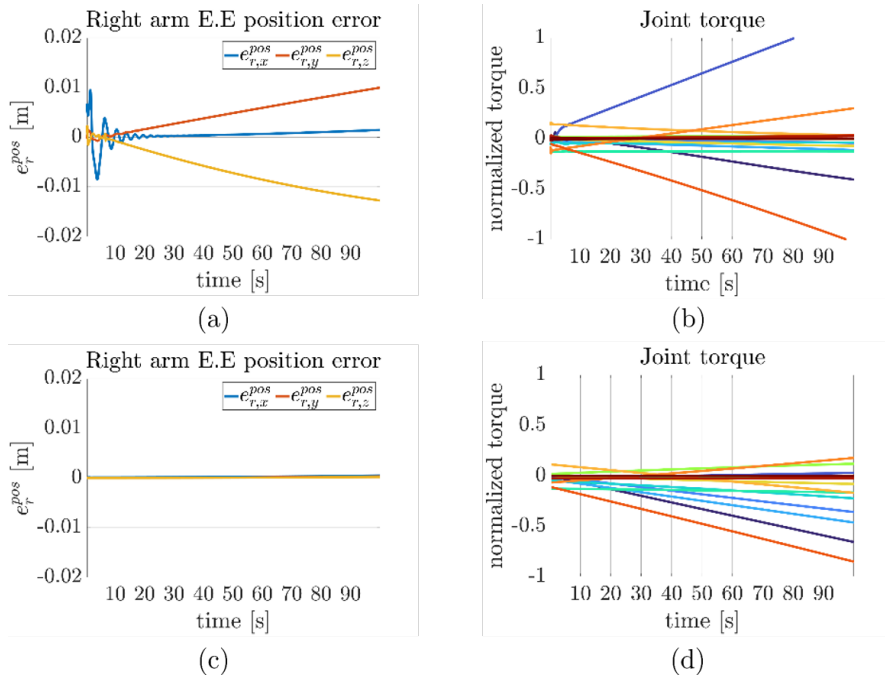


FIGURE 3.7: Results for the force compensation simulation in Fig. 3.6. (a)(b) End-effector position error and normalized joint torque results with passivity-based vibration suppression control. (c)(d) End-effector position error and normalized joint torque results with the proposed control framework utilizing supporting contact.

### 3.6 Simulation

To validate our proposed control framework, we first perform the simulation. For the simulation, we adopt two systems: the dual-arm telerobotic system for height operation in the nuclear power plant in Fig. 2.2, and the small-scale dual-arm system which consists of 7-DoF Franka Panda manipulator in Fig. 3.17.

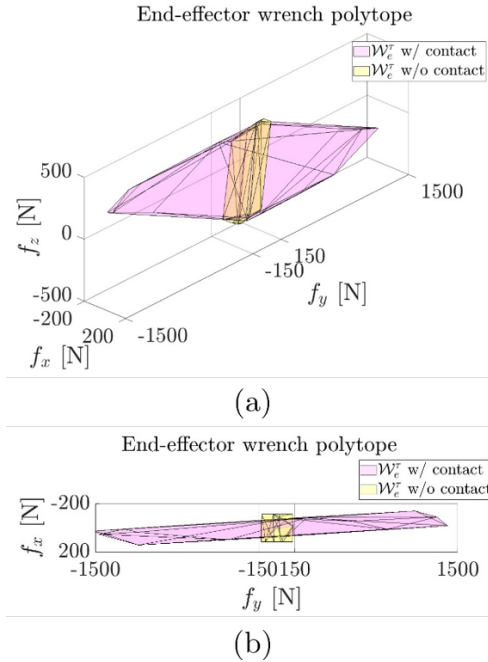


FIGURE 3.8: End-effector wrench polytope comparison with the existence of the supporting contact in two different views.

### 3.6.1 Validation of Supporting Contact

For the simulation with the dual-arm telerobotic system in Fig. 2.2, we aim to validate the necessity of the supporting contact. For that, we first compare the proposed control approach with the passivity-based vibration suppression control approach proposed in Chapter 2. For the same configuration satisfying equilibrium condition (3.10), linearly increasing time-variant external force is exerted at the right arm end-effector as shown in Fig. 3.6 and the system compensates the external force by using passivity-based vibration suppression control and the proposed control utilizing the supporting contact. Plots in Fig. 3.7 show the end-effector error and the normalized joint torque (including stage input) during the force compensation. We can see that the end-effector error

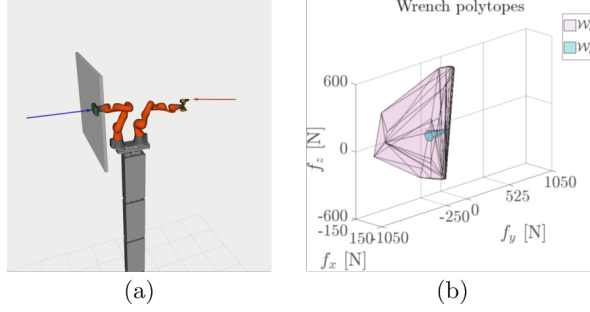


FIGURE 3.9: (a) Snapshot for the force tracking simulation with frictional contact. (b) Wrench polytope generation result.

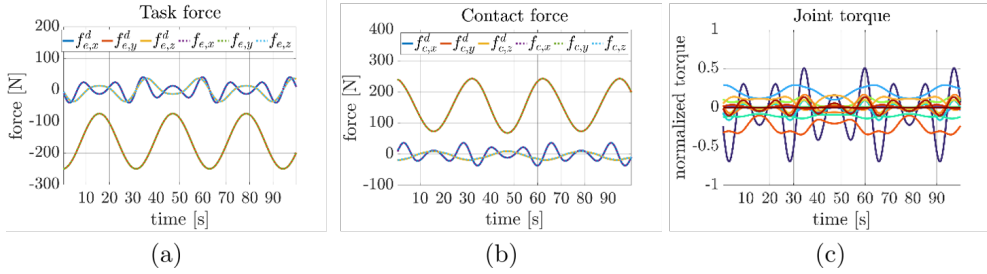


FIGURE 3.10: Simulation results for the force tracking simulation in Fig. 3.9. (a) Task force tracking result. (b) Contact force. (c) Normalized joint torque.

increases with the joint torque limit violation when the vibration suppression control is adopted. This error and the torque limit violation come from the fundamental limit of the system under-actuation. While the passivity-based vibration suppression control in (2.17) compensates the external wrench projected to the 2-DoF horizontal mast-stage position  $x_s$ , the remaining wrench projected to the internal mast-stage motion cannot be compensated due to the under-actuation such that the mast deflection increases which induces the end-effector error and the joint torque limit violation. On the other hand, the proposed control utilizing the supporting contact compensates the linearly increasing external wrench at the desired position within the joint torque limit which validates the necessity of the supporting contact.

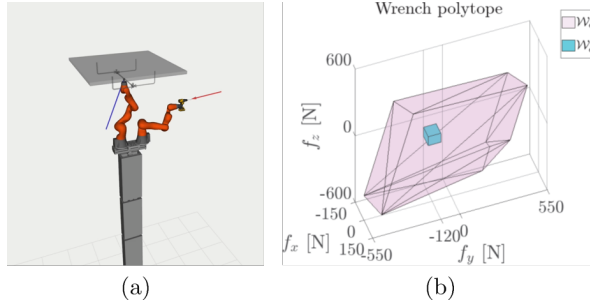


FIGURE 3.11: (a) Snapshot for the force tracking simulation with bilateral holding. (b) Wrench polytope generation result.

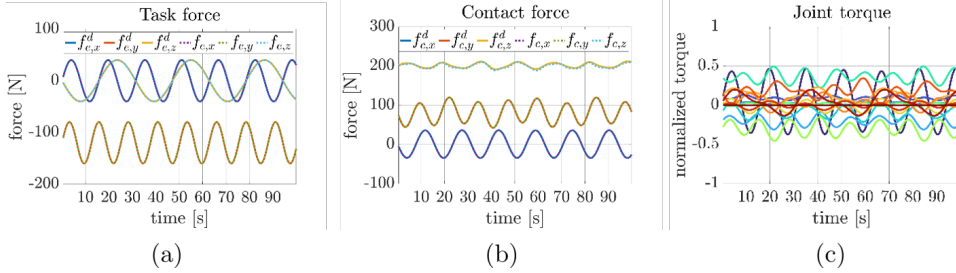


FIGURE 3.12: Simulation results for the force tracking simulation in Fig. 3.11. (a) Task force tracking result. (b) Contact force. (c) Normalized joint torque.

Next, we analyze the wrench capability at the same configuration with the existence of the supporting contact to check the efficacy of the supporting contact. As the flexibility of the mast affects the wrench capability, we utilize the quasi-static stiffness equation in (3.14) without the feedback wrench control term. Then, we can compare  $\mathcal{W}_e^T$  in (3.21) with or without the supporting contact. The wrench polytope generation result is shown in Fig. 3.8, and the supporting contact expands the  $\mathcal{W}_e^T$  such that the system can cover 10 times bigger y-direction force with the utilization of the supporting contact.

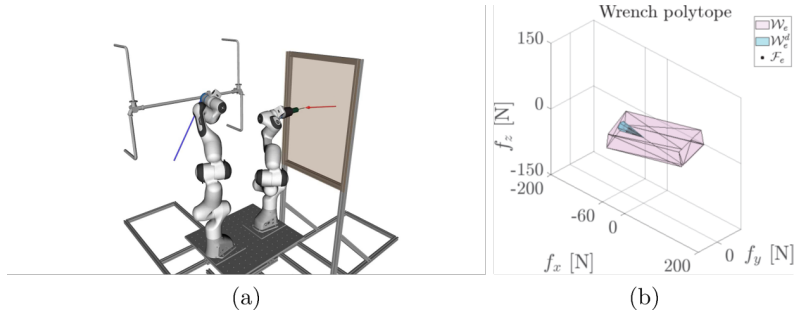


FIGURE 3.13: (a) Snapshot for the force tracking simulation with pipe grasping in the perpendicular direction. (b) Wrench polytope generation result.

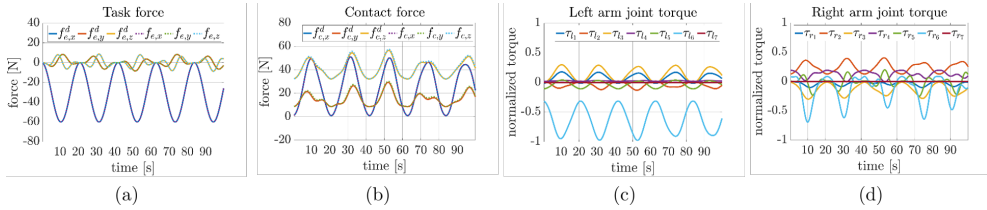


FIGURE 3.14: Simulation results for the force tracking simulation in Fig. 3.13. (a) Task force tracking result. (b) Contact force. (c) Normalized joint torque.

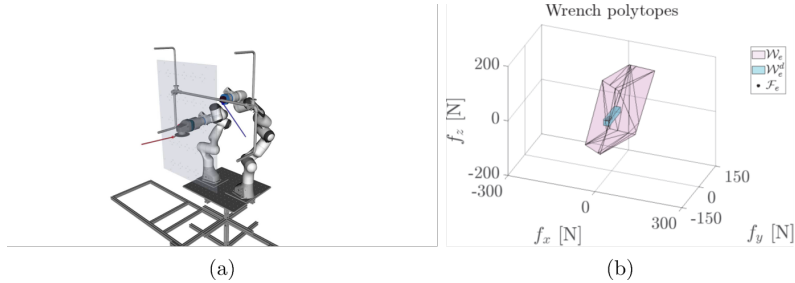


FIGURE 3.15: (a) Snapshot for the force tracking simulation with pipe grasping in the same direction. (b) Wrench polytope generation result.

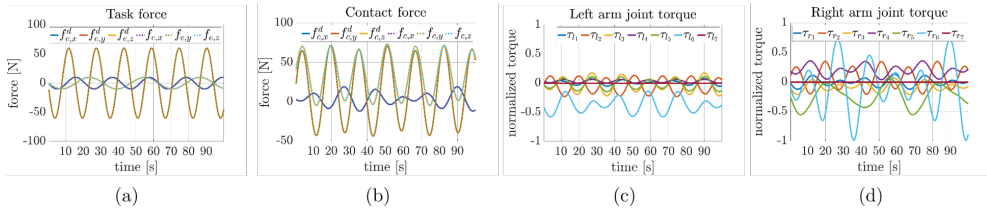


FIGURE 3.16: Simulation results for the force tracking simulation in Fig. 3.15. (a) Task force tracking result. (b) Contact force. (c) Normalized joint torque.

Base Parameter	
Parameter	Values
$m$ (kg)	0.49, 2.38, 0.49, 33.70
$[I_x, I_y, I_z, I_{xy}, I_{xz}, I_{yz}]$ (kg · m <sup>2</sup> )	[1.54e-4, 3e-3, 3e-3, 1.83e-3, -1.4e-5, 0.0], [8.9e-2, 4.5e-2, 4.5e-2, 2.17e-5, 2.5e-7, 2.1e-7], [1.54e-4, 3e-3, 3e-3, 1.83e-3, -1.4e-5, 0.0], [2.02, 0.63, 1.51, 0, -1.31e-5, -3e-3]
$[L_c^x, L_c^y, L_c^z]$ (m)	[0.129; 0; 0], [0.049; 0; 0], [0.129; 0; 0], [0.095; 0; 0]
$K$ (N · m/rad)	1439.8, 1801.13, 1323.35, 2156.89
$B$ (N · m · s/rad)	17.22, 34.07, 23.03, 45.45

TABLE 3.1: Inertial parameter of the flexible base in Fig. 3.17

### 3.6.2 Simulation in Various Scenarios

To validate the performance of the proposed control framework, two control scenarios for each system (systems in Fig. 2.2 and Fig. 3.17) are performed by simulation. The first scenario for the dual-arm telerobotic system in Fig. 2.2 is to perform force tracking with the frictional contact to the vertical wall on the opposite side, and the second scenario is to perform desired force tracking with another type of  $\mathcal{W}_e^d$  with the bilateral holding to the horizontal wall above the system. Simulation results in Fig. 3.10 3.12 shows the efficacy of the proposed control framework with the insurance of the force execution with minimum 170N magnitude.

For the simulation with the system in Fig. 3.17, the system is required to perform desired task force with the one arm grasping to the pipe in two different directions. Simulation results in Fig. 3.14 3.16 shows the efficacy of the proposed control framework with the insurance of the force execution with about 60N magnitude.

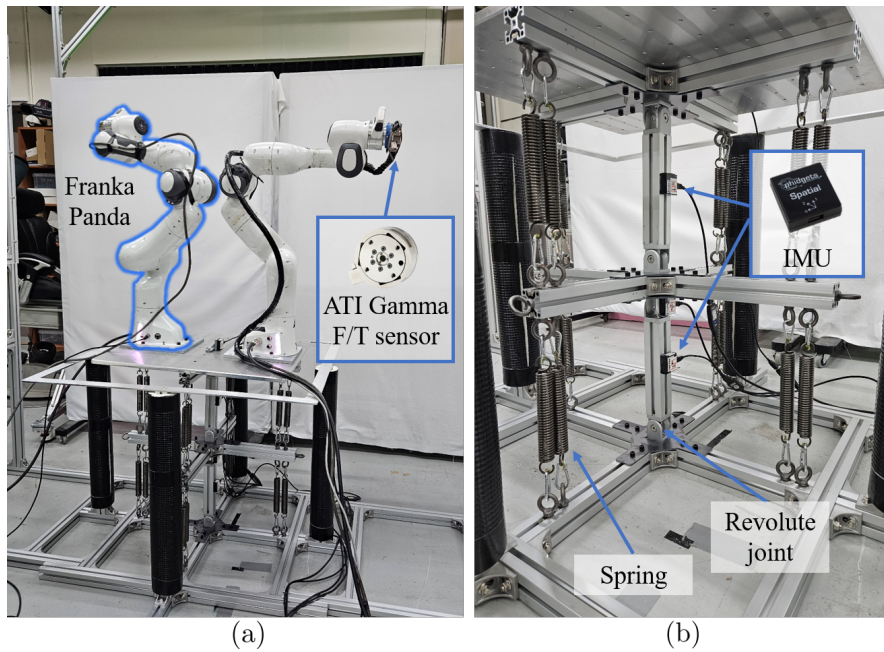


FIGURE 3.17: (a) System setup of the dual-arm manipulator system on the flexible base. (b) Detail of the flexible base with IMU sensor attachment.

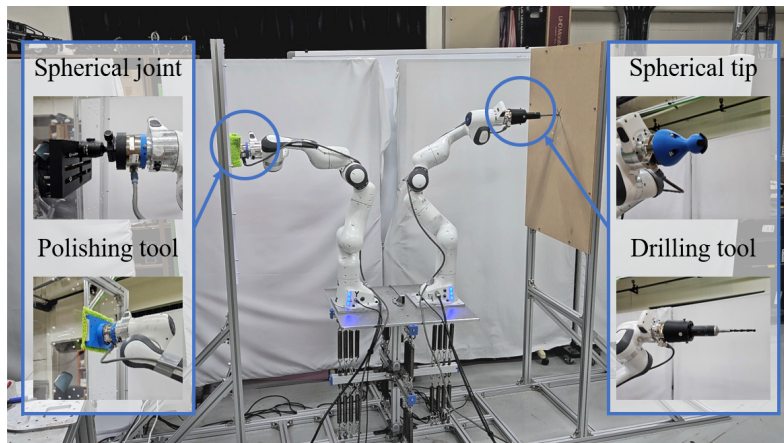


FIGURE 3.18: Environmental setup and the tool setup for the target task execution with the supporting contact.

## 3.7 Experiment

### 3.7.1 Experimental Setup

The hardware setup for the experimental validation of our control framework is described in Fig. 3.17. We adopt a 7-DoF Franka Panda manipulator for each arm with the 1kHz control rate. ATI-Gamma 6-axis F/T sensor is attached to the end-effector of each arm for the contact wrench and the task wrench measurement. For the flexible base setup, we employ an Elastic Kinematic Chain (EKC) modeling technique [36], which is modeled as a 4-DoF ( $n_f = 4$ ) EKC with a universal joint connection. Linear springs are mounted between each segment as shown in Fig. 3.17, and we can approximate the stiffness model of this spring attachment as a joint spring model, which can be linearized near the equilibrium point. For the base state estimation, inertial measurement unit (IMU) sensors (PhidgetSpatial 0/0/3 Basic model) are attached to each link of the base with a 250Hz measurement rate. Estimated inertial parameters of the flexible base are organized in Table. 3.1. For the experimental validation, the system is equipped with the mock-up environment as described in Fig. 3.18. The mock-up environment consists of the left wall for the supporting contact and the right wall for the task execution. Two types of supporting contact are adopted as described in Sec. 3.2.2; the bilateral holding as in (3.5) and the frictional contact as in (3.6). We set  $n_c = 3$  for both contact types such that only contact force is considered. Also, the boundedness of the bilateral holding is set to be  $\alpha = 70N$ , and the friction coefficient is set to be  $\mu = 0.3$ . There are two equivalent contact tools which are equipped at the left arm for each

contact type as shown in Fig. 3.18; a spherical joint setup for the bilateral holding and a flat contact tool for the frictional contact.

The experimental validation includes three scenarios. First, we compare the wrench polytope generation results to check the task wrench feasibility. For given target task information, we compare the generated polytopes  $\mathcal{W}_e$  to check whether these polytopes cover  $\mathcal{W}_e^d$  for the optimized solution in (3.33)-(3.34) and for the unoptimized variables. The unoptimized variables are set to only satisfying (3.33b)-(3.33c). For the second scenario, we aim to check the feedback wrench control performance. The system is required to execute  $f_e^d \in \mathcal{W}_e^d$  to the right wall, and we compare the measured  $f_e$  and  $f_c$  with  $f_e^d$  and  $f_c$  in (3.23). The third scenario is to perform a drilling task for the practical task validation. the system is required to make a hole in the right wall with the drilling tool by executing the desired drilling force. These scenarios are performed for each contact type. We set  $n_e = 3$  during the validation such that only task force is considered. Also, there are two types of tools which are equipped at the right arm for each scenario as shown in Fig. 3.18; a spherical tooltip for the second scenario and an automatic drilling tool (Bosch Go) for the third scenario. For the optimization solver, we utilize the NLOpt [76] optimization library which can deal with nonlinear optimization problems with nonlinear constraints. We utilize the COBYLA solver option in the NLOpt library for the optimization in Sec. 3.5.

Optimization Results: Bilateral Holding			
#	Task		
	$\xi_e^d$ (m)	$f_e^*$ (N)	$\delta f_e^i$ (N)
	Results		
	Time (s)	$\xi_c$ (m)	$\text{vec}(K_a^*)$ ( $N \cdot m/\text{rad}$ )
I	Task		
	[0.8;0.0;1.6]	[0;0;0]	[35;35;28], [35;35;-28], [35;-35;28], [35;-35;-28], [-35;35;28], [-35;35;-28], [-35;-35;28], [-35;-35;-28]
	Results		
	46.44	[-0.7;-0.04;1.54]	[228.48, 207.71, 181.83, 171.66, 101.39, 55, 50, 308.17, 200, 150.99, 127.27, 124.79, 113.44, 101.81]
II	Task		
	[0.85;-0.05;1.6]	[-30;0;0]	[20;30;30], [20;30;-30], [20;-30;30], [20;-30;-30], [-30;30;30], [-20;30;-30], [-20;-30;30], [-20;-30;-30]
	Results		
	127.22	[-0.7;-0.15;1.5]	[977.38, 906.68, 574, 531.08, 100, 50.00, 50.70, 219.46, 200, 206.87, 213.12, 206.47, 144.65, 145.58]
III	Task		
	[1.0;-0.05;1.5]	[-10;0;0]	[0;0;0], [-40;5;8.66], [-40;-5;8.66], [-40;5;-8.66], [-40;-5;-8.66], [-40;10;0], [-40;-10;0]
	Results		
	19.10	[-0.7;-0.09;1.5]	[220, 200, 121, 110, 100, 55, 50, 220, 200, 121, 110, 100, 55, 50]

TABLE 3.2: Optimization results for the case of bilateral holding

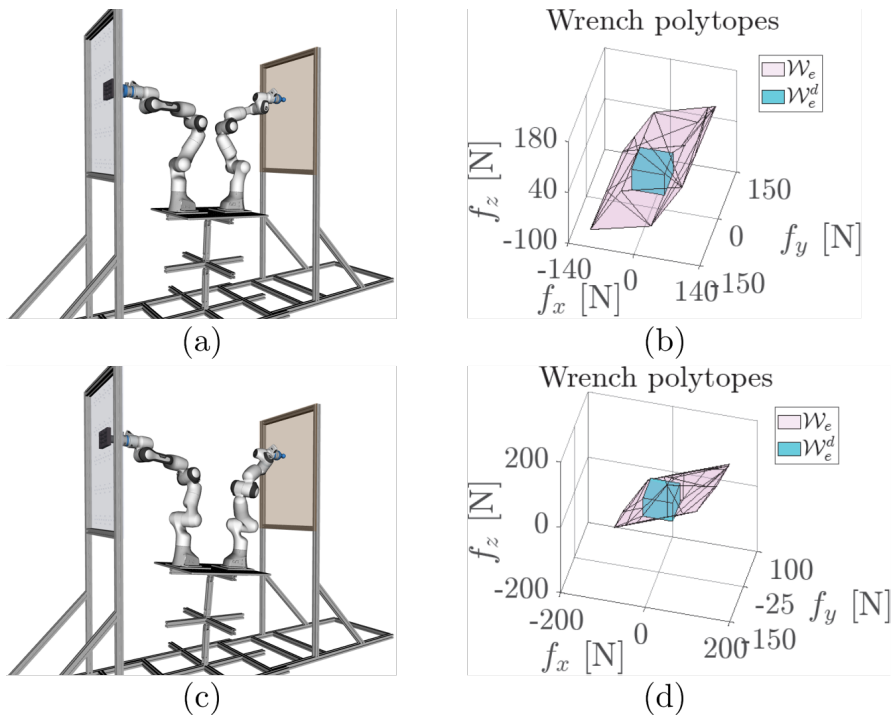


FIGURE 3.19: Comparison between the optimized solution and the unoptimized variables in the case of the bilateral holding. (a) Visualization of the optimized configuration. (b) Wrench polytope generation result from the optimized solution. (c) Visualization of the unoptimized configuration. (d) Wrench polytope generation result from the unoptimized variables.

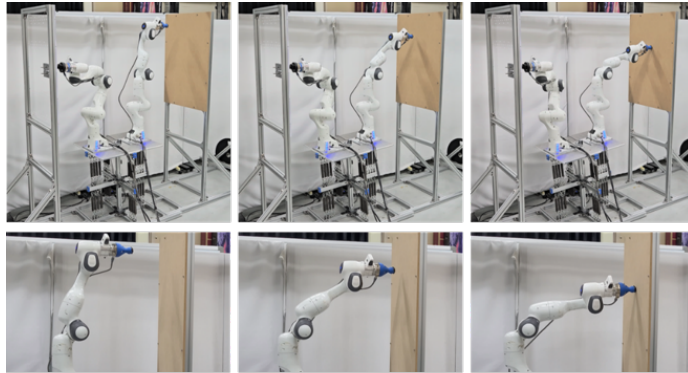
## 3.7.2 Experimental Results

### 3.7.2.1 Case 1 - Bilateral Holding

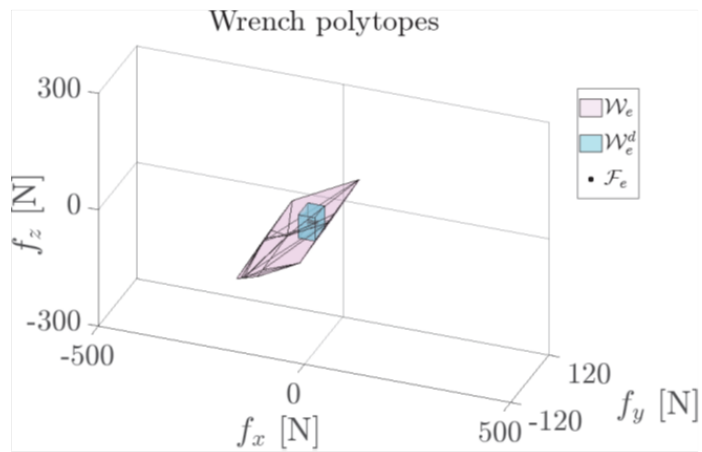
Table. 3.2 shows the information of target tasks and optimization results for the validation of the bilateral holding type supporting constraint case. The optimization results in Table. 3.2 include contact position calculated from  $q^*$ , calculation time and optimized active stiffness gain. During the optimization for validation, we restrict  $K_a$  to diagonal stiffness for simplicity, and the diagonal terms of optimization solution  $K_a^*$  are denoted in Table. 3.2 as a vectorized form for each arm. This restriction of the diagonal stiffness matrix can be relaxed and we can optimize non-diagonal  $K_a$  cases with our proposed framework.

For the first scenario, we compare the task feasibility between the optimized case and the unoptimized case for scenario I. For the unoptimized case, we fix arbitrary contact position  $\xi_c \in \mathcal{X}_c$  and regulate only the equilibrium constraint in Eq. 3.33c. Considering the bilaterality of the supporting contact, we define  $\mathcal{W}_e^d$  as a symmetric cuboid with zero  $f_e^*$ . The comparison result is described in Fig. 3.19. We can see that the generated  $\mathcal{W}_e$  from the optimization solution can cover  $\mathcal{W}_e^d$  as shown in Fig. 3.19-(c), while  $\mathcal{W}_e$  cannot cover the  $\mathcal{W}_e^d$  such that both the joint torque limit and contact wrench constraints (boundedness) are violated in the unoptimized solution as shown in Fig. 3.19-(d).

For the second scenario to validate the force tracking performance,  $\mathcal{W}_e^d$  is set to be cuboid with nonzero  $f_e^*$ . To avoid the slipping motion at the right wall during the task force execution,  $f_e^*$  is set to push the right wall with 30N in



(a)



(b)

FIGURE 3.20: (a) Snapshots for the force tracking experiment with bilateral holding. (b) Wrench polytope generation result.

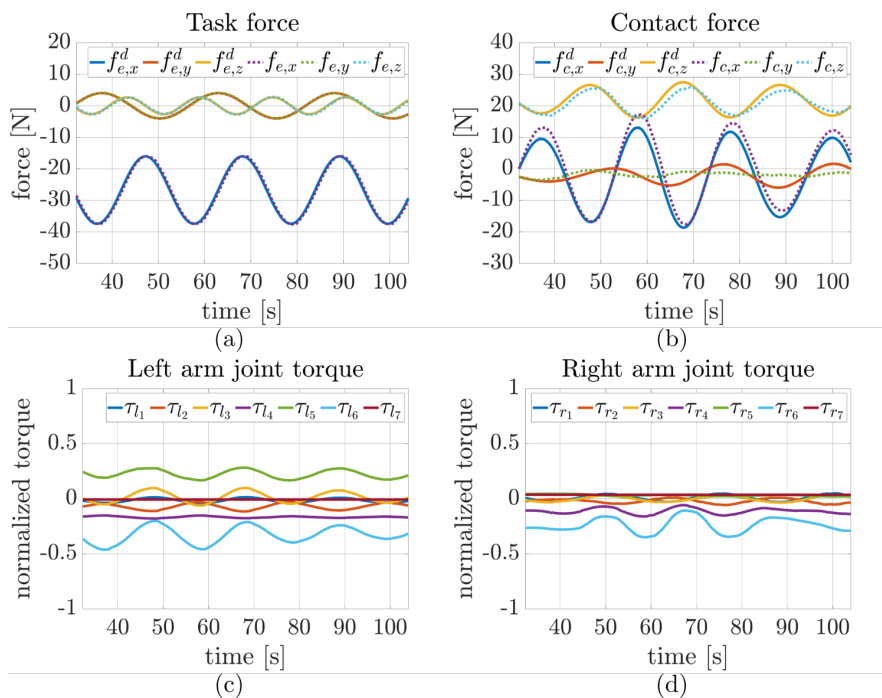
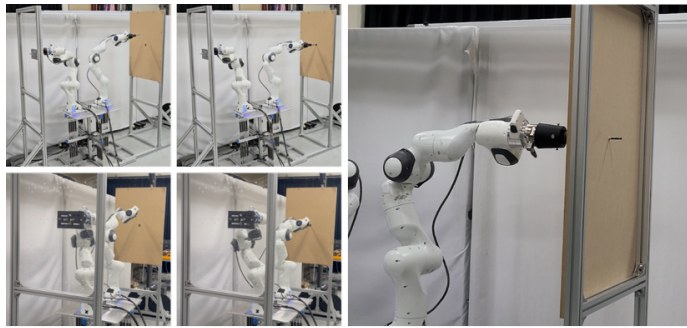


FIGURE 3.21: Experimental results for the force tracking with bilateral holding. (a) Task force tracking result. (b) Contact force. (c) Normalized left arm joint torque. (d) Normalized right arm joint torque.



(a)

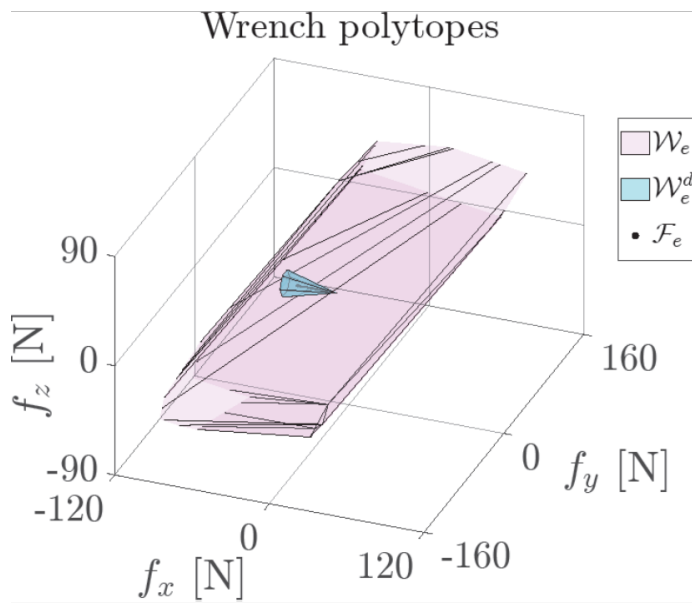


FIGURE 3.22: (a) Snapshots of the drilling task with bilateral holding. (b) Wrench polytope generation result.

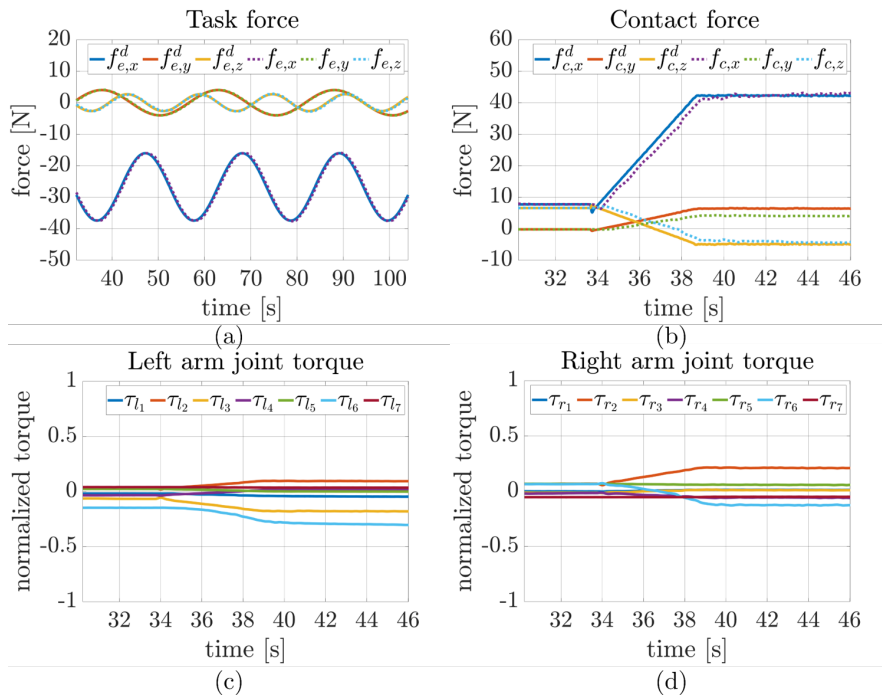


FIGURE 3.23: Experimental results for the drilling task with bilateral holding. (a) Task force tracking result. (b) Contact force. (c) Normalized left arm joint torque. (d) Normalized right arm joint torque.

the task contact normal direction. The force tracking experiment is shown in Fig. 3.20-(a) with the wrench polytope generation result based on optimization results in Fig. 3.20-(b) which guarantees the task wrench feasibility. The force and joint torque measurement results during the task are described in Fig. 3.21. As you can see in Fig. 3.21-(c) and Fig. 3.21-(d) which represent normalized joint torque measurement, the joint torque capacity of the system can cover the desired task force. The task force tracking result is shown in Fig. 3.21-(a) (RMS error: [0.60;0.12;0.18] (N)) and the contact force comparison result is shown in Fig. 3.21-(b) (RMS error: [2.66;2.03;1.37] (N)). We can see that the proposed control shows accurate task force tracking performance while the contact force comparison result shows a bigger error than the task force tracking result. This error may occur due the uncertainties such as the friction of the spherical joint, the parameter of the flexible base, and the kinematic error of the contact and task walls. Another uncertainty comes from the configuration error between the measured system configuration and optimal configuration  $q^*$ . Dual-arm manipulators are directly commanded to follow the optimal configuration  $q_a^*$ , but the flexible base cannot be directly controlled to follow  $q_f^*$  due to the underactuation issue and indirectly controlled through the equilibrium control  $\tau_a^*$ . Due to these uncertainties, the real system configuration and contact force at equilibrium may differ from  $q^*$ ,  $f_c^*$  and generate a deviated task force from  $f_e^*$ . While the task force error can be reduced by the PI control strategy of  $\tau_a'$  in (3.30), there is no specific feedback control for the contact force such that the contact force result shows the bigger tracking error.

Scenario III is to perform the drilling task to make a hole in the right wall. The autonomous drilling tool is operated at a pushing force over  $25N$ , and

Optimization Results: Frictional Contact			
#	Task		
	$\xi_e^d$ (m)	$f_e^*$ (N)	$\delta f_e^t$ (N)
	Results		
	Time (s)	$\xi_c$ (m)	$\text{vec}(K_a^*)$ ( $N \cdot m/rad$ )
I	Task		
	[0.8;0.0;1.6]	[0;0;0]	[0;0;0] [0;0;0], [-40;5;8.66], [-40;-5;8.66], [-40;5;-8.66], [-40;-5;-8.66], [-40;10;0], [-40;-10;0]
	28.76	[-0.7;0.17;1.48]	[336.33, 305.76, 277.96, 252.69, 229.72, 208.84, 89.00, 1000, 627.77, 121, 110, 100, 55, 50]
II	Task		
	[0.85;-0.05;1.55]	[-10;0;0]	[0;0;0], [-30;7.5;13], [-30;-7.5;13], [-30;7.5;-13], [-30;-7.5;-13], [-30;15;0], [-30;-15;0]
	36.15	[-0.7;-0.08;1.72]	[323.09, 293.72, 121, 110, 100, 55, 50, 231.58, 210.52, 121, 110, 100, 55, 50]
III	Task		
	[1.0;0.0;1.6]	[-10;0;0]	[0;0;0], [-40;3;5.20], [-40;-3;5.20], [-40;3;-5.20], [-40;-3;-5.20], [-40;6;0], [-40;-6;0]
	23.58	[-0.7;-0.06;1.54]	[220, 200, 121, 110, 100, 55, 50, 220, 200, 121, 110, 100, 55, 50]

TABLE 3.3: Optimization results for the case of the frictional contact

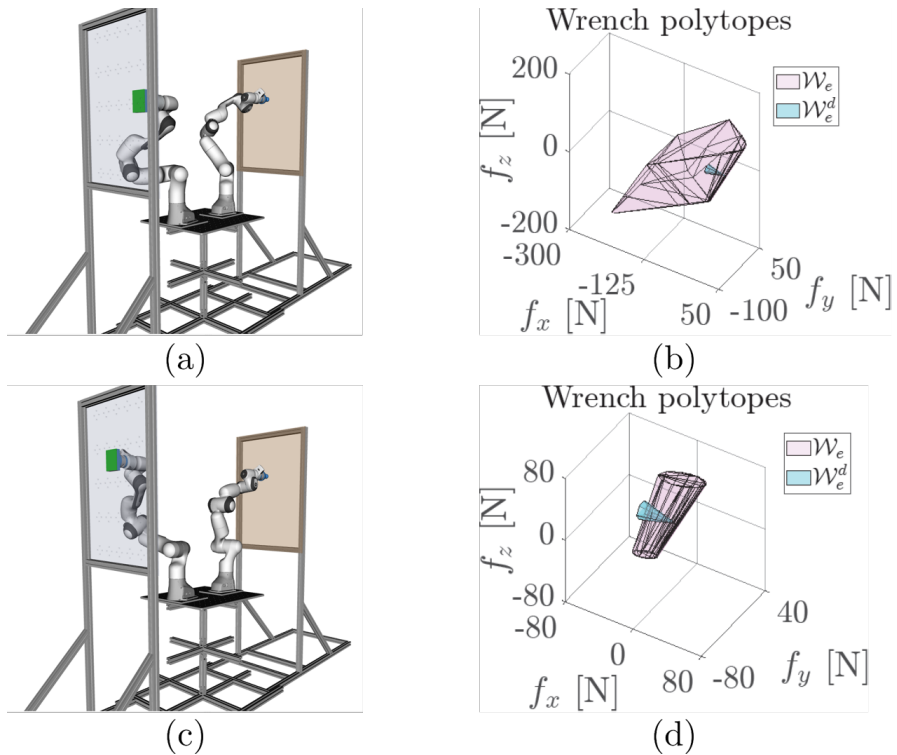


FIGURE 3.24: Comparison between the optimized solution and the unoptimized variables in the case of the frictional contact. (a) Visualization of the optimized configuration. (b) Generated wrench polytopes from the optimized solution. (c) Visualization of the unoptimized configuration. (d) Generated wrench polytopes from the unoptimized variables.

the system is required to execute linearly increasing drilling force with  $40N$  saturation. For that, we adopt cone type  $\mathcal{W}_e^d$ , where  $f_e^*$  is set to push the right wall with  $10N$  task contact normal direction and  $\mathcal{W}_e^d$  is set to push the task wall in maximum  $50N$  with the tangential maximum force is set to be  $10N$ . The wrench polytope generation based on optimization results in Fig. 3.22-(b) guarantee the task wrench feasibility and the drilling experiment is performed as shown in Fig. 3.22-(a). As you can see in Table. 3.2, the optimized  $K_a^*$  shows a lower bounded value when compared with previous experimental scenario results. This is due to the smaller task wall tangential force of  $\mathcal{W}_e^d$ . The contact wall and the task wall in our experimental setup show a parallel direction such that the task wall's normal force can be controlled by the contact force, but the tangential force should be covered mainly by the joint actuation. This induces the smaller  $K_a^*$  result for the drilling task. The force and joint torque measurement results during the drilling task are described in Fig. 3.23. The system shows sufficient actuation capacity during the drilling task as shown in Fig. 3.23-(c) and Fig. 3.23-(d), and the system can exert desired task force as shown in the Fig. 3.23-(a) (RMS error: [0.73;0.06;0.16] (N)) and contact force is given by Fig. 3.23-(b) (RMS error: [1.56;1.78;1.18] (N)).

### 3.7.2.2 Case 2 - Frictional Contact

Table. 3.3 shows the information on target tasks and optimization results for the validation of the frictional contact case. The optimization results in Table. 3.3 also include contact position calculated from  $q^*$ , calculation time and optimized active stiffness gain as same with Table. 3.2, and we also restrict  $K_a$  to diagonal stiffness during the point contact task scenarios. Considering

the unilateral property of the point contact, we set  $\mathcal{W}_e^d$  as a cone-type polytope with dominant task wall-normal direction force.

For the first scenario, we compare the task feasibility between the optimized system and the unoptimized system. As same as the case of the bilateral holding case, we only regulate the equilibrium constraint and the arbitrary contact position  $\xi_c \in \mathcal{X}_c$ , and additionally friction cone constraint of  $f_c^*$  at equilibrium condition. The result is described in Fig. 3.24. As we can see in the Fig. 3.24-(c), the task wrench feasibility is guaranteed with  $\mathcal{W}_e^d$  covered by  $\mathcal{W}_e$ , while  $\mathcal{W}_e$  cannot cover  $\mathcal{W}_e^d$  in the case of unoptimized system. For the case of force tracking simulation in both cases, the simulation results show that the optimized system maintains static supporting contact during the desired task force execution, while the friction cone constraint is violated such that the sliding occurs in the case of the unoptimized case (see Fig. 3.25 which compare  $\mu f_c^n$  and  $f_c^t$ ).

For scenario II, the force tracking experiment is performed as shown in Fig. 3.26-(a), and generated wrench polytopes by the optimization result in Fig. 3.26-(b) shows the guarantee of the task wrench feasibility. Force and control torque measurement results during the experiment are described in Fig. 3.27. We can see that the system can cover the desired task force with its actuation capacity as shown in Fig. 3.27-(c) and Fig. 3.27-(d), and the system can execute desired task force as shown in the Fig. 3.27-(a) (RMS error: [0.29; 0.20; 0.13] (N)) and contact force is given by Fig. 3.27-(b) (RMS error: [1.97; 1.13; 2.76] (N)). The contact force may come from the uncertainties of the system modeling, kinematic error, and the gap from the approximation similar to the bilateral holding case. Scenario III is to perform the drilling task as

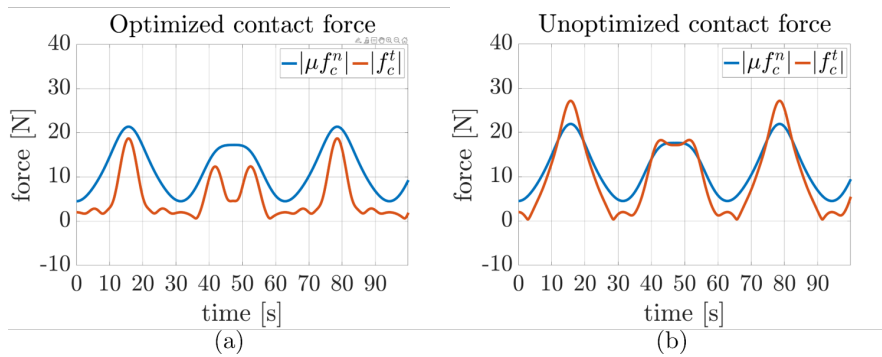
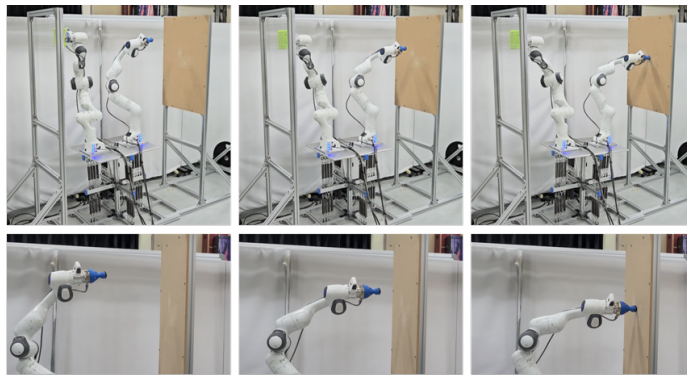


FIGURE 3.25: Contact force comparison between the optimized solution and the unoptimized variables in the case of the frictional contact. The friction cone constraint ( $f_c^t \leq \mu f_c^n$ ) is violated at around 16s, 42s, 51s, and 79s such that slip occurs for the unoptimized case.



(a)

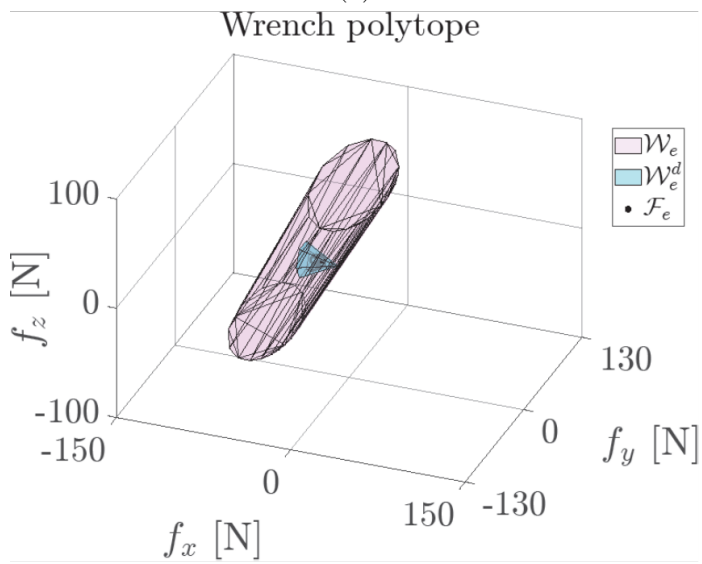


FIGURE 3.26: (a) Snapshots for the force tracking experiment with frictional contact. (b) Wrench polytope generation result.

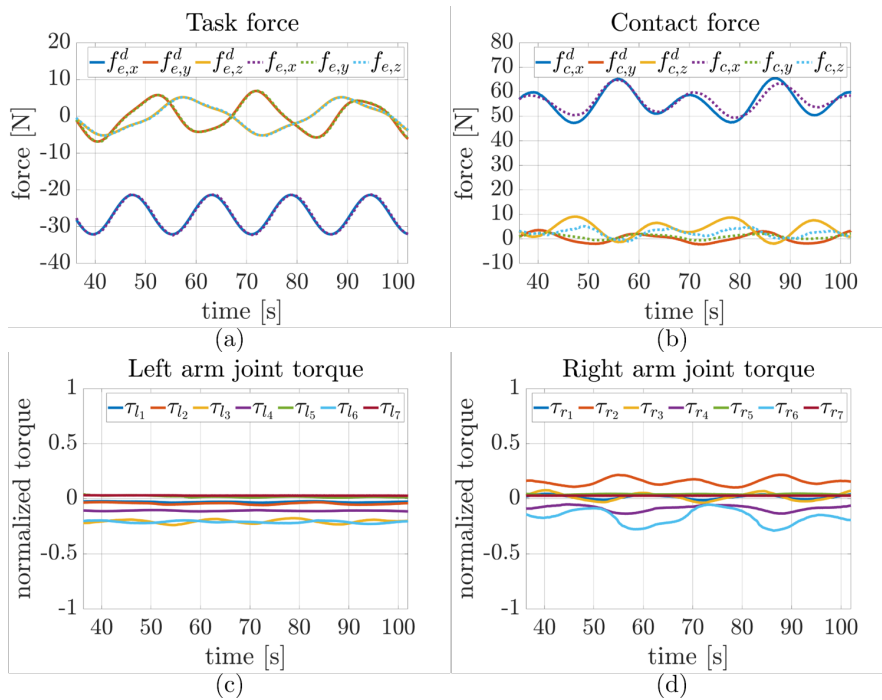
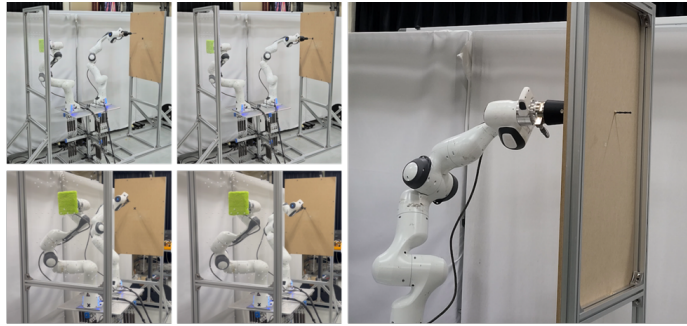


FIGURE 3.27: Experimental results for the force tracking with frictional contact. (a) Task force tracking result. (b) Contact force. (c) Normalized left arm joint torque. (d) Normalized right arm joint torque.



(a)

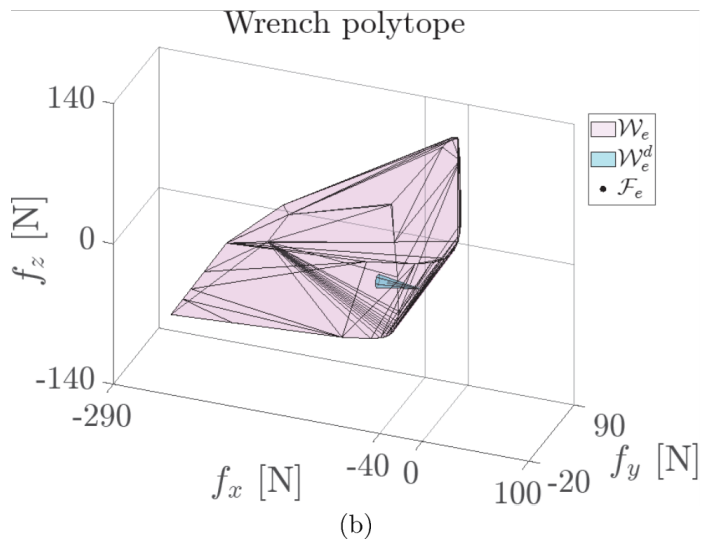


FIGURE 3.28: (a) Snapshots of the drilling task with frictional contact. (b) Wrench polytope generation result.

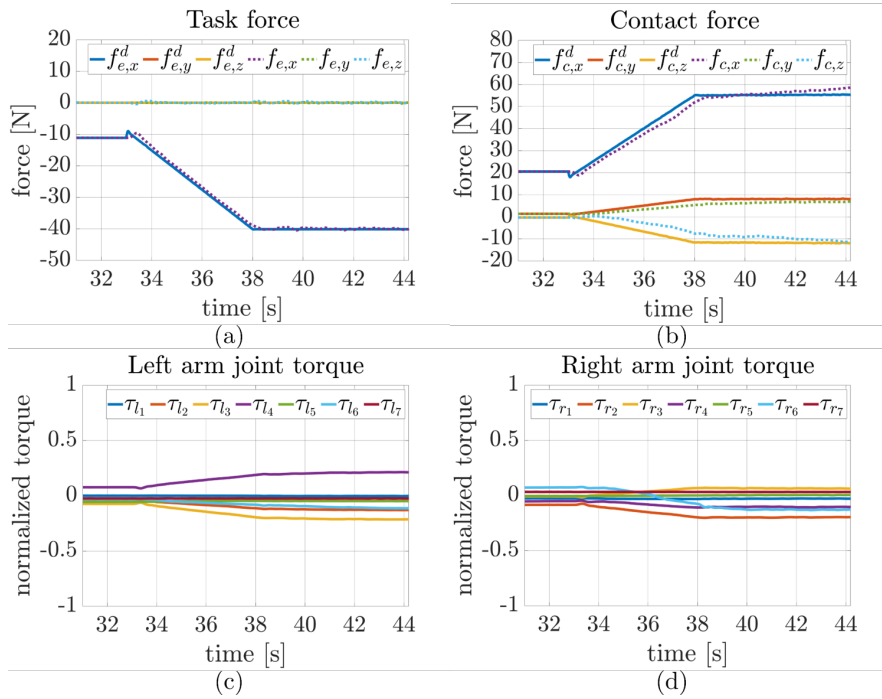


FIGURE 3.29: Experimental results for the drilling task with frictional contact. (a) Task force tracking result. (b) Contact force. (c) Normalized left arm joint torque. (d) Normalized right arm joint torque.

similar to the drilling task with the bilateral holding case. We design a similar structure of  $\mathcal{W}_e^d$  with the bilateral holding case with smaller tangent task force variation. The wrench polytope generation by the optimization result in Fig. 3.28-(b) also guarantees the task wrench feasibility with lower bounded  $K_a^*$  (see Table. 3.3) similar to the bilateral holding case, and the system can make a hole at the right wall by drilling task as shown in Fig. 3.28-(a) with equivalent forces and control torque measurement results shown in Fig. 3.29. The system shows sufficient actuation capacity during the drilling task as shown in Fig. 3.29-(c) and Fig. 3.29-(d), and the system can exert desired task force as shown in the Fig. 3.29-(a) (RMS error: [0.70;0.06;0.19] (N)) and contact force is given by Fig. 3.29-(b) (RMS error: [1.96;1.56;2.76] (N)).

### 3.8 Conclusion

In this chapter, we propose a novel high-force/high-precision interaction control framework of a dual-arm robot system on a flexible base by utilizing the supporting surface with one arm. Based on the integrated control design, which encompasses nominal control, stiffness control, and feedback wrench control, our framework optimizes the nominal configuration (with its related wrenches) and the active stiffness control gain to achieve the target interaction task. Also, by introducing novel stiffness analysis with system flexibility, we can obtain a peculiar linear relation among contact wrench, task wrench, and active control such that we can simplify the optimization process and facilitate the feedback

wrench control design. To validate our control framework, we present some experimental results with the dual-arm robotic system on the flexible base in the mock-up environment which shows the efficacy of the proposed framework.

# Chapter 4

## Conclusion

### 4.1 Summary

Despite the growing attention to robotization of industrial maintenance and repair tasks in the height environment, the fundamental problem of system flexibility has not been strictly handled well in the field of industrial robotics. This flexibility comes from the compliance itself and the assembly tolerance of the long-reach supporting platform and is not negligible as the supporting platform approaches the high altitude, thereby, it is challenging to perform target maintenance tasks with high-precision/high-force requirements. Moreover, the under-actuation (lack of actuation at the supporting platform) further complicates the situation of performing height operations.

To resolve this problem of supporting platform flexibility, in this thesis, we consider the control problem of the dual-arm robotic system on the flexible base for high-precision/high-force operation in the height environment. For that, we define two control problem scenarios to achieve target task operation: 1) passivity-based vibration suppression control for high-precision tasks, and 2)

optimal wrench control utilizing supporting surface for high-force interaction tasks.

For the first problem, we aim to attain precise motion tracking for high-precision target tasks. During the system motion, the vibration of the flexible base occurs which is induced by the manipulator motion and external disturbance. The vibration from the manipulator motion comes from the dynamic coupling between the base and the manipulator system and the control framework attaining motion tracking with the suppression of the base vibration is required. To achieve these two control objectives, we adopt passive decomposition to decompose the system dynamics into two subsystems and design decoupled control inputs. With the utilization of passive decomposition, the system is divided into flexible base dynamics and its orthogonal dynamics (including manipulator motion) without dynamics coupling (inertia coupling) such that these two subsystem dynamics can be controlled separately. Considering the under-actuation of the base, the base subsystem dynamics is defined as the reduced model with dominant vibration modes, and we only suppress these dominant modes with the remaining mimic motions stabilized by its compliance. The performance of the proposed control framework is validated by using a dual-arm telerobotic system on the telescopic mast which is for operation in the nuclear power plant. With experimental validations in a mock-up environment of the nuclear power plant, the proposed control framework successfully suppresses the mast vibration during the motion tracking such that the control enables precise operation in the height environment.

The second problem covers the control problem for the high-force interaction tasks. During the high-force execution to the task environment, the

system may suffer from the deformation induced by the flexible base. To resolve this deformation issue, we utilize the supporting surface to hold or push this surface with one arm while the other arm is executing the interaction force. This exploitation of the supporting contact is inspired by the human nature of supporting contact exploitation during the physical interaction task and the supporting contact wrench can be considered as an additional control input to resolve the deformation and enhance the force capability of the system. For the high-force interaction with supporting contact, we specify the target task as a set of desired task wrenches with the desired task pose and the supporting surface. Based on prior information on the target task, we design our control consisting of 1) nominal control, 2) compliance control, and 3) feedback wrench control. The nominal control and the compliance control (stiffness gain) are optimized through the sequential optimization framework: nominal configuration optimization and stiffness optimization. The feedback wrench control is designed based on the stiffness behavior of the system. The key theoretical result for this optimization and control design is to find the quasi-static stiffness analysis considering the supporting contact, which significantly improves the computational efficiency of the optimization and enables the design of the feedback wrench control. The efficacy of the proposed control framework is validated through some experiments.

By introducing the above two control frameworks of the dual-arm robotic system on the flexible base, we can attain high-precision/high-force height operations which extend the application of this system to various fields of industrial maintenance in height environments.

## 4.2 Future Works

Some possible future research topics include: 1) rigorous analysis of the decomposed dynamics and the controllability for the vibration suppression control with passive decomposition; 2) Improvement of the vibration suppression control; 3) Contact adaptation of the feedback wrench control with supporting contact for unknown environment scenarios; 4) Improvement of the feedback wrench control for high-force interaction with dynamic motion; 5) Extension of the proposed control framework to the other types of robot systems including quadruped, humanoid, LASDRA (Large-Size Aerial Skeleton System with Distributed Rotor Actuation) system with joint locking [77].

# Bibliography

- [1] C. Ha, H. Kim, and D. Lee. Passivity-based control of manipulator-stage systems on vertical flexible beam. In *Proc. IEEE/RSJ Int'l Conference on Intelligent Robots and Systems*, pages 429–435, 2017.
- [2] H. Kim, C. Ha, J. Ahn, J. Lee, and D. Lee. User interface design for semi-autonomous teleoperation of manipulator-stage system on flexible beam. In *In IEEE 2018 15th International Conference on Ubiquitous Robots (UR)*, pages 96–102, 2018.
- [3] MAGDALENA OSUMI. Very big tech enlisted to tackle risky railway tasks in japan, 2022.
- [4] Jiabo Feng and Weijun Zhang. Autonomous live-line maintenance robot for a 10 kv overhead line. *IEEE Access*, 9:61819–61831, 2021.
- [5] D. J. Lee. Passive decomposition and control of nonholonomic mechanical systems. *IEEE Transactions on Robotics*, 26(6):978–992, 2010.
- [6] I. Sharf. Active damping of a large flexible manipulator with a shortreach robot. In *Proc. American Control Conference*, 5:3329–3333, 1995.
- [7] T. Yoshikawa, K. Harada, and A. Matsumoto. Hybrid position/force control of flexible-macro/rigid-micro manipulator systems. *IEEE Transactions on Robotics and Automation*, 12(4):633–630, 1996.

- [8] Tang Wen Yang, Wei Liang Xu, and Jian Da Han. Dynamic compensation control of flexible macro–micro manipulator systems. *IEEE Transactions on Control Systems Technology*, 18(1):143–151, 2010.
- [9] T.W. Yang, Z.Q. Sun, S.K. Tso, and W.L. Xu. Trajectory control a flexible space manipulator utilizing a macro-micro architecture. In *2003 IEEE International Conference on Robotics and Automation (Cat. No.03CH37422)*, volume 2, pages 2522–2528 vol.2, 2003.
- [10] J.Y. Lew, D.J. Trudnowski, M.S. Evans, and D.W. Bennett. Micro manipulator motion control to suppress macro manipulator structural vibrations. In *Proceedings of 1995 IEEE International Conference on Robotics and Automation*, volume 3, pages 3116–3120 vol.3, 1995.
- [11] Lynnane E George and Wayne J Book. Inertial vibration damping control for a flexible base manipulator. In *ASME International Mechanical Engineering Congress and Exposition*, volume 36290, pages 347–354, 2002.
- [12] HİRA Karagülle, LEVENT Malgaca, M Dirilmiş, M Akdağ, and ŞAHİN Yavuz. Vibration control of a two-link flexible manipulator. *Journal of Vibration and Control*, 23(12):2023–2034, 2017.
- [13] Mehdi Abdolvand and Mohamad Hosain Fatehi. Model-base predictive control for vibration suppression of a flexible manipulator. In *Proceedings of 2012 UKACC International Conference on Control*, pages 562–567, 2012.
- [14] Qingxin Meng, Xuzhi Lai, Ze Yan, Chun-Yi Su, and Min Wu. Motion planning and adaptive neural tracking control of an uncertain two-link

- rigid–flexible manipulator with vibration amplitude constraint. *IEEE Transactions on Neural Networks and Learning Systems*, 33(8):3814–3828, 2022.
- [15] Shayan Hoshyari, Hongyi Xu, Espen Knoop, Stelian Coros, and Moritz Bächer. Vibration-minimizing motion retargeting for robotic characters. *ACM Transactions on Graphics (TOG)*, 38(4):1–14, 2019.
- [16] J. Y. Lew, and S. M. Moon. A simple active damping control for compliant base manipulators. *IEEE Transaction on Mechatronics*, 6(3):305–310, 2001.
- [17] J. Lin, Z. Z. Huang, and P. H. Huang. An active damping control of robot manipulators with oscillatory bases by singular perturbation approach. *Journal of Sound and Vibration*, 304(12):345–360, 2007.
- [18] Mahdi Salehi and Gholamreza Vossoughi. Impedance control of flexible base mobile manipulator using singular perturbation method and sliding mode control law. *International Journal of Control, Automation, and Systems*, 6(5):677–688, 2008.
- [19] Wei He, Fengshou Kang, Linghuan Kong, Yanghe Feng, Guangquan Cheng, and Changyin Sun. Vibration control of a constrained two-link flexible robotic manipulator with fixed-time convergence. *IEEE Transactions on Cybernetics*, 52(7):5973–5983, 2021.
- [20] Marc-André Bégin, Ryan Poon, and Ian Hunter. Streamlined tuning procedure for stable pid control of flexible-base manipulators. *IEEE Robotics and Automation Letters*, 6(4):7413–7420, 2021.

- [21] D. N. Nenchev, K. Yoshida, P. Vichitkulsawat, and M. Uchiyama. Reaction null-space control of flexible structure mounted manipulator systems. *IEEE Trans. on Robotics and Automation*, 15(6):1011–1023, 1999.
- [22] D. N. Nenchev. Reaction null space of a multibody system with applications in robotics. *Mechanical Sciences*, 4(1):97–112, 2013.
- [23] Naoyuki Hara, Dragomir Nenchev, Qiao Sun, and Daisuke Sato. Momentum conserving path tracking through dynamic singularities with a flexible-base redundant manipulator. In *2010 IEEE/RSJ International Conference on Intelligent Robots and Systems*, pages 5392–5397, 2010.
- [24] Fabian Beck, Gianluca Garofalo, and Christian Ott. Vibration control for manipulators on a translationally flexible base. In *2019 International Conference on Robotics and Automation (ICRA)*, pages 4451–4457, 2019.
- [25] Gianluca Garofalo, Fabian Beck, Julian Klodmann, and Christian Ott. On the control of translationally flexible base manipulators. In *2020 European Control Conference (ECC)*, pages 867–874, 2020.
- [26] T. Wimbock, D. Nenchev, A. Albu-Schäffer, and G. Hirzinger. Experimental study on dynamic reactionless motions with dlr’s humanoid robot justin. In *Proc. IEEE/RSJ International Conference on Intelligent Robots and Systems*, pages 5481–5486, 2009.
- [27] Dongil Choi. Min-max control for vibration suppression of mobile manipulator with active suspension system. *International Journal of Control, Automation and Systems*, 20(2):618–626, 2022.

- [28] Akira Abe. Minimum energy trajectory planning method for robot manipulator mounted on flexible base. In *2013 9th Asian Control Conference (ASCC)*, pages 1–7, 2013.
- [29] T. Bretl, and Z. McCarthy. Mechanics and quasi-static manipulation of planar elastic kinematic chains. *IEEE Transactions on Robotics*, 29(1):1–14, 2013.
- [30] M. W. Hannan and I. D. Walker. Real-time shape estimation for continuum robots using vision. *Robotica*, 23(5):645–651, 2005.
- [31] A. Borum, D. Matthews, and T. Bretl. State estimation and tracking of deforming planar elastic rods. In *Proc. IEEE Int’l Conference on Robotics and Automation*, pages 4127–4132, 2014.
- [32] E. J. Lobaton, J. Fu, L. G. Torres, and R. Alterovitz. Continuous shape estimation of continuum robots using x-ray images. In *Proc. IEEE Int’l Conference on Robotics and Automation*, pages 725–732, 2013.
- [33] J. Jeon and B. Yi. Shape prediction algorithm for flexible endoscope. In *Proc. IEEE Int’l Conference on Robotics and Automation*, pages 2856–2861, 2014.
- [34] S. C. Ryu and P. E. Dupont. Fbg-based shape sensing tubes for continuum robots. In *Proc. IEEE Int’l Conference on Robotics and Automation*, pages 3531–3537, 2014.
- [35] R. J. Roesthuis, M. Kemp, J. J. van den Dobbela, and S. Misra. Three-dimensional needle shape reconstruction using an array of fiber

- bragg grating sensors. *IEEE/ASME Transactions on Mechatronics*, 19(4):1115–1126, 2014.
- [36] J. Ahn, J. Yoon, J. Lee, and D. Lee. Model-free optimal estimation and sensor placement framework for elastic kinematic chain. In *Proc. IEEE Int’l Conference on Robotics and Automation*, pages 8776–8782, 2019.
- [37] Loris Roveda, Federico Vicentini, Nicola Pedrocchi, and Lorenzo Molinari Tosatti. Force-tracking impedance control for manipulators mounted on compliant bases. In *2014 IEEE International Conference on Robotics and Automation (ICRA)*, pages 760–765, 2014.
- [38] Loris Roveda, Federico Vicentini, Nicola Pedrocchi, Francesco Braghin, and Lorenzo Molinari Tosatti. Impedance shaping controller for robotic applications involving interacting compliant environments and compliant robot bases. In *2015 IEEE International Conference on Robotics and Automation (ICRA)*, pages 2066–2071, 2015.
- [39] Yuquan Wang, Arnaud Tanguy, Pierre Gergondet, and Abderrahmane Kheddar. Impact-aware humanoid robot motion generation with a quadratic optimization controller. *arXiv preprint arXiv:2001.08454*, 2020.
- [40] Ko Yamamoto, Taiki Ishigaki, and Yoshihiko Nakamura. Humanoid motion control by compliance optimization explicitly considering its positive definiteness. *IEEE Transactions on Robotics*, 38(3):1973–1989, 2022.
- [41] Mathew Jose Pollayil, Franco Angelini, Guiyang Xin, Michael Mistry, Sethu Vijayakumar, Antonio Bicchi, and Manolo Garabini. Choosing stiffness and damping for optimal impedance planning. *IEEE Transactions on Robotics*, 39(2):1281–1300, 2023.

- [42] Mohamed Djeha, Pierre Gergondet, and Abderrahmane Kheddar. Robust task-space quadratic programming for kinematic-controlled robots. *IEEE Transactions on Robotics*, 39(5):3857–3874, 2023.
- [43] Diego Ferigo, Raffaello Camoriano, Paolo Maria Viceconte, Daniele Cilandriello, Silvio Traversaro, Lorenzo Rosasco, and Daniele Pucci. On the emergence of whole-body strategies from humanoid robot push-recovery learning. *IEEE Robotics and Automation Letters*, 6(4):8561–8568, 2021.
- [44] Francesco Ruscelli, Matteo Parigi Polverini, Arturo Laurenzi, Enrico Mingo Hoffman, and Nikos G. Tsagarakis. A multi-contact motion planning and control strategy for physical interaction tasks using a humanoid robot. In *2020 IEEE/RSJ International Conference on Intelligent Robots and Systems (IROS)*, pages 3869–3876, 2020.
- [45] Saeid Samadi, Stéphane Caron, Arnaud Tanguy, and Abderrahmane Kheddar. Balance of humanoid robots in a mix of fixed and sliding multi-contact scenarios. In *2020 IEEE International Conference on Robotics and Automation (ICRA)*, pages 6590–6596, 2020.
- [46] Rafael Cisneros, Mehdi Benallegue, Mitsuharu Morisawa, and Fumio Kanehiro. Qp-based task-space hybrid / parallel control for multi-contact motion in a torque-controlled humanoid robot. In *2019 IEEE-RAS 19th International Conference on Humanoid Robots (Humanoids)*, pages 663–670, 2019.
- [47] Aurelien Ibanez, Philippe Bidaud, and Vincent Padois. Unified preview control for humanoid postural stability and upper-limb interaction adaptation. In *2012 IEEE/RSJ International Conference on Intelligent Robots*

*and Systems*, pages 1801–1808, 2012.

- [48] Naoki Hiraoka, Masaki Murooka, Hideaki Ito, Iori Yanokura, Kei Okada, and Masayuki Inaba. Whole-body control of humanoid robot in 3d multi-contact under contact wrench constraints including joint load reduction with self-collision and internal wrench distribution. In *2019 IEEE/RSJ International Conference on Intelligent Robots and Systems (IROS)*, pages 3860–3867, 2019.
- [49] K. Harada, S. Kajita, F. Kanehiro, K. Fujiwara, K. Kaneko, K. Yokoi, and H. Hirukawa. Real-time planning of humanoid robot’s gait for force controlled manipulation. In *IEEE International Conference on Robotics and Automation, 2004. Proceedings. ICRA ’04. 2004*, volume 1, pages 616–622 Vol.1, 2004.
- [50] Masaki Murooka, Shunichi Nozawa, Yohei Kakiuchi, Kei Okada, and Masayuki Inaba. Whole-body pushing manipulation with contact posture planning of large and heavy object for humanoid robot. In *2015 IEEE International Conference on Robotics and Automation (ICRA)*, pages 5682–5689, 2015.
- [51] Guoteng Zhang, Shugen Ma, Yayi Shen, and Yibin Li. A motion planning approach for nonprehensile manipulation and locomotion tasks of a legged robot. *IEEE Transactions on Robotics*, 36(3):855–874, 2020.
- [52] Junheng Li and Quan Nguyen. Kinodynamic pose optimization for humanoid loco-manipulation. In *2023 IEEE-RAS 22nd International Conference on Humanoid Robots (Humanoids)*, pages 1–8, 2023.

- [53] Matteo Parigi Polverini, Arturo Laurenzi, Enrico Mingo Hoffman, Francesco Ruscelli, and Nikos G. Tsagarakis. Multi-contact heavy object pushing with a centaur-type humanoid robot: Planning and control for a real demonstrator. *IEEE Robotics and Automation Letters*, 5(2):859–866, 2020.
- [54] Firas Abi-Farraj, Bernd Henze, Christian Ott, Paolo Robuffo Giordano, and Máximo A. Roa. Torque-based balancing for a humanoid robot performing high-force interaction tasks. *IEEE Robotics and Automation Letters*, 4(2):2023–2030, 2019.
- [55] David E Orin, Ambarish Goswami, and Sung-Hee Lee. Centroidal dynamics of a humanoid robot. *Autonomous robots*, 35:161–176, 2013.
- [56] Hongkai Dai, Andrés Valenzuela, and Russ Tedrake. Whole-body motion planning with centroidal dynamics and full kinematics. In *2014 IEEE-RAS International Conference on Humanoid Robots*, pages 295–302, 2014.
- [57] Stéphane Caron, Quang-Cuong Pham, and Yoshihiko Nakamura. Leveraging cone double description for multi-contact stability of humanoids with applications to statics and dynamics. In *Robotics: Science and System*, July 2015.
- [58] Stéphane Caron and Abderrahmane Kheddar. Multi-contact walking pattern generation based on model preview control of 3d com accelerations. In *2016 IEEE-RAS 16th International Conference on Humanoid Robots (Humanoids)*, pages 550–557, 2016.

- [59] Stéphane Caron, Quang-Cuong Pham, and Yoshihiko Nakamura. Zmp support areas for multicontact mobility under frictional constraints. *IEEE Transactions on Robotics*, 33(1):67–80, 2017.
- [60] Hongkai Dai and Russ Tedrake. Planning robust walking motion on uneven terrain via convex optimization. In *2016 IEEE-RAS 16th International Conference on Humanoid Robots (Humanoids)*, pages 579–586, 2016.
- [61] Romeo Orsolino, Michele Focchi, Carlos Mastalli, Hongkai Dai, Darwin G. Caldwell, and Claudio Semini. Application of wrench-based feasibility analysis to the online trajectory optimization of legged robots. *IEEE Robotics and Automation Letters*, 3(4):3363–3370, 2018.
- [62] Romeo Orsolino, Michele Focchi, Stéphane Caron, Gennaro Raiola, Victor Barasuol, Darwin G. Caldwell, and Claudio Semini. Feasible region: An actuation-aware extension of the support region. *IEEE Transactions on Robotics*, 36(4):1239–1255, 2020.
- [63] Pasquale Chiacchio, Yann Bouffard-Vercelli, and François Pierrot. Force polytope and force ellipsoid for redundant manipulators. *Journal of Robotic Systems*, 14(8):613–620, 1997.
- [64] Antun Skuric, Vincent Padois, Nasser Rezzoug, and David Daney. Online feasible wrench polytope evaluation based on human musculoskeletal models: an iterative convex hull method. *IEEE Robotics and Automation Letters*, 7(2):5206–5213, 2022.

- [65] Antun Skuric, Vincent Padois, and David Daney. On-line force capability evaluation based on efficient polytope vertex search. In *2021 IEEE International Conference on Robotics and Automation (ICRA)*, pages 1700–1706, 2021.
- [66] Arash Ajoudani, Nikos G. Tsagarakis, and Antonio Bicchi. Choosing poses for force and stiffness control. *IEEE Transactions on Robotics*, 33(6):1483–1490, 2017.
- [67] Paul Bosscher, Andrew T Riechel, and Imme Ebert-Uphoff. Wrench-feasible workspace generation for cable-driven robots. *IEEE Transactions on Robotics*, 22(5):890–902, 2006.
- [68] Samuel Bouchard, Clément Gosselin, and Brian Moore. On the Ability of a Cable-Driven Robot to Generate a Prescribed Set of Wrenches. *Journal of Mechanisms and Robotics*, 2(1):011010, 12 2009.
- [69] Tsuneo Yoshikawa. Manipulability of robotic mechanisms. *The International Journal of Robotics Research*, 4(2):3–9, 1985.
- [70] A. Bicchi and D. Prattichizzo. Manipulability of cooperating robots with unactuated joints and closed-chain mechanisms. *IEEE Transactions on Robotics and Automation*, 16(4):336–345, 2000.
- [71] H. Shin, C. Kim, Y. Seo, K. Jeong, Y. Choi, B. Choi, and J. Moon. Aerial work robot for a nuclear power plant with a pressurized heavy water reactor. *Annals of Nuclear Energy*, 92:284–288, 2016.

- [72] H. Shin, S. H. Jung, Y. R. Choi, B. Choi, and C. Kim. Development of a shared remote control robot for aerial work in nuclear power plants. *Nuclear Engineering and Technology*, 50(4):613–618, 2018.
- [73] S. Lall, J. E. Marsden, and S. Glavaški. A subspace approach to balanced truncation for model reduction of nonlinear control systems. *Int'l Journal of Robust and Nonlinear Control*, 12(6):519–535, 2002.
- [74] Mark R Cutkosky and Imin Kao. Computing and controlling compliance of a robotic hand. *IEEE transactions on robotics and automation*, 5(2):151–165, 1989.
- [75] M. Kim, Y. Lee, Y. Lee and D. J. Lee. Haptic rendering and interactive simulation using passive midpoint integration. *The International Journal of Robotics Research*, 36(12):1341–1362, 2017.
- [76] Steven G. Johnson. The NLOpt nonlinear-optimization package. <https://github.com/stevengj/nlopt>, 2007.
- [77] Hyunsoo Yang, Sangyul Park, Jeongseob Lee, Joonmo Ahn, Dongwon Son, and Dongjun Lee. Lasdra: Large-size aerial skeleton system with distributed rotor actuation. In *2018 IEEE International Conference on Robotics and Automation (ICRA)*, pages 7017–7023, 2018.

# 초 록

## 듀얼암-유연성 베이스 시스템의 진동 저감 및 힘 제어

이 정 섭

기계항공공학부

Graduate School of Mechanical Engineering

Seoul National University

본 논문에서는 다양한 산업 현장에서의 고소환경 유지·보수 작업을 위한 듀얼암-유연성 베이스 시스템의 제어 기법을 제안함. 원전/활선 작업과 같은 다양한 산업현장에서의 고소환경 유지·보수 작업을 위해 설계된 로봇 시스템은 듀얼암과 고소환경 접근을 위한 장치 플랫폼으로 구성되며, 이 때 장치 플랫폼의 구조적 특성 및 공차로 인한 유연성은 시스템이 목표로 하는 고정밀/고작업력 유지·보수 작업의 성능을 저하시키며, 시스템의 구동부족으로 이에 대한 제어를 더욱 어렵게 함. 이를 해결하기 위한 다음의 두 가지 제어 기법을 제안하였음: 1) 고정밀 작업을 위한 수동성 동역학 분할 기반 진동 저감 및 사용자지령 추종 제어 기법, 2) 고작업력 작업을 위한 한팔 환경 지지접촉 기반 최적 힘제어 기법.

제안된 각 제어기법의 유효성을 검증하기 위하여 원전 고소작업용 듀얼암/스테이지-텔레스코픽 마스트 시스템 및 듀얼암-유연성 베이스 테스트베드 시스템 등의 다양한 시스템에 대한 시뮬레이션 및 실험 결과를 제시하였으며, 이를 통해 제안된 제어기법의 성능 검증 및 실제 산업현장 유지·보수작업 적용에 대한 가능성을 제시하였음.

**주요어:** 듀얼암 시스템, 유연성 베이스, 진동저감 제어, 동역학 분할, 힘 제어,  
지지 접촉 제어

**학 번:** 2016-20707